# Analysis of Swirl Recovery Vanes

## Propulsion system performance and slipstream-wing interaction

J. J. A. van Kuijk

Technische Universiteit Delft

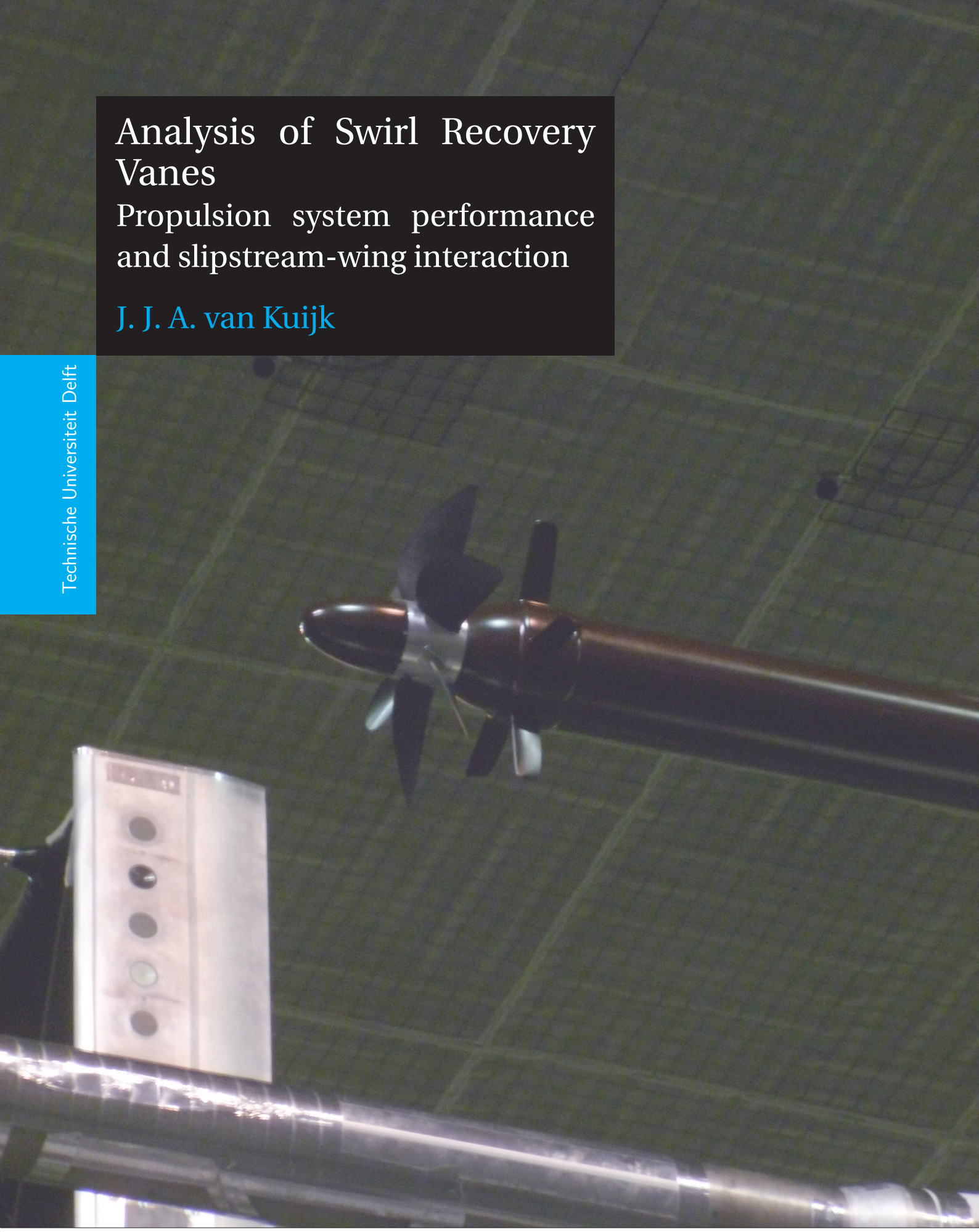

TU Delft Delft University of Technology

Challenge the future

# Analysis of Swirl Recovery Vanes

## Propulsion system performance and slipstream-wing interaction

by

**J. J. A. van Kuijk**

in partial fulfillment of the requirements for the degree of

**Master of Science**
in Aerospace Engineering

at the Delft University of Technology,
to be defended publicly on 20 February, 2015 at 10:00 AM.

| | | |
|---|---|---|
| Supervisor: | prof. dr. ir. L. L. M. Veldhuis, | TU Delft |
| Thesis committee: | prof. dr. ir. L. L. M. Veldhuis, | TU Delft |
| | prof. dr. ing. G. Eitelberg, | TU Delft |
| | ir. T. Sinnige, | TU Delft |
| | ir. W. A. Timmer, | TU Delft |

*This thesis is confidential and cannot be made public until February 20, 2015.*

An electronic version of this thesis is available at http://repository.tudelft.nl/.
Thesis registration number: 021#15#MT#FPP

TU Delft Delft University of Technology

# ACKNOWLEDGMENTS

*J. J. A. van Kuijk*
*Delft, January 2015*

This thesis report is the final part of the Master of Science degree at Delft University of Technology, Master track Flight Propulsion and Performance. I would like to thank the people who have supported me during this period.

I have been interested in propellers, windmills and sustainable energy from a young age onwards; the thesis topic therefore proved to be well suited. The literature study has given me valuable insights in the working of counter rotation rotors and rotors with swirl recovery vanes. The thesis research has given me additional knowledge of the behaviour of rotors, stators and the effect that their slipstreams have on a wing.

I want to thank my MSc thesis primary supervisor Prof. Leo Veldhuis for answering my questions that surfaced during the research and our interesting discussions about rotor-stator systems. Also thanks to secondary supervisor Prof. Georg Eitelberg for his brief but informative input. It was an extraordinary opportunity to have a stator design tested in a wind tunnel during the APIAN-INF test program at the LLF at DNW. Discussions with PhD candidate Tomas Sinnige about the full rotor-stator test setup gave new insights. The APIAN-INF stator could not have been realized without additional CAD-input by Eddy van den Bos, and the manufacturing of the blades by the DEMO workshop of the faculty.

I want to thank my parents for always supporting me in everything I did. I am also grateful for their support during my human powered aircraft projects.

# SUMMARY

This MSc thesis is about the propulsion performance Swirl Recovery Vanes (SRVs), also known as rotor-stator systems. SRVs are mounted behind a rotor of propeller of a propulsion system, to increase the thrust of that system. Where the propulsive element is usually a propeller or fan in aircraft propulsion, here is chosen to use the word 'rotor' for the rotating, thrust producing part of the propulsion system. Although a stator is technically not a rotor, it can be seen as the limit case of a rotor which has zero *rpm*. The rotor-stator system is thus a limit case of a counter-rotation propulsion system. It is known from literature and numerous wind tunnel tests that counter-rotation rotors have quite a gain in propulsion efficiency. There is less literature available on SRVs, but it is found that SRVs can provide about half the gain of counter-rotation systems, without the added difficulties of drive-train issues, large weight increase, and reliability and maintenance issues.

The main part of the thesis concerns the development of a computer program which can analyze rotor-stator systems. It uses the open-source codes XROTOR and XFOIL to assess respectively rotor (or stator) and airfoil performance. The user has to input the rotor and stator designs in XROTOR's rotor data format. The program can also design a stator using the XROTOR Minimum Induced Loss (MIL) routine, or using a simple constant-chord, constant angle of attack BEM code. The rotor of a Fokker F50 was modeled from the XPROP 1/9 scale model of a Dowty-Rotol six-bladed rotor. A stator was designed for both take-off and cruise conditions for this Fokker F50 analysis case, and the blade geometry and stator performance were analyzed. A stator developed for the F50 in cruise conditions gives about 1% gain in propulsion efficiency over the stand-alone rotor, for both cruise and take-off conditions. Literature on SRVs and stators suggests that a gain up to 4% is attainable in the right operation conditions.

As an addition to the development of the rotor-stator analysis routine, there was the extraordinary opportunity to validate the stator performance by designing a stator for the APIAN rotor for the APIAN-INF test program in September 2014. APIAN is an European project between industry and universities to investigate the performance of a six-bladed transonic propeller at a wide range of operating conditions. The test program was conducted in the Large Low-speed Facility (LLF) of DNW in the Netherlands. A short overview of the wind tunnel setup is given. Since the stator test was added quite late to the test program, direct stator thrust and torque measurements were not possible and the PIV setup was less than optimal. At time of writing, PIV results were not fully available yet, so unfortunately there is yet no conclusion on the APIAN stator performance.

An additional part of the thesis explains the development of a lifting line computer program to analyze the influence of a rotor or rotor-stator system slipstream on an aircraft wing. The lifting line method is a fast and reliable method to analyze wings which have very little sweep and little dihedral, such as most wings seen on propeller aircraft. The effect of propulsion system slipstreams on the velocity distribution and angle of attack as seen by

the wing can be analyzed to great detail as long as the number of analysis nodes along the lifting line is large enough. To be able to assess the change in performance by employing a stator behind the rotor, the program analyzes three cases: one wing with stand-alone rotor slipstreams, one wing with the rotor-stator slipstreams, and one uninstalled case where only the wing is analyzed. All three cases are adjusted to have equal lift, with the installed rotor case as baseline, as this is the configuration most seen on existing propeller aircraft today.

As an analysis case the Fokker F50 rotor slipstream and rotor-stator slipstream from the first thesis part are used as an example, together with a model of the F50 wing. Both slipstream cases influence the circulation distribution over the wing such that the induced drag increases, and the wing span efficiency decreases. However, the stator has removed considerable swirl such that the span efficiency of the wing increases by 10% over the stand-alone rotor slipstream case, and gets close to the clean wing span efficiency. Because both F50 rotors rotate in the same direction, the slipstream causes an (unwanted) asymmetrical circulation distribution over the wing. This results in a rolling moment of the wing for the installed cases, where the stator slipstream case reduces this rolling moment significantly.

# Contents

# List of Figures

# List of Tables

# NOMENCLATURE

## Roman symbols

| Symbol | Parameter | Unit |
|---|---|---|
| $A$ | Area of actuator disk | $m^2$ |
| $AR$ | Wing aspect ratio | - |
| $a$ | Axial interference factor in actuator disk theory | - |
| $adv_{xrotor}$ | Advance ratio as used by XROTOR | - |
| $\mathbf{B}$ | Magnetic field vector | $Nm^{-1}A^{-1}$ |
| $B$ | Number of blades of rotor or stator | - |
| $b$ | Wing span | $m$ |
| $C_L$ | Overall lift coefficient for XROTOR stator design | - |
| | (QPROP definition) or aircraft wing overall lift coefficient | - |
| $C_P$ | Power coefficient | - |
| $C_T$ | Thrust coefficient | - |
| $C_Q$ | Torque coefficient | - |
| $C_d$ | Airfoil section drag coefficient | - |
| $C_{d0}$ | Airfoil section profile drag coefficient | - |
| $C_{di}$ | Airfoil section induced drag coefficient | - |
| $C_{d,min}$ | Section minimum drag coefficient | - |
| $C_l$ | Airfoil section lift coefficient | - |
| $C_m$ | Section moment coefficient | - |
| $c$ | Chord length of wing, or rotor or stator blade | $m$ |
| $c_{kink}$ | Wing chord at joining of two trapezoidal panels | $m$ |
| $c_{root}$ | Wing root chord | $m$ |
| $c_{tip}$ | Wing tip chord | $m$ |
| $c/R$ | Chord ratio; chord over tip radius | - |
| $D$ | Rotor diameter | $m$ |
| | or aerodynamic drag | $N$ |
| $D_{wing}$ | Aerodynamic drag of isolated wing | $N$ |
| $D_{wing+propulsion}$ | Total aerodynamic drag of wing and wing-mounted propulsion systems | $N$ |
| $D_{wing,uninstalled}$ | Aerodynamic drag of isolated wing without wing-mounted propulsion systems | $N$ |
| $D_{rest}$ | Aerodyanamic drag of aircraft minus isolated wing | $N$ |
| $dD$ | BEM section drag | $N$ |
| $dL$ | BEM section lift | $N$ |
| $dQ$ | BEM section torque | $Nm$ |
| $dR$ | BEM section resultant force of $dL$ and $dD$ | $Nm$ |

| | | |
|---|---|---|
| $dT$ | BEM section thrust | $N$ |
| $dr$ | BEM radial dimension of a section | $m$ |
| $dy$ | Spanwise section of wing in lifting line theory | $m$ |
| $F$ | Prandtl tip loss factor | - |
| $f$ | Exponent in Prandtl tip loss factor equation | - |
| $H$ | Total pressure of flow | $Pa$ |
| $h$ | Flying altitude in international standard atmosphere (ISA) | $m$ |
| $I$ | Steady electric current | $A$ |
| $J$ | Advance ratio | - |
| $J_{design}$ | Design advance ratio of stator | - |
| $J_{xrotor}$ | Alternate form of advance ratio as used by XROTOR | - |
| $L$ | Lift | $N$ |
| $L_{wing}$ | Lift of isolated wing | $N$ |
| $L_{elev}$ | Lift of elevator | $N$ |
| $L/D$ | Lift-to-drag ratio of airfoil or wing | - |
| $M$ | Mach number | - |
| | or rolling moment of wing with wing-mounted propulsion systems | $Nm$ |
| $\dot{m}$ | Mass flow through rotor | $kg/m^{-3}$ |
| $N$ | Number of lifting line nodes | - |
| $n$ | Rotor revolutions per second | $rps$ |
| $P$ | Power | $W$ |
| $P_{aircraft}$ | Total aircraft propulsive power | $W$ |
| $P_{rotor}$ | Rotor power | $W$ |
| $P_{stator}$ | Stator power | $W$ |
| $P_{sys}$ | System power | $W$ |
| $Q$ | Torque of rotor or stator | $Nm$ |
| $Q_{blade}$ | Torque of one rotor or stator blade | $Nm$ |
| $R$ | Resultant vector of $L$ and $D$ | $N$ |
| | or rotor tip radius (QPROP definition) | $m$ |
| $Re$ | Reynolds number | - |
| $\Re$ | Residual of Newtonian iteration scheme (QPROP definition) | - |
| $r$ | Radius; radial distance of section of rotor or stator | $m$ |
| $\mathbf{r}$ | Position vector (Biot-Savart law) | $m$ |
| $r_{LE}$ | Rotor airfoil LE radius | $m$ |
| $r_{TE}$ | Rotor airfoil TE radius | $m$ |
| $r_{hub}$ | Hub radius | $m$ |
| $r_{hub,rotor}$ | Rotor hub radius | $m$ |
| $r_{hub,stator}$ | Stator hub radius | $m$ |
| $r_{tip}$ | Tip radius | $m$ |
| $r_{tip,rotor}$ | Rotor tip radius | $m$ |
| $r_{tip,stator}$ | Stator tip radius | $m$ |
| $r/R$ | Radial station ratio; radius over tip radius | - |

| | | |
|---|---|---|
| $rpm_{rotor}$ | Rotor revolutions per minute | $rpm$ |
| $rpm_{stator}$ | Stator revolutions per minute | $rpm$ |
| $S$ | Wing area (projected) | $m^2$ |
| $s/R$ | Rotor-stator spacing ratio; spacing over rotor tip | - |
| $T$ | Thrust | $N$ |
| $T_{blade}$ | Thrust of one rotor or stator blade | $N$ |
| $T_{rotor}$ | Rotor thrust | $N$ |
| $T_{stator}$ | Stator thrust | $N$ |
| $T_{sys}$ | System thrust | $N$ |
| $T_{wing+propulsion}$ | Total thrust of wing and wing-mounted propulsion systems | $N$ |
| $U$ | Intermediate velocity of all imposed velocities on rotor section excluding the section's own induced velocities $v_a$ and $v_t$ (QPROP definition) | $ms^{-1}$ |
| $U_a$ | Axial velocity component of $U$ (QPROP definition) | $ms^{-1}$ |
| $U_t$ | Tangential velocity component of $U$ (QPROP definition) | $ms^{-1}$ |
| $u$ | External slipstream velocity (QPROP definition) | $ms^{-1}$ |
| $u_a$ | Axial component of $u$ (QPROP definition) | $ms^{-1}$ |
| $u_t$ | Tangential component of $u$ (QPROP definition) | $ms^{-1}$ |
| $V$ | Relative or total velocity | $ms^{-1}$ |
| $V_\infty$ | Airspeed | $ms^{-1}$ |
| $V_a$ | Axial velocity component | $ms^{-1}$ |
| $V_{a,r}$ | Axial velocity component of rotor | $ms^{-1}$ |
| $V_{a,s}$ | Axial velocity component of stator | $ms^{-1}$ |
| $V_t$ | Tangential velocity component | $ms^{-1}$ |
| $V_{t,r}$ | Tangential velocity component of rotor | $ms^{-1}$ |
| $v$ | Induced velocity of rotor blade (QPROP definition) | $ms^{-1}$ |
| $v_a$ | Axial component of $v$ (QPROP definition) | $ms^{-1}$ |
| $v_t$ | Tangential component of $v$ (QPROP definition) | $ms^{-1}$ |
| $\bar{v}_t$ | Tangential component of $v$, circumferentially averaged (QPROP definition) | $ms^{-1}$ |
| $W$ | Relative or total velocity (QPROP definition) | $ms^{-1}$ |
| | or aircraft weight | $N$ |
| $W_a$ | Axial velocity component of $W$ (QPROP definition) | $ms^{-1}$ |
| $W_t$ | Tangential velocity component of $W$ (QPROP definition) | $ms^{-1}$ |
| $w$ | Downwash imposed by lifting line | $ms^{-1}$ |
| $x$ | Axial distance of rotor local chord section | $m$ |
| | Axial location of rotor or stator objects, positive downstream, zero at rotor $0.25c$ chord line. | $m$ |
| $x/R$ | Axial spacing of rotor and stator (APIAN test data definition) | - |
| $y$ | Tangential dimension of local rotor chord section | $m$ |
| | or wing spanwise position from wing centerline | $m$ |
| $y_0$ | Lifting line center location, spanwise direction | $m$ |

| | | |
|---|---|---|
| $y_{kink}$ | Spanwise distance of kink position from wing centerline | $m$ |
| $y_{rotor}$ | Spanwise distance of rotor axis from wing centerline | $m$ |

**Greek symbols**

| Symbol | Parameter | Unit |
|---|---|---|
| $\alpha$ | Local airfoil section or wing angle of attack | ° |
| $\alpha_0$ | Local zero-lift angle of attack | ° |
| $\alpha_{geo}$ | Local geometric angle of attack | ° |
| $\alpha_i$ | Local induced angle of attack | ° |
| $\beta$ | Local blade angle | ° |
| $\beta_{temp}$ | Local blade angle of APIAN rotor model | ° |
| $\Gamma$ | Circulation | $m^2 s^{-1}$ |
| $\epsilon$ | Inverted drag-to-lift ratio of airfoil section (QPROP definition) | - |
| $\eta$ | Overall propulsion system efficiency | - |
| $\eta'$ | Total aircraft efficiency | - |
| $\eta'_{rotors\ installed}$ | Total aircraft efficiency, with rotor propulsion systems | - |
| $\eta'_{systems\ installed}$ | Total aircraft efficiency, with rotor-stator propulsion systems | - |
| $\eta_{rotor}$ | Rotor propulsion efficiency | - |
| $\eta_{span}$ | Wing span efficiency | - |
| $\eta_{stator}$ | Stator propulsion efficiency | - |
| $\eta_{sys}$ | System propulsion efficiency | - |
| $\overline{\eta}$ | Overall blade efficiency (QPROP definition) | - |
| $\theta$ | Dummy angle for cosine spacing of lifting line nodes over wing span | ° |
| $\lambda_w$ | Local wake advance ratio (QPROP definition) | - |
| $\mu$ | Dynamic viscosity | $Nsm^{-2}$ |
| $\mu_0$ | Magnetic constant | $NA^{-2}$ |
| $\pi$ | Circumference of circle with unit diameter | - |
| $\rho$ | Air density | $kgm^{-3}$ |
| $\phi$ | Angle between the rotation direction and the apparent velocity vector of a blade section | |
| $\chi$ | Angle between the freestream and apparent velocity vector | ° |
| $\Psi$ | Dummy angle used as iteration parameter (QPROP definition) | - |
| $\Omega$ | Rotational velocity of rotor or stator | $rads^{-1}$ |

**List of Abbrevations**

| Abbrevation | Definition |
|---|---|
| APIAN | Advanced Propulsion Integration Aerodynamics and |

| | |
|---|---|
| | Noise |
| BEM | Blade Element Method |
| CFD | Computational Fluid Dynamics |
| DNW | German-Dutch Wind Tunnels |
| ISA | International Standard Atmosphere |
| LE | Leading Edge |
| LLF | Large Low-speed Facility (at DNW) |
| NLR | National Aerospace Laboratory |
| QPROP | Propeller and windmill analysis and design program |
| TE | Trailing Edge |
| XFOIL | Airfoil 2D viscous analysis and design panel method program |
| XPROP | 1/9 scale model of Dowty-Rotol six-bladed rotor |
| XROTOR | Rotor analysis and design blade element method program |

# 1

# INTRODUCTION AND OBJECTIVE

## 1.1. INTRODUCTION

**The history of Swirl Recovery Vanes**

From the beginning of flight, propeller-driven aircraft have mostly used single propellers. Research as early as 1923 [1] showed that the rotation in the slipstream behind a propeller could be partially removed by adding a second, counter-rotating propeller behind the first propeller, although an increase in performance or efficiency was not always seen due to the combination of propellers used. Difficulties concerning the powerplant and gearboxes to drive such a counter-rotating axial system while being sufficiently lightweight and reliable prevented the counter-rotating propeller system from gaining popularity. After World War II there was hardly any research being done on this subject. The oil crisis in the seventies and the strive for fuel reduction in the last decades have given rise to new research on counter-rotating rotors, and to a lesser extent also on SRV rotors. A typical setup can be seen in Figure 1.1. Most of the recent research, which concern both wind tunnel tests as CFD calculations show that there is a propulsion efficiency gain present of several % with the right rotor-rotor or rotor-stator combination. A literature study on this subject by the author [2] gives an overview of propulsion efficiency gains or losses for both counter-rotation and SRV systems. Table 1.1 is reproduced from this study.

**How do SRVs work?**

It might seem counterintuitive that a stator, which 'just sits there', can have significant effect on the flow. A counter-rotation system is more intuitive; the front rotor imparts a swirl which is countered the aft rotor rotating in the opposite direction. As Table 1.1 already has shown, the gain in propulsion efficiency is indeed larger for counter rotation systems than for rotor-stator systems. The principle which creates this gain is the same for both types of rotor systems, and is explained below.

Assume that the rotor sees an uniform freestream flow. There are no tangential components. Axial components are present, since the flow contracts when it is sped up by the rotor. These components are usually significantly smaller than the axial components. Because the rotor-stator system will be analyzed with blade element methods, which by their very nature look at 2D sections along the blade (the plane spanned by the axial and tangential direction), radial flow is usually not taken into account or adjusted for afterwards.

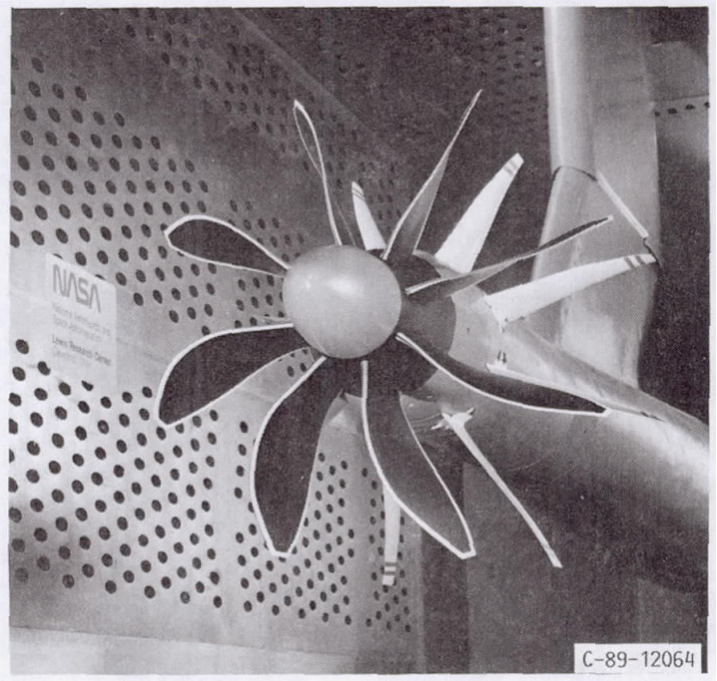


Figure 1.1: Rotor (black) with swirl recovery vanes (white) as used in an experimental study by Dittmar et al. at NASA Lewis Research Center. From [3].

Table 1.1: Efficiency changes of various counter rotation and SRV rotor configurations versus single rotors. From [2].

| SRV efficiency change | % ('+' is more efficient) |
|---|---|
| Yangang et al. [4] | 0 to 3 |
| Gazzaniga and Rose [5] | 2, 4.5 |
| Miller [6] | 3, 4 to 5 |
| Benson [7] | 0.5 to 2.5, -1 to -2 |

| Counter rotation efficiency change | % ('+' is more efficient) |
|---|---|
| Rose and Jeracki [8] | -1 to 0 |
| Lesley [9] [10] | 0.5 to 4 |
| Coleman [11] | 3 to 9 |
| Biermann and Gray [12] | 0 to 6 |
| Biermann and Gray [13] | 1 to 8 |
| Biermann and Hartman [14] | 0 to 16 |
| Munk [1] | -4 to -5 |

Radial flow is therefore assumed to be nonexistent throughout the whole document. Figure 1.2 shows the cross-sections of a rotor blade and a stator blade, and the relevant velocity vectors and forces for this explanation. The rotor airfoil section imparts an axial velocity $V_a$ to the flow, which has to be added to the freestream velocity $V_\infty$. The increase in axial flow velocity is felt by the section as an forward force according to Newton's second law. Summing these forces over the full rotor results in the rotor thrust. Due to downwash and viscous interaction between the flow and the blade, the flow also gets an tangential component $V_t$. This is referred to as 'swirl' because the slipstream behind a propeller will indeed have a rotational component.

A stator or rotor mounted coaxially behind the first rotor thus sees this modified slipstream: generally the total velocity $V > V_\infty$, and $V_t \neq 0$. The local blade angle, the geometric angle between the stator plane and the airfoil chord line, has to be chosen such that the airfoil is still at an angle of attack to this resultant velocity vector. Because the stator airfoil blade angle will be nearly parallel to the freestream or axial direction, the downwash is almost fully directed in tangential direction. A stator blade therefore 'bends' the swirling rotor slipstream back to a more axially-aligned flow.

So far nothing has been said about the effect of the stator on thrust, drag or propulsion efficiency. With a sufficiently efficient stator airfoil ($L/D$) at the local angle of attack in combination with the blade angle, the resultant airfoil $C_l$ and $C_d$ vectors, as seen in Figure 1.3, are positioned such that the axial component of the $C_l$ vector is larger than the $C_d$ vector, and therefore the stator creates an net axial forward force: thrust. Equations 1.1 and 1.2 relate the stator section thrust and tangential forces to the angle of attack.

$$T = Lsin(\chi) - Dcos(\chi) \tag{1.1}$$

$$Q = Lcos(\chi) + Dsin(\chi) \tag{1.2}$$

It has been shown that the stator can deliver thrust under appropriate circumstances (slipstreams, geometry). Because the stator does not rotate, it does not consume any power. This is where the addition of a stator becomes interesting for the total propulsion efficiency of a rotor-stator system; rotor slipstream swirl is exchanged for thrust on the stator blades.

Propulsion efficiency is defined as:

$$\eta = \frac{TV_\infty}{P} \tag{1.3}$$

It is easy to understand that if thrust $T$ increases while power $P$ and freestream velocity $V$ stay constant, the efficiency $\eta$ increases too. This is the very basic idea behind employing SRVs or stators behind a rotor: to increase the total system thrust for the same power requirement.

**The reason for investigating rotor-stator systems**

It can be seen that the gain of a counter-rotation system is twice as high as a SRV system. The SRV system has the advantage of the absence of another gearbox or other drive-train limitations for the stator since the stator blades are stationary. This is also a great advantage over the counter-rotation system in terms of reliability and maintenance. Aircraft and aero-engine manufactures are always looking for ways to increase the fuel efficiency of their products, as this is an important selling point to potential customers due to rising oil prices.

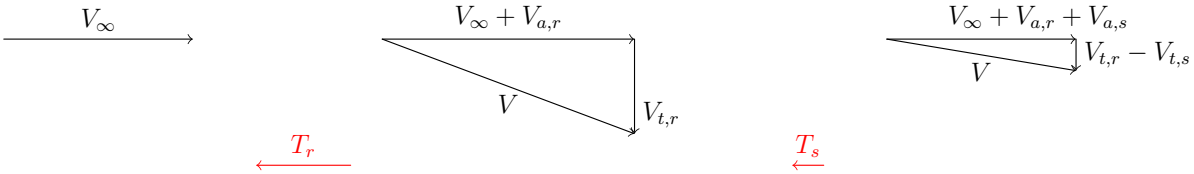


Figure 1.2: Schematic view of the slipstream velocities around a rotor (left) and stator (right) airfoil. It can readily be seen that the stator reduced the rotor swirl. The subscripts $_r$ and $_s$ denote respectively rotor and stator.

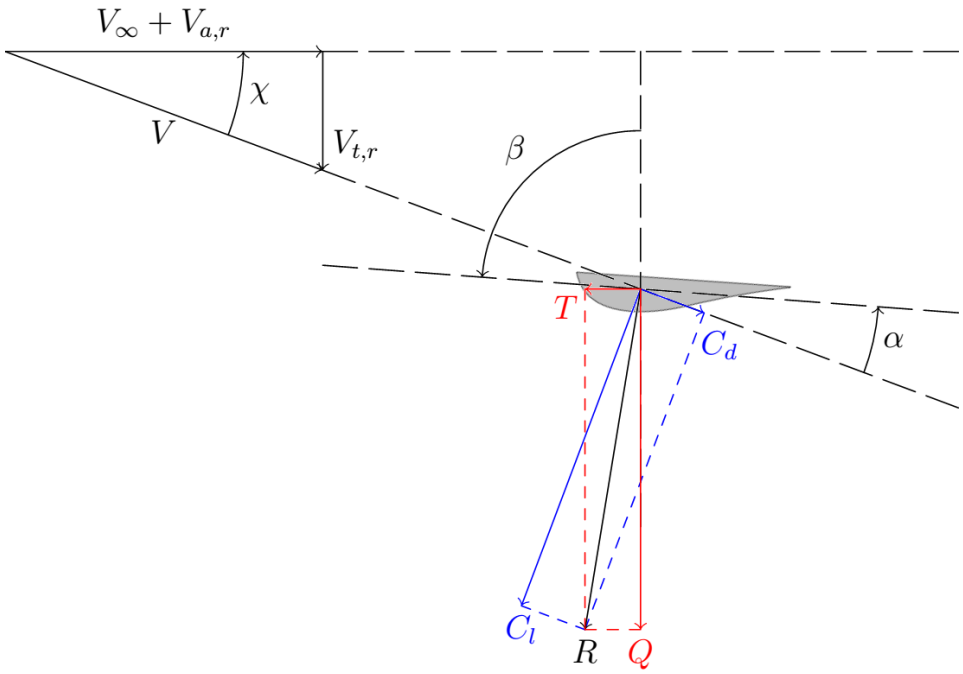


Figure 1.3: Schematic view of force decomposition on a section of a stator blade, operating in a slipstream with tangential flow. The resultant force $R$ due to airfoil lift and drag has a small thrust component and causes a large tangential force which adds to the stator torque. Note that angle $\chi$, and not the angle of attack $\alpha$, defines the thrust and tangential components from the lift and drag forces, whereas $\alpha$ is the geometric angle of attack with respect to the local velocity vector $V$.

With turboprop aeroengines already being advanced in propulsion efficiency and clean combustion, an additional propulsion efficiency gain of just 1% by simply adding SRVs could be seen as a large improvement. The author is therefore mildly surprised that rotor-stator systems are still almost nonexistent, and are also not seen as retro-fits on existing propeller aircraft.

**A note on terminology**

Throughout literature various terms are used for counter-rotation and SRV systems. For the counter-rotation rotors, one can find variations such as 'counter-rotation', 'counter-rotating', 'contra-rotation', and 'contra-rotating', and also these forms without hyphenation. SRV systems have even more options. Swirl Recovery Vanes can indeed be vanes, but the set of vanes can also be thought of a stationary rotor: a stator. Literature mentions terms as 'SRV vanes', 'SRVs', 'stator blades', and 'stator', which all denote stators. In this document the author has chosen to use the following definitions and terms for consistency:

- 'CR' means counter rotation.
- 'SRV' means 'Swirl Recovery Vane', 'SRVs' is plural, and is used also as a different word for stator.
- 'Rotor', although a bit superfluous, is always meant to be the forward rotor or propeller of the system.
- 'Stator' is the aft rotor, which consists of SRVs.
- 'System' or 'SRV rotor' both denote the combination of rotor and stator, but for clarity, 'rotor-stator system' will be used.

## 1.2. OBJECTIVE

**The objective**

The gain in propulsive efficiency by employing a stator is real, as discussed in the literature study by the author [2]. It is deemed wortwhile to further research stator performance as it might be employed on future rotor-driven aircraft, or be installed as retrofits on existing propeller aircraft such as the Fokker and Bombardier turboprop passenger aircraft for example. From Figure 1.3 it might be clear that a small change in $\chi$ will result in very small thrust values, to such extent that the net thrust can become negative: the stator has become a drag-adding device, lowering the overall propulsion efficiency. The design of the stator blades is therefore of utmost importance since small deviations from the ideal can have large influences on performance.

There are various ways of modeling a rotor or stator and assess its performance, from rather simple actuator disk theory via blade element methods (BEMs) to full-fledged CFD analysis. In this MSc thesis the performance of a rotor-stator system was analyzed using a blade element method. BEMs come in various degrees of simplicity and accuracy. The most simple ones analyze a rotorblade as a number of rectangular wing sections placed next to each ochter, with limited accuracy. Advanced BEMs might take into account the tip and root vortex and allow for a minimum induced loss design routine, which is similar in concept of that of the elliptical lift distribution over an aircraft wing for minimum induced

drag. The amount of thrust produced by the stator blades is small (order of a few %) compared to that of the rotor, while the blades are of similar size and see a rather similar flow velocity. This means that the accuracy of a stator analysis or design method should be reasonable to excellent, as the performance gains might otherwise lie well in the uncertainty range of a simple BEM analysis.

The idea was to use a MIL method to design a stator, and see if the designed stator performs as expected or not. The effect of stator design parameters at various advance ratios was analyzed to see how such a rotor-stator system performs at various operating conditions.

If a very accurate solution or very precise answers are to be found, a CFD (Computational Fluid Dynamics) analysis would seem the right way. The slight downside of CFD however, is that creating a mesh of the fluid around the object is a bit of an art in order to get the most accurate results, and that run-times with a fine mesh prevent running a large number of analyses to see which geometry would work best. It is therefore deemed interesting to take 'one step back' and develop a tool which can analyze *different* rotor-stator systems *fast* and with *reasonable accuracy*, in order to be able to asses large numbers of geometries quickly for their *improvement in propulsion efficiency* and *general performance*. The 'winning' rotor-stator combination of this analysis could then be analyzed in more detail by a CFD analysis for example.

Assessing just the performance of a propulsion system might be adequate for aircraft where the propulsion system is mounted in the nose or rear of the fuselage. Many aircraft however have tractor propellers on the wings, which is by far the most common propeller layout on multi-engine aircraft. It might very well be the case that an improvement in propulsion efficiency by adding SRVs is negated by a decrease in wing performance. It is therefore of importance to assess the rotor-stator system performance and the its effect on the wing performance.

An additional part of the thesis looks into the effects of this slipstream-wing interaction by employing a lifting line method to simulate the wing performance. The propulsion system slipstreams have an effect on the circulation and lift distribution over the wing, and therefore they influence the induced drag of the wing. The lifting line program analyses three cases: stand-alone rotor slipstreams, rotor-stator system slipstreams, and a clean wing without slipstreams, where the latter two are compared to the first one in terms of performance. Just like the rotor-stator analysis, the focus lies on creating a *fast* yet reasonably *accurate* tool to quickly asses various geometry cases.

**Research question**

The main research question on which this investigation is based is:

> "What is the effect of design parameters of a rotor with swirl recovery vanes (SRVs) on the system propulsion efficiency, for an uninstalled and installed case?"

In case of an installed system, a wing is placed at some distance behind the rotor and stator. It is assumed that the wing has negligible upstream influence on the SRV rotor system. Based on this research question and the conclusions of the literature study by the author [2], the following sub-questions are defined, which are answered throughout this report:

- What is the effect of rotor-stator spacing on the propulsion efficiency?
- What is the effect of the number of blades of the stator on the propulsion efficiency?
- Does the propulsion efficiency of rotor-stator system increase over a rotor stand-alone?
- How does the increase in propulsion efficiency of a rotor-stator system over a stand-alone rotor change with advance ratio?
- What is the effect of rotors or rotor-stator systems slipstreams on a wing mounted behind the rotors or systems?
- What is the overall aircraft efficiency increase of the rotor or system installed case over an uninstalled case?

# 2

# THEORETICAL BACKGROUND OF ROTOR AERODYNAMICS

## 2.1. ACTUATOR DISK THEORY

One of the most simple and earliest theories (described by Rankine in 1865) to analyze rotor performance is the actuator disk theory, also known as momentum theory. It is one of the most basic and simple means to calculate the thrust of rotor. It's limited scope is the reason that it is not used in the further analysis of rotor-stator systems in this thesis, but it is presented here as a basic example of how and why a rotor or stator creates thrust. Because the theory is not concerned with any rotation of the thrust-creating device, but rather approximates the device by assuming it being a disk, it can intuitively be seen that the thrust-producing mechanism is the same for both stator and rotor.

**The theory**

Assume that the swept area of a rotor can be replaced replaced by an infinitely thin disk with the same tip radius, placed in an uniform flow field. For simplicity, assume there is no hub, such that the disk is indeed solid. See Figure 2.1, and the pressure and velocity distributions in Figure 2.2. The disk is capable of producing a constant pressure change across the disk in a 'magic' way. This velocity difference given to the fluid passing through the disk due to the pressure difference creates an equal and opposite reaction, which is known as thrust.

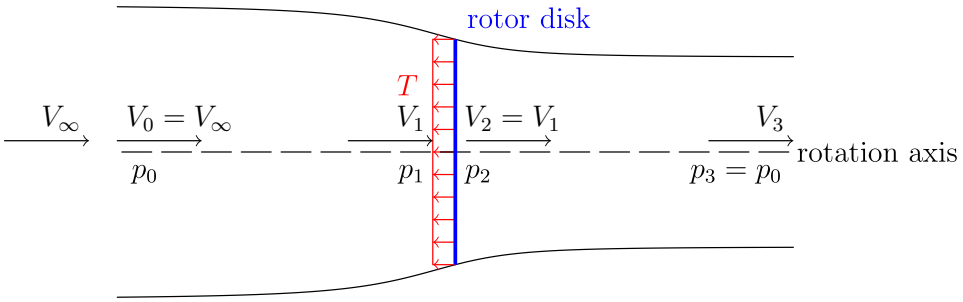


Figure 2.1: Schematic side view of actuator disk and streamline profile, with velocities and pressures indicated.

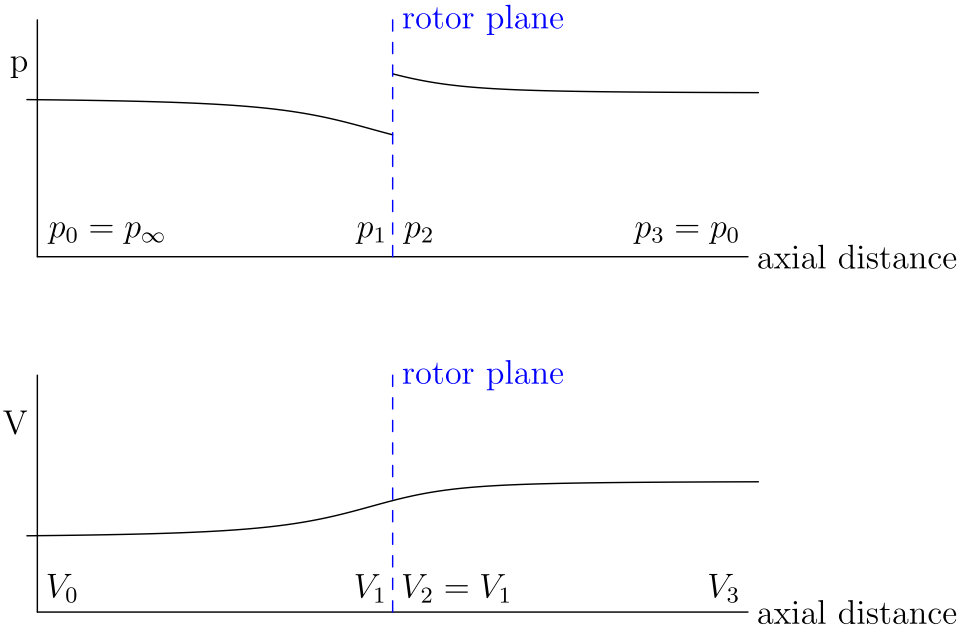


Figure 2.2: Schematic view of velocity and pressure variations along a streamline.

Assuming that the flow is incompressible, Bernoulli's law can be used to find the change in velocity and pressure due to this thrust. Note that this law has to be used on both sides separately, since Bernoulli's law is not valid for domains where energy is added (in this case: a pressure jump across the disk). The total pressure in front and behind the rotor can be written as:

$$\begin{aligned} H_0 &= p_0 + \frac{1}{2}\rho {V_0}^2 \\ &= p_1 + \frac{1}{2}\rho {V_1}^2 \end{aligned} \tag{2.1}$$

$$\begin{aligned} H_1 &= p2 + \frac{1}{2}\rho {V_2}^2 \\ &= p_3 + \frac{1}{2}\rho {V_3}^2 \end{aligned} \tag{2.2}$$

$$p_3 = p_2 + \Delta p \tag{2.3}$$

$$p_0 = p_3 \tag{2.4}$$

$$V_2 = V_1 \tag{2.5}$$

The pressure change $\Delta p$ across the disk can be found by subtracting these total pressures:

$$\begin{aligned} H_1 - H_0 = \Delta p &= p_0 - p_0 + \frac{1}{2}\rho \left({V_3}^2 - {V_0}^2\right) \\ &= \frac{1}{2}\rho \left({V_3}^2 - {V_0}^2\right) \end{aligned} \tag{2.6}$$

Multiplying the area of the disk $A$ by the constant pressure difference the total thrust is found, which can also be expressed by the total change in velocity:

$$\begin{aligned} T &= \Delta p A \\ &= \frac{1}{2} A \rho \left( {V_3}^2 - {V_0}^2 \right) \end{aligned} \tag{2.7}$$

The change in axial momentum can be calculated readily form the velocities by rewriting Equation 2.7 by using the mass flow $\dot{m} = \rho V_1 A$:

$$\begin{aligned} T &= \dot{m} \left( V_3 - V_0 \right) \\ &= A \rho V_1 \left( V_3 - V_0 \right) \end{aligned} \tag{2.8}$$

By equation Equations 2.7 and 2.8, the value for the velocity $v_1$ at the rotor disk can be found:

$$V_1 = \frac{V_0 + V_3}{2} \tag{2.9}$$

Equation 2.9 shows that the induced velocity at the rotor disk is half of the total velocity increase between the freestream velocity and the far wake velocity. Actuator disk theory also introduces the axial interference factor $a$, which is the ratio between the induced axial velocity increase and the freestream velocity. By doing so, $a$ becomes a non-dimensional parameter in preliminary rotor design using actuator disk theory.

$$a = \frac{V_1}{V_0} - 1 \tag{2.10}$$

Rewriting the Equation 2.10:

$$V_1 = V_0 \left( 1 + a \right) \tag{2.11}$$

And since $V_3$ has twice the velocity increase of $V_1$:

$$V_3 = V_0 \left( 1 + 2a \right) \tag{2.12}$$

The thrust equation, Equation 2.8, can now be rewritten in terms of the non-dimensional axial interference factor:

$$\begin{aligned} T &= A \rho V_1 \left( V_3 - V_0 \right) \\ &= A \rho V_0 \left( 1 + a \right) \left( V_0 \left( 1 + 2a \right) - V_0 \right) \\ &= 2 A \rho {V_0}^2 a \left( 1 + a \right) \end{aligned} \tag{2.13}$$

**Strengths and limitations**

Because the actuator disk method is so very simple and fast to implement, it is widely used to get a rough order-of-estimate idea of rotor performance. In some cases it actually produces quite accurate results, especially for low speed rotors with low disk loadings. Helicopter rotors in hover, or aircraft rotors during take-off from standstill cannot be modeled since the freestream velocity should be finite to prevent division-by-zero errors. In reality the induced velocity of the rotor creates an artificial freestream velocity in these situations, but this is certainly not modeled in the actuator disk theory. Further limitations are:

- Friction is not taken into account
- Effect of number of blades is neglected
- Effect of rotation speed is neglected
- It assumes that the pressure jump is seen equally on both sides, which is not necessarily true.

Concerning the last point, this influences the slipstream shape too. As Figure 2.3 shows, the slipstream contraction behind the rotor is quite small, significantly smaller than the contraction seen before the rotor, and this behavior is seen in many other rotors as well. The article by Schouten [15] proposes an improvement over Theodorsen's propeller theory (related to actuator disk theory), and points out that the slipstream behind a rotor undergoes very little contraction, if any, in the improved model. Yang et al. [16] also mention that slipstream contraction behind propellers is very small as shown by a PIV wind tunnel test and photograph(s) of propeller aircraft. See Figure 2.3 for a PIV example.

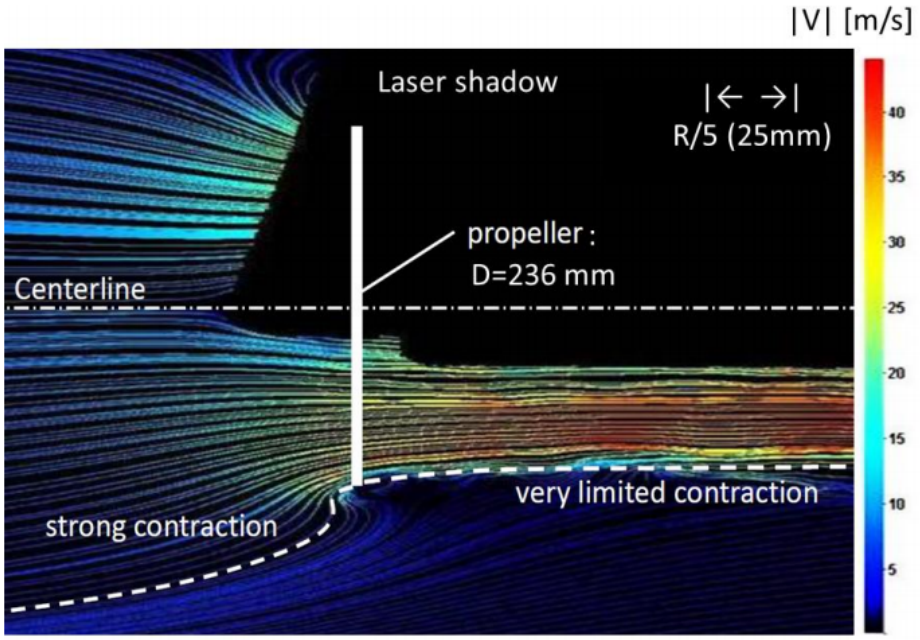


Figure 2.3: PIV image by Yang et al. [16]. Flow direction from left to right. Note the very limited slipstream contraction behind the propeller disk.

Veldhuis [17] (personal communication) explains it in a simple and clear manner: the pressure distribution over the rotor airfoils and their angle with the rotor plane is different from the assumption in the actuator disk theory. In actuator disk theory, the pressure jump across the rotor plane is assumed to equally affect the flow upstream and downstream of the rotor (see Figure 2.2). In reality, the amount of airfoil underpressure is much larger than the overpressure which are located more or less upstream and downstream, respectively. Therefore there is very little overpressure behind the rotor to cause slipstream contraction. See Figure 2.4 for a graphical explanation.

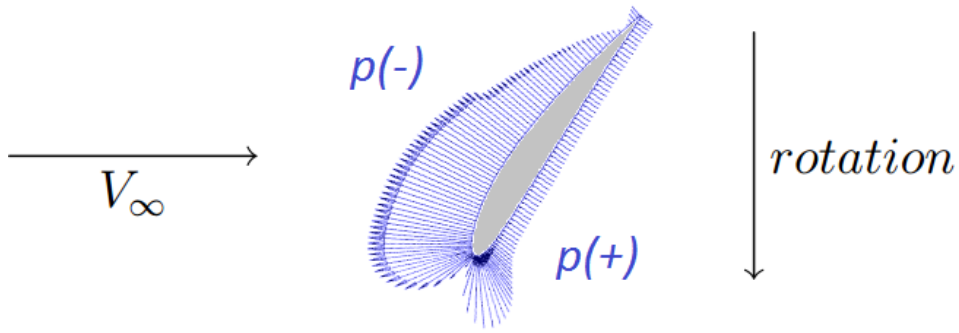


Figure 2.4: Schematic top view of rotor airfoil, with large underpressure upstream and small overpressure dowstream.

All in all, the actuator method does seem to perform rather well concerning the many limitations. For more accurate design and analysis of rotors, the next step is a Blade Element Method (BEM): see next section, Section 2.2.

## 2.2. BLADE ELEMENT METHOD (BEM)

This chapter gives a general description of a Blade Element Method (hereafter: BEM). BEMs and variations on it are widely used to generate preliminary rotor designs or to quickly analyze existing rotors. The most simple BEMs will divide a blade in segments and analyze these segments as separate 2D airfoil sections. More elaborate BEMs iterate on this to create a more accurate results by analyzing the influence of each section on the other, much alike the lifting line method does for wings. A very general description is given below to give a feel of how a BEM works.

The induced velocities on a blade originating from other blades of the same rotor are not taken into account in this example for simplicity. These and other external induced velocities (e.g. from an upstream slipstream) are included in the more accurate MIL routine explained in the next section, and left out here to avoid repetition. However, both simple BEM and the advanced MIL routine operate on the same base principle described below. The program XROTOR uses a MIL BEM, and produces rather detailed results and designs within a very short time. An overview of the specific routine in XROTOR and its limitations is presented in the next chapter.

**Step one: dividing a rotor blade in segments**

As the name suggests, the method looks into segments of a rotor blade. Such a blade should be thought of as a wing consisting of individual segments along its span, each segment having unique geometric parameters such as radius $r$, chord $c$, airfoil, and blade angle $\beta$. Figure 2.5 shows how a section of the rotor blade is defined, and Figure 2.6 shows how the cross-section of such a blade section, with all relevant angles and velocity vectors.

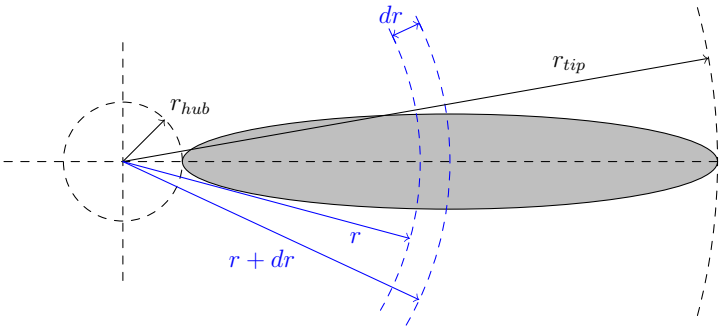


Figure 2.5: Dividing a rotor blade (gray) in radial segments of width $dr$ at radius $r$.

**Step two: calculate segment lift and drag**

Each segment sees a different total velocity $V$. The axial velocity $V_a$ is assumed equal for all segments, but due to constant rotation rate and varying radial position, the tangential velocity is different for each segment: $V_t = \Omega r$. Pythagorean theorem gives the total velocity $V$ seen by the segment:

$$\begin{aligned} V &= \sqrt{{V_a}^2 + {V_t}^2} \\ &= \sqrt{{V_\infty}^2 + (\Omega r)^2} \end{aligned} \tag{2.14}$$

The angle of this relative wind with respect to the rotor plane is $\phi$:

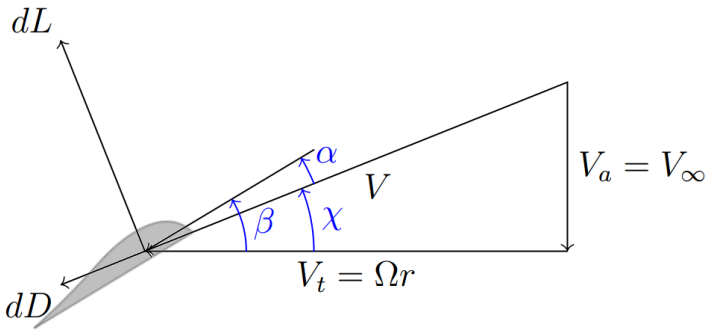


Figure 2.6: A cross-section of a segment, showing the relations between the segment lift and drag and the velocity vectors. Note that the geometric blade angle $\beta$ differs from the velocity angle $\phi$ by the airfoil angle of attack $\alpha$. The magnitude of $V_t$ depends on radial position $r$.

$$\begin{aligned}\phi &= \arctan\left(\frac{V_a}{V_t}\right)\\ &= \arctan\left(\frac{V_\infty}{\Omega r}\right)\end{aligned} \tag{2.15}$$

See Figure 2.6 for clarity. Blade angle $\beta$ is a geometric angle that can be measured on an existing propeller or chosen during design. The airfoil of that segment is placed at a certain angle of attack $\alpha$ with respect to the total velocity vector $W$. Note the relation between $\alpha$, $\beta$, and $\phi$: the angle of attack $\alpha$ is the difference between the geometric blade angle $\beta$ and the relative wind angle $\phi$:

$$\alpha = \beta - \phi \tag{2.16}$$

Simple 2D airfoil analysis gives the local lift, drag, and moment coefficients $C_l$, $C_d$, and $C_m$. The moment coefficient is only of importance for structural calculations or aeroelastic effects, and is neglected in most BEMs. The segment lift $dL$ and drag $dD$ can be found using the following relations:

$$dL = \frac{1}{2} C_l \rho V^2 c, dr \tag{2.17}$$

$$dD = \frac{1}{2} C_d \rho V^2 c, dr \tag{2.18}$$

**Step three: calculate segment thrust and torque**

The thrust created by a segment is the sum of the axial components of $dL$ and $dD$, whereas the torque is the sum of the tangential components, multiplied by the segment radius $r$:

$$\begin{aligned}dT &= dL\cos(\phi) - dD\sin(\phi)\\ &= \frac{1}{2}\rho V^2 c\left(C_l\cos(\phi) - C_d\sin(\phi)\right)dr\end{aligned} \tag{2.19}$$

$$\begin{aligned}dQ &= \left(dL\sin(\phi) + dD\cos(\phi)\right)r\\ &= \frac{1}{2}\rho V^2 cr\left(C_l\sin(\phi) + C_d\cos(\phi)\right)dr\end{aligned} \tag{2.20}$$

The geometric relation between the segment lift, drag, thrust, and torque can be seen in Figure 2.7. Note that they are related to each other by the relative wind angle $\phi$ only, and not by the blade angle $\beta$ or angle of attack $\alpha$.

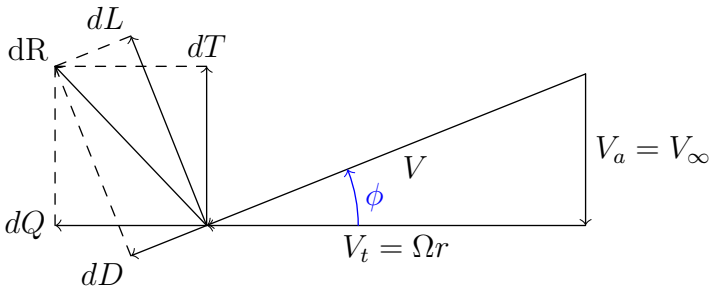


Figure 2.7: A cross-section of a segment, showing the relations between the segment lift and drag and the segment thrust and torque. The freestream flow is coming from the top of the picture. *dR* is the resultant vector sum of either segment lift and drag, or segment thrust and torque.

**Step four: find total thrust and torque of rotor**

Now the thrust and torque of each segment is known, the total thrust is found by summing the thrust of all segments of a blade, and multiplying this by the number of blades. The same procedure is used for calculating the total torque:

$$T = B \sum dT \tag{2.21}$$

$$Q = B \sum dQ \tag{2.22}$$

**Limitations**

The above BEM procedure is very basic, and does not take into account the fact that circulation goes to zero at the blade tip, and possibly at the blade root as well, depending on the local spinner geometry. Moreover it does not take into account the effect of segments on each other, which will change the induced angle of attack of each segment, changing the lift and drag of those segments. An iterative procedure is needed to do so. As can be seen in Chapter 3, this method is not accurate but for the analyzed rotor the simple BEM results are within 15% of XROTOR BEM values. A more accurate method is the minimum induced loss routine explained in the next section.

Another limitation shows up at high speeds. Propellers working at sufficiently high *rpm* and flying speed will have large tip speeds, encountering compressibility effects. If the tip speed surpasses the drag divergence Mach number, it reaches the transonic speed regime where the local airfoil drag wil increase significantly, leading to a larger power requirement. At even larger speeds in the transonic regime, the critical Mach number might be surpassed, and the development of a stretch of supersonic flow over the airfoil will seriously alter the performance. BEM codes need to have correction methods to model these effects, and in general any 3D flow caused by partial transonic flow on a blade needs to be modeled into the 2D section performance too. Most propellers and propeller-driven aircraft are designed such that flying speeds and tip speeds stay well below the critical Mach number for performance reasons.

## 2.3. MINIMUM INDUCED LOSS (MIL) ROUTINE IN BLADE ELEMENT METHODS (BEM)

A minimum induced loss routine for BEM takes into account the finite span effects on the circulation distribution and includes the viscous drag in the performance analysis. It is therefore deemed an excellent method of assessing rotor performance in a quick yet accurate way. One of the available MIL routines for BEM is the open-source code XROTOR by Drela and Youngren [18]. Drela has developed a very similar rotor and design analysis program for model airplane propellers called QPROP, which uses the same design and analysis MIL routine as XROTOR. This routine is based on the theoretical works of Betz [19], Goldstein [20], Theodorsen [21], and a modification with slight simplying assumptions to these theories as described by Larrabee [22]. The theoretical background of QPROP is given by Drela [23], and large parts are reproduced below to show how a MIL routine analyzes rotor blades.

The QPROP/XROTOR MIL blade element method is an iterative numerical method. Like most iterative methods it needs sensible starting conditions to converge at all. Rotor blades in deep stall for example are likely to lead to nonconvergence. It typically needs a small number of iterations to converge to a steady solution. A Newton iteration scheme is used, which basically uses the first derivatives of parameters to calculate the change for the new iteration. The code flexible enough that the user can input either *rpm* or advance ratio, and either thrust or power, when analyzing a rotor. A blade is modeled using different airfoil sections, and the iteration process tries to converge a certain angle $\Psi$ such that the induced efficiency is as constant as possible. Drela uses $\Psi$ instead of the circulation $\Gamma$ directly to allow much parameters to be a function of $\Psi$, as can be seen below.

**Flowfield and circulation**

At a radial distance $r$ the blade sees a velocity $W$ at an angle $\phi$ from the tangential direction. See Figure 2.8. This velocity $W$ can be decomposed in an axial component $W_a$ and a tangential component $W_t$. The rotor blades introduce axial and tangential velocity components, $v_t$ and $v_a$ in the streamtube, which give a total velocity difference $v$ which is assumed to be perpendicular to $W$. If there is an external slipstream present, which is the case for a rotor-stator system for example, a velocity vector $u$ based on components $u_t$ and $u_a$ is present too. The components of $W$ and $W$ itself can now be described:

$$W_a = V + u_a + v_a \tag{2.23}$$

$$W_t = \Omega r - u_t - v_t \tag{2.24}$$

$$W = \sqrt{{W_a}^2 + {W_t}^2} \tag{2.25}$$

The total circulation on all blades at radius $r$ is $B\Gamma(r)$. This is half the circulation on the circumferential distance at radius $r$. Introducing a circumferentially averaged tangential velocity $\bar{v}_t$:

$$2\pi r \bar{v}_t = \frac{1}{2} B\Gamma \tag{2.26}$$

$$\bar{v}_t = \frac{B\Gamma}{4\pi r} \tag{2.27}$$

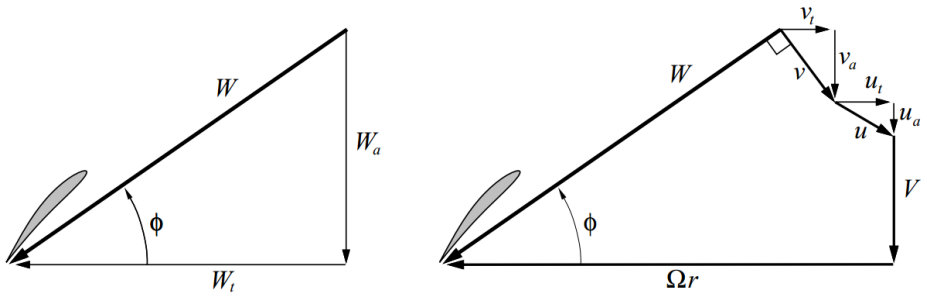


Figure 2.8: Section velocities. From [23].

$$\bar{v}_t = v_t F \sqrt{1 + \left(\frac{4\lambda_w R}{\pi B r}\right)^2} \tag{2.28}$$

Where $F$ is Prandtl's tip correction factor [24], which is an important and simple approximation to model tip losses:

$$F = \frac{2}{\pi} \arccos\left(e^{-f}\right) \tag{2.29}$$

$$f = \frac{B}{2}\left(1 - \frac{r}{R}\right)\frac{1}{\lambda_w} \tag{2.30}$$

The local wake advance ratio, which differs slightly from the rotor advance ratio, is found using the following equation:

$$\lambda_w = \frac{r}{R}\tan(\phi) = \frac{r}{R}\frac{W_a}{W_t} \tag{2.31}$$

Solving for $v_t$ and $v_a$ gives:

$$v_t = \frac{B\Gamma}{4\pi r}\frac{1}{F\sqrt{1 + \left(\frac{4\lambda_w R}{\pi B r}\right)^2}} \tag{2.32}$$

$$v_a = v_t \frac{W_t}{W_a} \tag{2.33}$$

But it should be noted that the assumption of $v$ being perpendicular to $W$ is only valid for a non-contracting helical wake and assuming that all radial stations have the same pitch. Although this assumption only holds for a Goldstein circulation distribution and lightly loaded rotors, it is gives reasonable results in general. The simplification instead of more accurate methods greatly speeds up analysis.

**Blade section geometry**

The local inflow angle $\phi$ and the blade angle $\beta$ are not equal, and the difference creates the angle of attack of the local section:

$$\begin{aligned} \alpha &= \beta - \phi \\ &= \beta - \arctan\left(\frac{W_a}{W_t}\right) \end{aligned} \tag{2.34}$$

See Figure 2.9 for an overview of the local geometry and angles. The local blade airfoil lift and drag coefficients $C_l$ and $C_d$ can now be found from polars, since the angle of attack is known and the Reynolds number can be calculated using $W$ and the local blade chord. XROTOR uses parametrized approximations with compressibility corrections for the airfoil polars. The local circulation can be found using the local lift coefficient:

$$\Gamma = \frac{1}{2} W c C_l \tag{2.35}$$

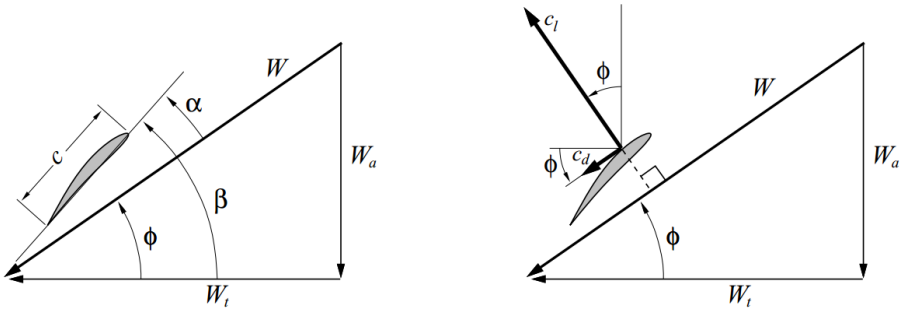


Figure 2.9: Section angles and aerodynamic vectors. The left figure shows the relations between the local velocity vector and the airfoil angle of attack. The right figure shows the direction of the aerodynamic $C_l$ and $C_d$ vectors, as they are by definition respectively perpendicular and parallel to the local velocity vector $W$. From [23].

**Blade section analysis**

The blade geometry parameters $c(r)$, $\beta(r)$, airfoil properties $C_l$, $C_d$, airspeed $V$, and rotation speed $\Omega$ have to be known to start the local section analysis. The radial circulation distribution $\Gamma(r)$ can then be calculated independently for each radius. Drela parametrizes much of the section parameters and velocities with respect to dummy angle $\Psi$ for convenience, instead of directly iterating on $\Gamma$. There is no particular reason why $\Psi$ should be chosen, and in fact this method might be a problem for values near 90°, as described in Section 2.3. See Figure 2.10 for an overview of the section velocity geometry.

All velocities found in Figure 2.10 can now be written as a function of $\Psi$:

$$U_a = V + u_a \tag{2.36}$$

$$U_t = \Omega r - u_t \tag{2.37}$$

$$U = \sqrt{{U_a}^2 + {U_t}^2} \tag{2.38}$$

$$W_a(\Psi) = \frac{1}{2} U_a + \frac{1}{2} U \sin(\Psi) \tag{2.39}$$

$$W_t(\Psi) = \frac{1}{2} U_t + \frac{1}{2} U \cos(\Psi) \tag{2.40}$$

$$v_a(\Psi) = W_a - U_a \tag{2.41}$$

$$v_t(\Psi) = U_t - W_t \tag{2.42}$$

The local angle of attack and total velocity seen by the section can also be written as function of $\Psi$:

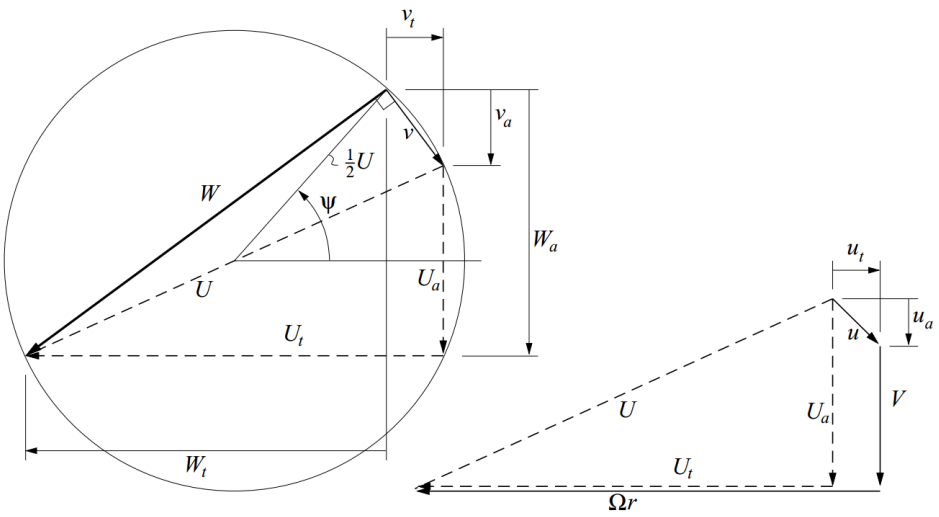


Figure 4: Velocity parameterization by the angle $\psi$.

Figure 2.10: Velocity parametrization using dummy angle $\Psi$. From [23].

$$\alpha(\Psi) = \beta - \arctan\left(\frac{W_a}{W_t}\right) \tag{2.43}$$

$$W(\Psi) = \sqrt{{W_a}^2 + {W_t}^2} \tag{2.44}$$

The local Reynolds number and local Mach number need to be calculated because XROTOR uses these parameters to estimate airfoil performance from a given airfoil polar by using scaling laws which are a function of $Re$ and $M$.

$$Re(\Psi) = \frac{\rho W c}{\mu} \tag{2.45}$$

$$M(\Psi) = \frac{W}{a} \tag{2.46}$$

The circulation is related to the tangential induced velocity $v_t$ by Equation 2.32, and parameterizing by dummy angle $\Psi$ gives:

$$\lambda_w(\Psi) = \frac{r}{R}\frac{W_a}{W_t} \tag{2.47}$$

$$f(\Psi) = \frac{B}{2}\left(1 - \frac{r}{R}\right)\frac{1}{\lambda_w} \tag{2.48}$$

$$F(\Psi) = \frac{2}{\pi}\arccos\left(e^{-f}\right) \tag{2.49}$$

$$\Gamma(\Psi) = v_t \frac{4\pi r}{B} F \sqrt{1 + \left(\frac{4\lambda_w R}{\pi B r}\right)^2} \tag{2.50}$$

To allow for a Newtonian iteration procedure, the circulation Equation 2.35 is rewritten as a residual function, which will be driven towards 0 in the iteration procedure:

$$\Re(\Psi) = \Gamma - \frac{1}{2} W c C_l(\alpha, Re, M) \tag{2.51}$$

The Newtonian residual is updated using the following function:

$$\delta\Psi = -\frac{\Re}{\frac{d\Re}{d\Psi}} \tag{2.52}$$

$$\Psi \leftarrow \Psi + \delta\Psi \tag{2.53}$$

**Thrust and torque**

First the section lift and drag are calculated over the full annulus with width $dr$. Therefore the result is multiplied by the number of blades $B$.

$$dL = B\frac{1}{2}\rho W^2 C_l c\,dr \tag{2.54}$$

$$dD = B\frac{1}{2}\rho W^2 C_d c\,dr \tag{2.55}$$

The thrust and torque of each annulus can be found from $dL$ and $dD$ using the local blade angle $\phi$.

$$\begin{aligned} dT &= dL\cos(\phi) - dD\sin(\phi) \\ &= B\frac{1}{2}\rho W^2 \left(C_l\cos(\phi) - C_d\sin(\phi)\right) c\,dr \end{aligned} \tag{2.56}$$

$$\begin{aligned} dQ &= \left(dL\sin(\phi) + dD\cos(\phi)\right) r \\ &= B\frac{1}{2}\rho W^2 \left(C_l\sin(\phi) + C_d\cos(\phi)\right) c\,r\,dr \end{aligned} \tag{2.57}$$

From Figure 2.11 it is clear that the tangential and axial components of $W$ are a function of $\phi$:

$$W\cos(\phi) = W_t \tag{2.58}$$

$$W\sin(\phi) = W_a \tag{2.59}$$

The trust and torque components of each annulus (note again the multiplication by $B$) can be expressed using these terms:

$$dT = \rho B\Gamma\left(W_t - \epsilon W_a\right) dr \tag{2.60}$$

$$dQ = \rho B\Gamma\left(W_a + \epsilon W_t\right) r\,dr \tag{2.61}$$

The parameter $\epsilon$ is a measure for the 2D aerodynamic performance of the airfoil section, written as the inverse lift-to-drag ratio:

$$\epsilon = \frac{C_d}{C_l} \tag{2.62}$$

The local or section efficiency of a section from that annulus is now given by:

$$\eta = \frac{V\,dT}{\Omega\,dQ} \tag{2.63}$$

Inserting Equations 2.60 and 2.61 into Equation 2.63 results in an expression for the section efficiency as a function of the section drag-to-lift ratio $\epsilon$.

$$\begin{aligned}\eta &= \frac{V}{\Omega r}\frac{C_l\cos(\phi) - C_d\sin(\phi)}{C_l\sin(\phi) + C_d\cos(\phi)} \\ &= \frac{V}{\Omega r}\frac{W_t - \epsilon W_a}{W_a + \epsilon W_t}\end{aligned} \tag{2.64}$$

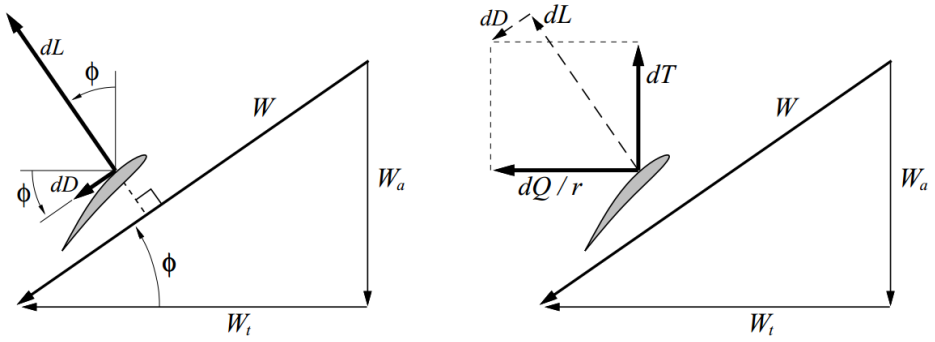


Figure 2.11: Blade section thrust and torque. From [23].

**Total thrust, torque, and efficiency**

Integrating Equations 2.60 and 2.61 along the blade and multiplying by the number of blades gives the total thrust and torque of the rotor:

$$\begin{aligned}T &= \rho B\int_0^R \Gamma\left(W_t - \epsilon W_a\right)dr \\ &\simeq \rho B\sum_r \Gamma\left(W_t - \epsilon W_a\right)\Delta r\end{aligned} \tag{2.65}$$

$$\begin{aligned}Q &= \rho B\int_0^R \Gamma\left(W_a + \epsilon W_t\right)r\,dr \\ &\simeq \rho B\sum_r \Gamma\left(W_a + \epsilon W_t\right)r\Delta r\end{aligned} \tag{2.66}$$

The overall efficiency of the rotor then becomes:

$$\overline{\eta} = \frac{VT}{\Omega Q} \tag{2.67}$$

**Minimum Induced Loss condition**

A minimum induced loss propeller blade is the rotating version of a minimum induced (elliptically loaded) wing. It has a spanwise or radially constant induced drag over lift ratio, equal to an initially unknown value of $\overline{\eta}$. With $\epsilon = 0$ (an airfoil with no drag) in Equation 2.64 an initial guess is found:

$$\frac{V}{\Omega r}\frac{W_t}{W_a} = \overline{\eta} \tag{2.68}$$

A value for an overall lift coefficient $C_L$ is needed to find the overall circulation distribution which leads to this average $C_L$. During the iteration process XROTOR tries to find

a circulation which matches this overall $C_L$. While this works well for a wide range of propeller design conditions, the above procedure has its limits when used for stator design, as explained below.

**Implications for stator design**

Suppose that there is no rotor present in front of the stator. The stator then simply sees an uniform flow field with freestream velocity (no hub effects taken into account). Looking at the velocity diagram of Figure 2.8, absence of rotor slipstream means that $u = 0$. With no rotational speed, $\Omega = 0$, and what is left is a velocity triangle composed of $W$, $V$, and $v$. Velocity $V$ has to be vertical in this picture, since it is still in the freestream direction. This does not mean that $v = 0$ and $W = V$, but since there is no slipstream to be countered, there is no incentive for the stator blades with symmetric airfoils to be set at a nonzero angle of attack. The stator-only case with then has $\Psi = 0$, and from this it follows that $W_t = 0$ too. The overall efficiency of Equation 2.68 becomes zero too; $\overline{\eta} = 0$. This is fully correct since the stator blades are not imposing a tangential slipstream on the flow.

However, XROTOR does need an initial value of $\overline{\eta}$ to start iterating for the MIL condition. With a specified nonzero $C_L$ and an initial overall efficiency $\overline{\eta} = 0$, it is clear that this condition cannot be met easily: the former constraint asks for a nonzero $v$, which would make $\Phi$ nonzero too. This in turn would mean that $W_t$ is nonzero too, and a nonzero $\overline{\eta}$ is found which contradicts the latter (initial) constraint. It might very well be this initial constraint which might make XROTOR behave erratically when designing a MIL stator. Figure 2.12 shows a redrawn velocity diagram of Figure 2.10, for the case where there is no external (rotor) slipstream present, but a finite $C_l$ is used as input, such that there is a finite downwash $v$ off the blade. $W_t$ is nonzero, thus the efficiency can be calculated. A case with external rotor slipstream $u$ present is shown in Figure 2.13, and now it is possible to have the paradox of finite circulation with $\overline{\eta} = 0$. Note how $u$ has forced the vectors $W$ and $v$, which are perpendicular, to move such that $W$ has become parallel to freestream velocity vector $V$. Consequently $W_t = 0$, which prevents $\overline{\eta}$ to be nonzero.

Unfortunately it is rather impossible to prove that this issue is the exact cause of XROTOR's strange stator-design behavior. Maybe there are other contributing issues too, such as values getting so small that they get affected by machine accuracy during mathematical operations. These values are not part of the output and are thus not seen by the user. Looking back at Drela's decision to iterate on $\Psi$, it might be worth rewriting the code to directly iterate on the circulation $\Gamma$. This would almost certainly prevent the circulation becoming zero when there is a finite lift coefficient, at the expense of code simplicity, but it does not change the MIL design/analysis routine in general.

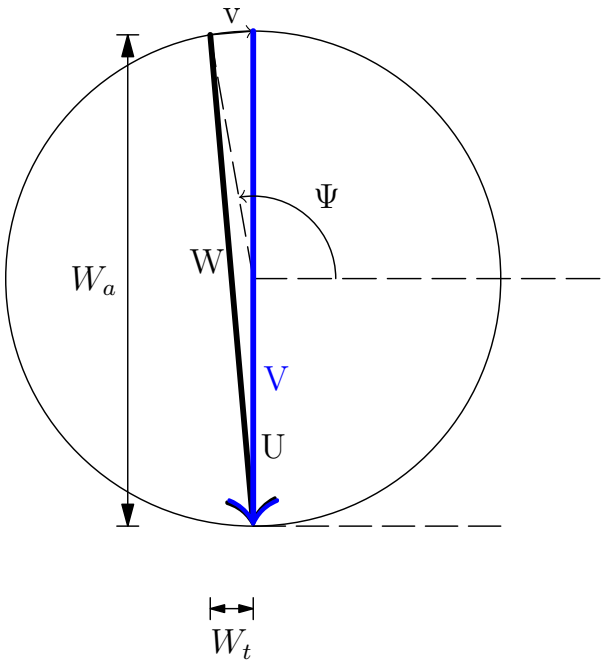


Figure 2.12: Velocity diagram, of stator blade in an undisturbed flow. Vectors $W$ and $v$ are perpendicular.

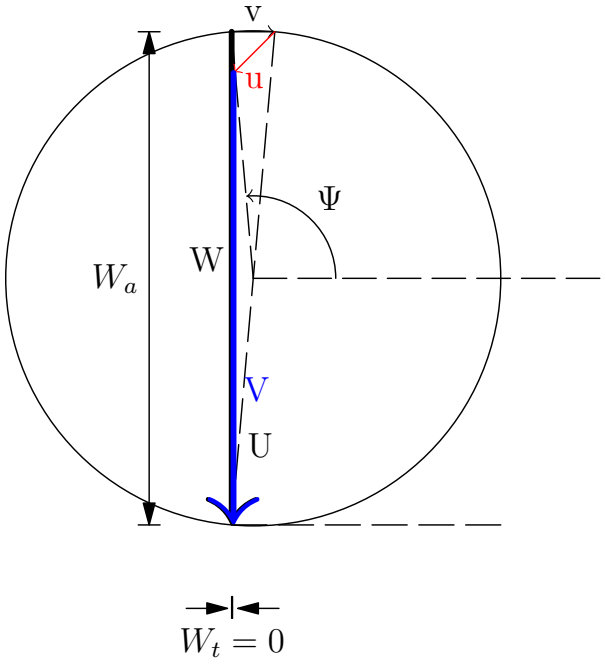


Figure 2.13: Velocity diagram, of stator blade in a rotor slipstream. Freestream velocity $V$ is now parallel to and lies on top of blade velocity $W$. Vectors $W$ and $v$ are perpendicular. Vector $u$ is an incoming slipstream velocity vector.

## 2.4. ROTOR-STATOR SYSTEM GEOMETRY

The rotor-stator system consists of an unswept stator mounted coaxially behind an unswept rotor. Figure 2.14 shows such an arrangement, with the rotation axis at the bottom. Rotor and stator can have different tip radii and hub radii, which affects the slipstream diameter as explained in Appendix C. The figure shows how the rotor-stator system used in this thesis is defined. The spacing refers to the axial distance between the $0.25c$ radial lines of the unswept rotor and unswept stator. With the stator tip radius defined equal or smaller than the rotor slipstream radius, the rotor slipstream radius is always seen as the larger one of the two and becomes the system slipstream radius.

If the flow is assumed incompressible, it is clear that the step in hub radius has a a large effect on the streamtube radius. A step as depicted in Figure 2.14 shows an increase in hub radius, which will push the flow radially outward. In Appendix C it is explained how this effect is incorporated into the rotor-stator analysis software program.

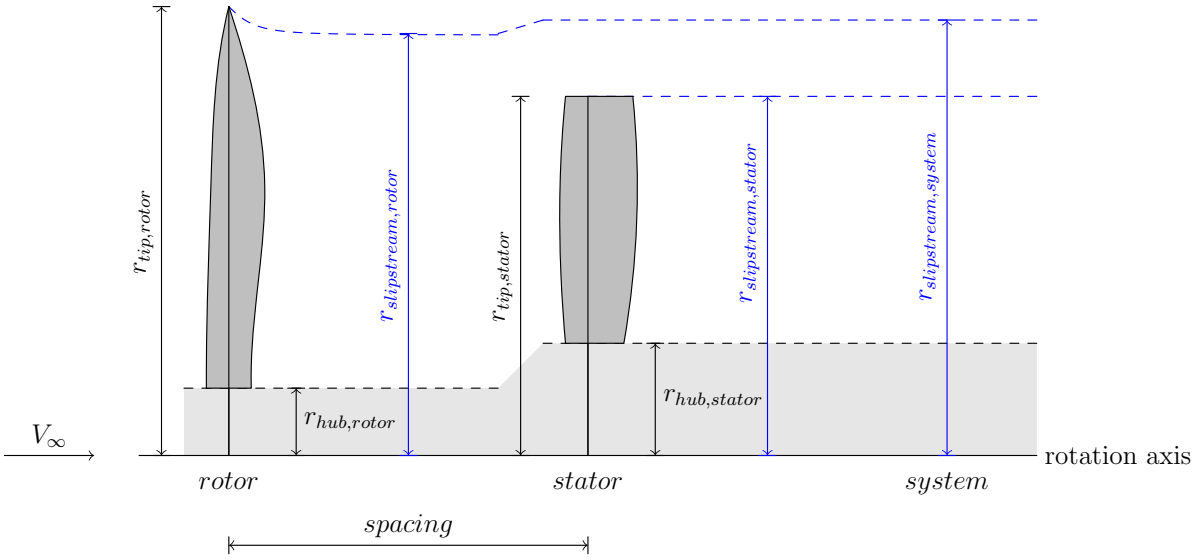


Figure 2.14: Geometry of rotor-stator system, indicating various radii and rotor-stator spacing.

# 3

# STATOR DESIGN AND ANALYSIS ISSUES

## 3.1. THE IDEAL ZERO SWIRL SLIPSTREAM

A propeller or rotor generates a slipstream with a swirl; a wake which is slowly rotating. When introducing a stator behind the rotor, a good question is if there can actually be a zero swirl slipstream behind this system, i.e. a slipstream without any tangential components. When the stator is cropped, a part of the rotor slipstream falls outside the stator radius and therefore cannot be modified by the stator. This means that while a perfect zero system tangential slipstream is very difficult (if possible at all) to achieve for stators equal or larger than the rotor slipstream radius, this is definitely impossible in cases where the stator radius is smaller than the rotor slipstream radius: cases which are of most interest in aircraft rotor-stator design. Operational changes in angle of attack and related rotor tip vortex interactions or prevention of aerodynamic noise are reasons to clip the stator radius to a radius smaller than the rotor slipstream radius.

When there is a nonzero swirl at the stator tip radius, for example with a cropped stator, the stator tip needs a finite circulation to negate all swirl. However, this is physically not possible, since the circulation goes to zero at the stator tip as there is no lifting surface beyond it. This is the very reason why a cropped stator will never remove all swirl from a slipstream.

## 3.2. FOKKER F50 AIRCRAFT AND ROTOR

A suitable rotor should be available in order to design a set of stators for a sensitivity analysis. The succesful Fokker F50 turboprop aircraft is used as an example. First a general description of the aircraft is given, after which the modeling of the rotor is explained. The next section contains the parameter sweep analysis of Fokker F50 rotor-stator combinations.

**The Fokker F50 aircraft**

The Fokker F50 is a very successful turboprop aircraft from Fokker in the Netherlands. It first flew on 28 December 1985, and 213 units were produced before the Fokker company went bankrupt in 1997. F50's are still flying around, many as cargo aircraft, due to the short take-off and landing distances possible with the F50. The F50 was also known for its quiet cabin, as various measures were taken to suppress cabin noise. For instance, the rotor

*rpm* was mostly kept at a very constant value of $17Hz = 1020rpm$ such that tuned dampers between the wing and the cabin could reduce vibrations. The propellers are thus variable in pitch. The fact that the F50 is still a widely used turboprop aircraft makes it an excellent choice of study for a possible stator retrofit to increase its economic lifespan. The four Fokker F60's in existence are stretched versions of the Fokker F50.


Figure 3.1: Fokker F50 during climb, from [25].

**Comparison XPROP OJF wind tunnel data and XPROP modeled in XROTOR**

Geometry data of the Dowty-Rotol propellers used on Fokker F50 aircraft was not available. NLR has performed wind tunnel tests [26] on a small propeller called XPROP (not to be confused with software programs XFOIL and XROTOR). This propeller was a 1 : 9 scale model of a Dowty Rotol 6-bladed aircraft propeller. It was assumed that the XPROP blade geometry could therefore directly be scaled to the full-size Fokker F50 dimensions, as the blade planform made clear that it is virtually the same rotor (see Figure 3.2).

Data from a DNW wind tunnel test (See also Janssen [27]) includes graphs of XPROP wind tunnel tests in the OJF facility at Delft University of Technology. The rotor was tested at free-stream speeds of 28 and $60m/s$, and 5 different blade angle settings. The standard setting was 30°, and this setting was also used for the XROTOR model of XPROP. Because no extensive performance data is available of the F50 rotors, the performance of the XPROP model in XROTOR was compared with the NLR wind tunnel test data to have an idea about the performance difference. A comparison for the rotor thrust coefficient and power coefficient was made by overlaying performance graphs of both rotors. The results can be seen in Figures 3.3 and 3.4. The match is not particularly strong, but is still within a 2° blade angle change at high $J$, comparing with the original NLR 'shoptest' data. For low advance ratios, $J < 0.60$, the match is progressively worse. The cause must primarily be sought in 3D flow effects and blade stall over the real rotor versus the blade element method analysis. Correcting for this however is difficult, as 3D hub effects are difficult to model into a 2D BEM. Correction models such as proposed by Snel et al. [28] try to model 3D-effects on wind turbine rotor blades by changing the 2D $C_L$ values, but do not incorporate radial flow components as created by different rotor and stator hub radii (such as the APIAN rotor-stator system described in this thesis).

It is very interesting to note that the cross-over point for both $C_T$ and $C_P$ graphs occurs roughly near $J = 0.70$, which is close to the design cruise $J$ of the actual F50 rotor as mentioned below in Section 3.2. However, this is suspected to be purely a coincidence since there is no aerodynamic reason why a cross-over should happen at that particular $J$. Performance data of XPROP compared to the full-scale F50 rotor might yet be quite accurate in the direct neighborhood of the F50 rotor cruise design advance ratio.

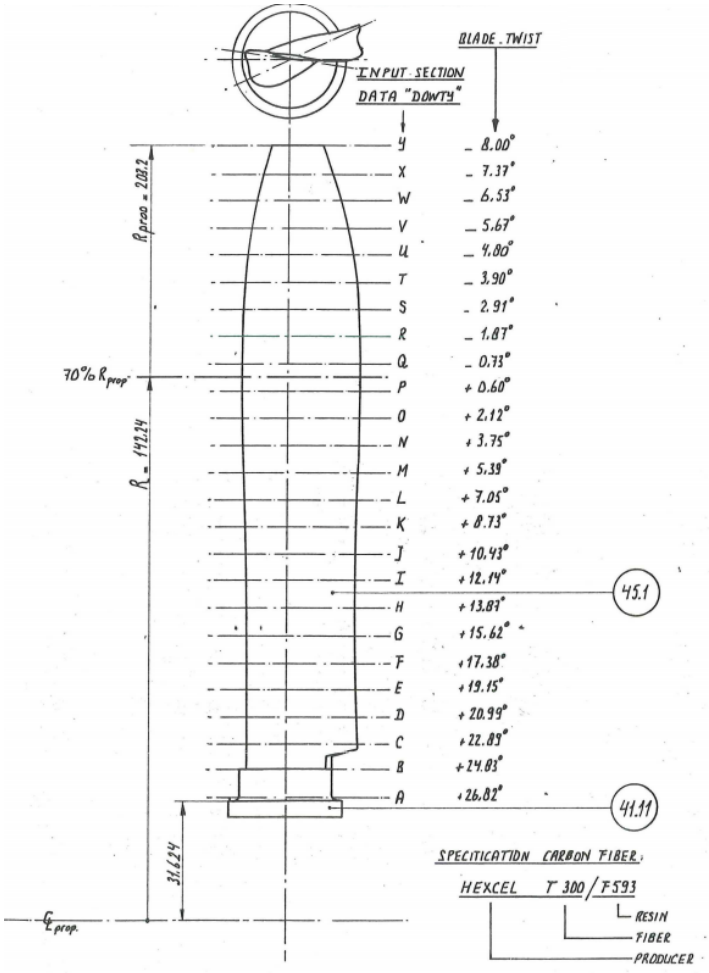


Figure 3.2: Wind tunnel model blade plan-form and twist angles, from [26].

**Analysis of F50 Dowty-Rotol 6-bladed rotor modeled from XPROP geometry**

Based on the rather acceptable match in performance of the XPROP rotor near the cruise advance ratio of the F50 rotor, the XPROP model was used to create a F50 rotor model by scaling up by a factor of 9. In XROTOR two F50 rotors were created, which are geometrically similar but only the pitch angle is different. As explained earlier, the F50 is assumed to have a constant *rpm* for noise reasons. XROTOR was used to automatically find the corresponding blade pitch to match the constant *rpm* but different power settings of the rotor in cruise condition and take-off condition. The blade geometry input consists of 25 stations equally spaced along the radius. Airfoil coordinates were also specified for all radial stations, of which only the ones at uneven blade stations are used as XROTOR has a limit

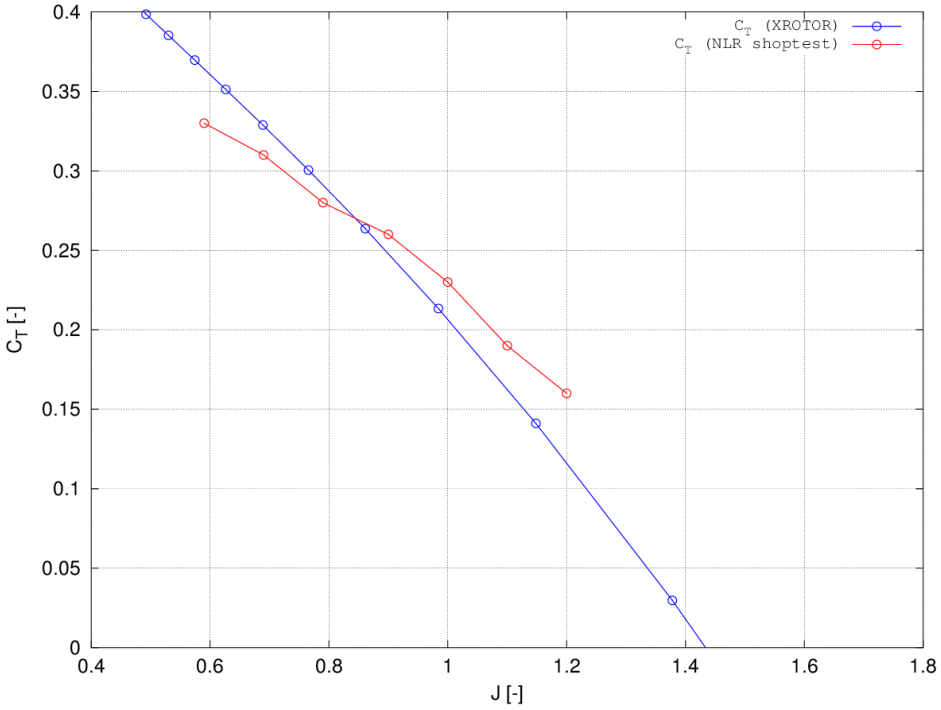


Figure 3.3: Comparison of NLR wind tunnel data (digitized by Janssen) and XROTOR calculated $C_T$ values for XPROP rotor with a blade angle of 30°, tested at $V = 28 m/s$.

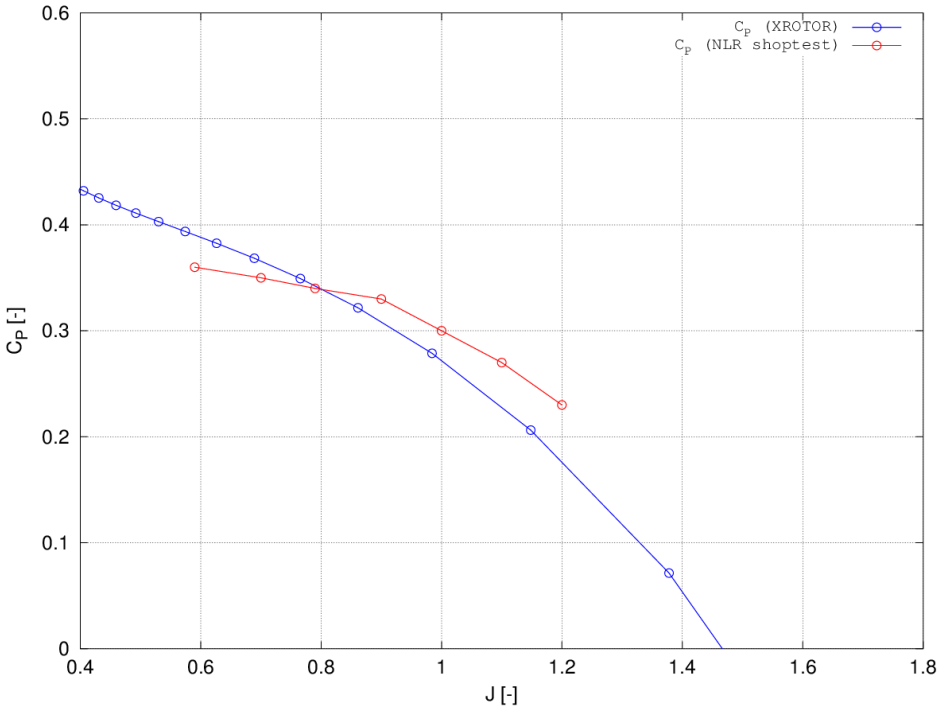


Figure 3.4: Comparison of NLR wind tunnel data (digitized by Janssen) and XROTOR calculated $C_P$ values for XPROP rotor with a blade angle of 30°, tested at $V = 28 m/s$.

to the amount of airfoil sections it can handle. A blade thus consists of 25 stations with *r/R*, *c/R*, and blade twist angle specified, and the airfoil performance data belonging to 13 stations along the full blade length.

A 3D plot of a F50 rotor blade at cruise blade angle setting was plotted in Figure 3.5. A picture of a real Dowty-Rotol F50 rotor can be seen in Figure 3.6. This was done to be able to simulate propeller performance at cruise and TO (take-off) conditions. The F50 is known for its low cabin noise, which was partly realized by using dampers between the wing and fuselage which are tuned to the rotor *rpm* of $17 Hz$ or $1020 rpm$. Therefore, for both cases a *rpm* of 1020 was assumed. Various sources mention a cruise speed around $270 kts$ or $140 m/s$, while the speed at take-off (rotation) is about $120 kn$ or $62 m/s$. Engine power figures from various on-line sources note about $2250 hp$ during TO and $1725 hp$ during cruise. Cruise altitude can be as high as $7.62 km$, which was chosen as the design cruise altitude. This input data is displayed in a neat table; Table 3.1. The stator hub radius was set equal to the rotor hub radius, which is a valid assumption regarding the rather cylindrical nacelles as seen in Figure 3.1. The engine nacelles protrude far out from the wing leading edge, which also offer ample place for stator vanes. Due to the engine air intake location, care should be taken to prevent excessive interference drag between the stator vanes and the nacelle. This nacelle is not taken into account in this analysis. For a first analysis this is deemed acceptable, as the air intake covers only part of the circumference of the hub, and the intake itself relieves the blockage effect anyway. Figure 3.7 shows how the rotor-stator combination with the F50 engine nacelle with air inlet is modeled.

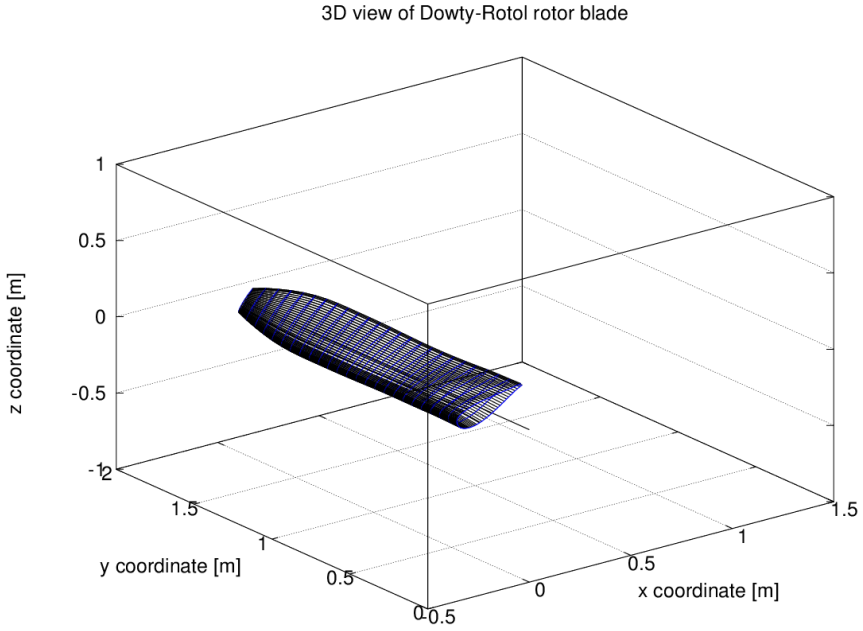


Figure 3.5: 3D wireframe model of a Dowty-Rotol F50 rotor blade set at cruise pitch, scaled from XPROP data. It is very similar to the real Dowty-Rotol blades seen in Figure 3.6 for example.

Figure 3.6: Dowty-Rotol rotor on left wing of a Fokker F50. Photo by author.

Table 3.1: Table containing XROTOR input data and performance data of the two F50 flight operating conditions.

| **Parameter** | **TO (take-off)** | **Cruise** | **Unit** |
|---|---|---|---|
| $h$ | 0.000 | 7.620 | $[km]$ |
| $\rho$ | 1.226 | 0.550 | $[kg/m^3]$ |
| $V_\infty$ | 62.0 | 140.0 | $[m/s]$ |
| $V_\infty$ | 0.1824 | 0.4523 | $[M]$ |
| $P$ | 1678 | 1125 | $[kW]$ |
| $rpm$ | 1020 | 1020 | $[rpm]$ |
| $J$ | 0.9971 | 2.2516 | $[-]$ |
| $T$ | 20.1395 | 6.9822 | $[kN]$ |
| $Q$ | 15.7 | 10.5 | $[kNm]$ |
| $C_T$ | 0.31760 | 0.24547 | $[-]$ |
| $C_P$ | 0.42557 | 0.63607 | $[-]$ |
| $\eta$ | 0.7441 | 0.8689 | $[-]$ |
| $Re(0.7\ r/R)$ | 3.54E6 | 1.08E6 | $[-]$ |

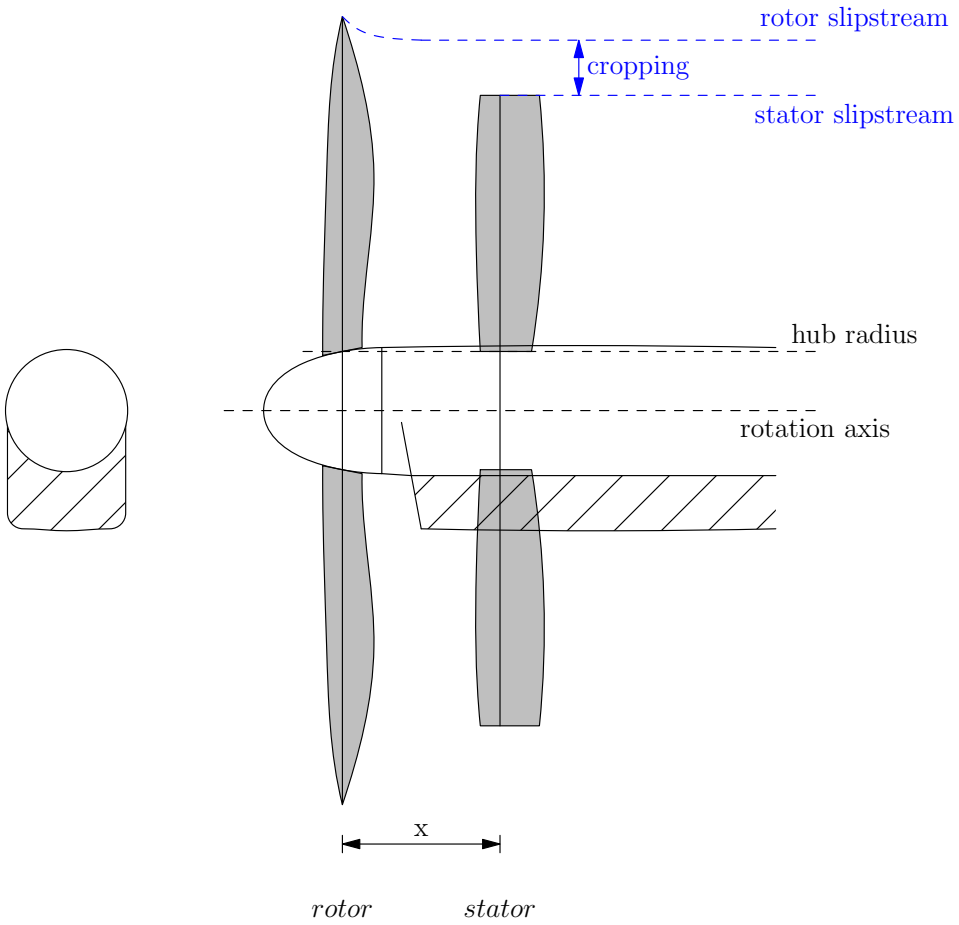


Figure 3.7: Schematic view of F50 rotor-stator combination and nacelle; front view of nacelle only and side view of nacelle with rotor and stator. The hatched part is the air inlet and oil cooler which is left out in the analysis, giving a cylindrical hub. Rotor-stator spacing $x$ is often given as ratio of rotor tip radius: $r/R$. The definition of (stator) cropping used in this document can also be seen.

## 3.3. F50 STATOR PARAMETER SWEEP

In order to assess the sensitivity of a BEM code for the design of a stator, the XROTOR BEM code is used together with the author's code for rotor-stator interaction, as found in Appendix C. XROTOR is given a very low *rpm* and very low $P$ in order to model a stator as a very slowly rotating propeller. For the parameter sweep, these values are given as ratios with respect to the respective rotor values, as can be found in Appendix B. A comparison with a simple BEM method is made to see if the stator design of XROTOR is plausible, and conclusions about the use of XROTOR BEM are given at the end.

**Varying power ratio**

A comparison of five power ratio settings is given below in Table 3.2, and the accompanying stator designs can be found in Figure(s) 3.8. The table tells that the power ratio has some effect on the propulsion efficiency increase, but there is no linear correlation: the maximum $\Delta\eta$ occurs not the maximum or minimum power ratio. From Figure 3.8 it is clear that XROTOR decreases chord size when the power ratio increases (and therefore the absolute stator power value decreases). The $\Delta\eta$ behavior does not really match this linear trend, see also Figure 3.9, and the differences must be sought in subtle changes in blade angle distributions and Reynolds number effects with varying chord sizes, as these are the only parameters which change between different designs in this comparison and which can influence the circulation distribution.

Figure 3.10 shows the slipstream profiles of power ratio cases 500 and 2000 from Table 3.2. At first glance the stator tangential slipstream profiles seem rather similar. However, the magnitude of this component differs greatly, which seems to be a direct result of the large difference in chord size, as blade angles are rather similar for all stator designs of this analysis case. Consequently, the system tangential slipstreams are very different too, but the efficiency increase $\Delta\eta$ is (nearly) equal. It must be concluded that the tangential slipstream component is not the only significant contributor to $\Delta\eta$. It is assumed that the circulation distribution in both cases has about the same induced drag and same thrust, leading to rather similar effects on the overall slipstream.

Table 3.2: Table showing the increase in propulsion efficiency of a rotor-stator system over a rotor standalone, with constant design and analysis *rpm* ratios, $C_L = 0.25$, $J = 2.2516$.

| **Parameter** | **Value** | **Value** | **Value** | **Value** | **Value** | **Unit** |
|---|---|---|---|---|---|---|
| Power ratio | 500 | 750 | 1000 | 1500 | 2000 | [-] |
| Power | 2.2500 | 1.5000 | 1.1250 | 0.7500 | 0.5625 | [kW] |
| Design *rpm* ratio | 1000 | 1000 | 1000 | 1000 | 1000 | [-] |
| Design *rpm* | 1.020 | 1.020 | 1.020 | 1.020 | 1.020 | [*rpm*] |
| Analysis *rpm* ratio | 1000 | 1000 | 1000 | 1000 | 1000 | [-] |
| Analysis *rpm* | 1.020 | 1.020 | 1.020 | 1.020 | 1.020 | [*rpm*] |
| $\Delta\eta$ | 0.78 | 1.29 | 1.23 | 1.02 | 0.78 | [%] |

**Varying design and analysis *rpm***

In the same way as the variation of power ratio was analyzed, the variation of design and analysis *rpm* was analyzed too, to see if the *rpm* has a significant effect on performance and

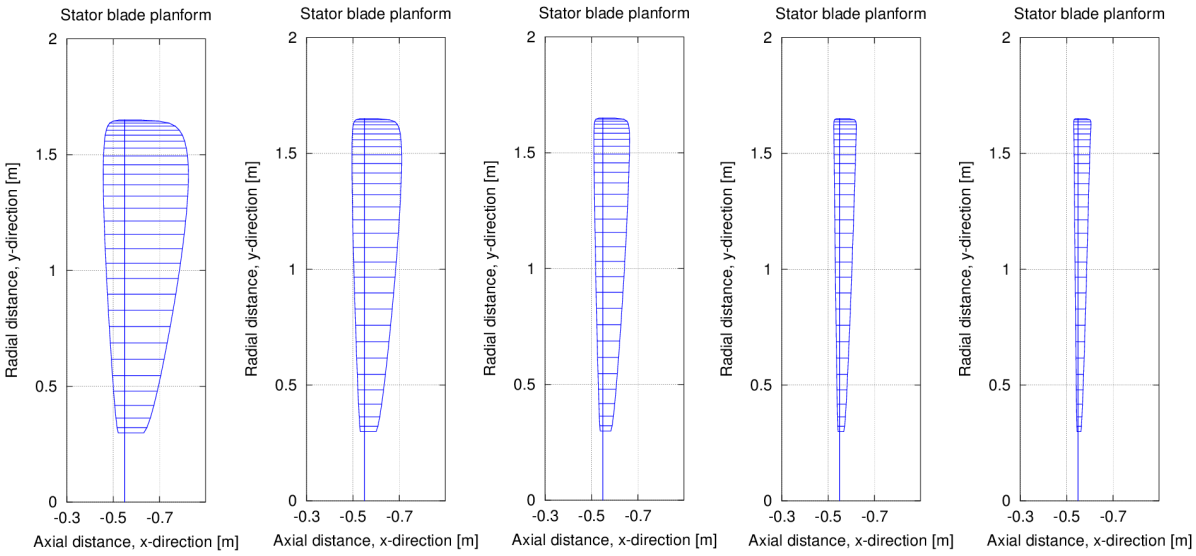


Figure 3.8: Planforms of stator designs with power ratios of resp. 500, 750, 1000, 1500, and 2000, see Table 3.2 for more data.

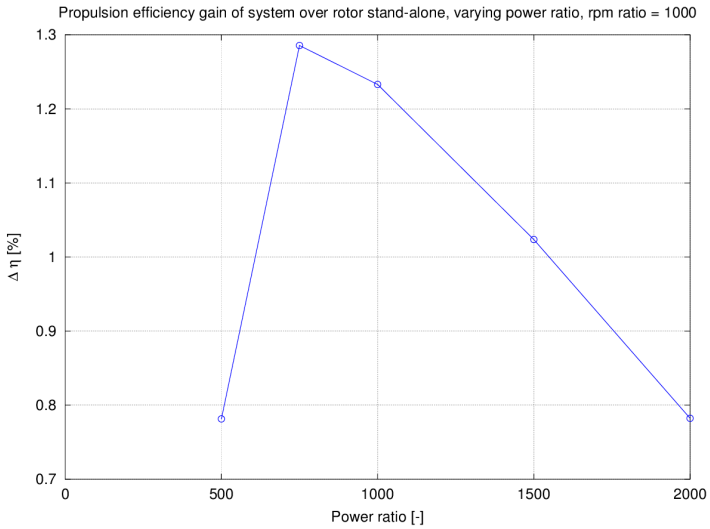


Figure 3.9: Graph of propulsion efficiency increase versus power ratio, belonging to Table 3.2.

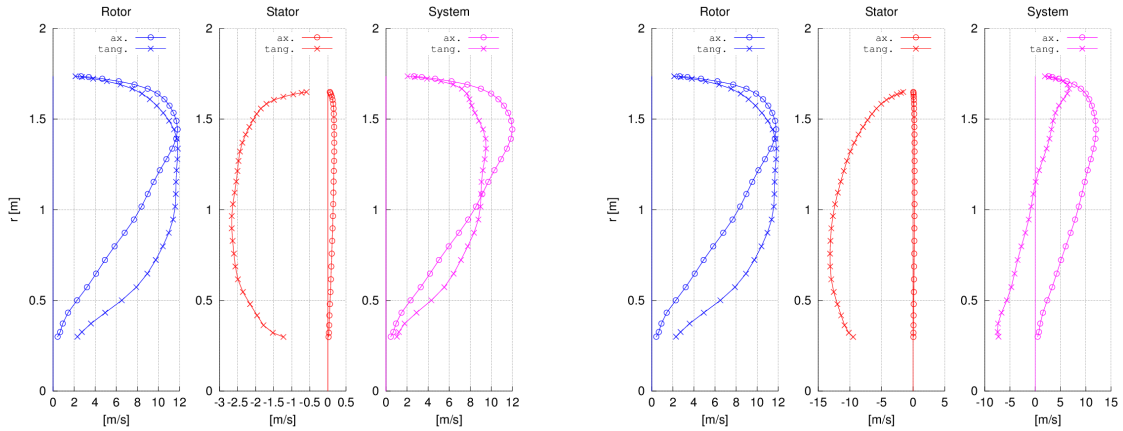


Figure 3.10: Slipstream profiles of stator designs with power ratios of resp. 500 and 2000. Belongs to Table 3.2, and Figure 3.8. Note how the stator tangential velocity distributions of both cases have roughly the same shape, but differ significantly in magnitude, which seems to be directly related to the chord size of both stator designs.

stator geometry. Both *rpm* ratios were set equal to each other, to not further complicate the situation; XROTOR should be able to analyze a stator at the same low *rpm* as was used to design the stator. Table 3.3 neatly shows the parameters and performance data. Again $\Delta\eta$ hovers around 1% at rotor $J_{design}$ and increases slightly with lower $J$, with an order of magnitude in minimum and maximum *rpm* analyzed for a given power ratio. See Figure 3.12. At first there seems to be not much difference between these stator designs. But one look at Figure 3.11 tells a whole different story: the chord distributions are clearly different for each case. In particular the two stator designs on the left ($rpm = 100, rpm = 500$) show an interesting difference. The overall planform changes from an 'inverted knotted triangle' (base at the stator tip, the knotted end pointing towards the hub) into a 'knotted triangle' with the broad end near the hub, which looks almost rectangular. Yet cases $rpm = 100, rpm = 1000$ have nearly the same change in propulsion efficiency for extremely different chord distributions. XROTOR does not have an option to design a MIL blade with constant or given chord. The program by the author contains a simple routine to design a constant-chord blade, with a blade angle setting according to simple BEM. However, such a stator results in nonconvergence in most XROTOR analyses, and therefore cannot be used. With the chord distribution thus specified by the MIL routine, the difference in performance seems to be caused by the blade angle distribution. This is not true: the wide blade has blade angles of up to 1° larger than the thin blade, where the opposite is expected to achieve a similar lift coefficient. The case with a *rpm* ratio of 250 shows a very small chord and the $\Delta\eta$ is rather low compared to the other cases.

This might indicate a 'turning point' where XROTOR's design routine switches to different chord distributions trying to satisfy MIL requirements, as the largest chords are suddenly found near the root of the blade instead of near the tip. Figure 3.13 shows the slipstream profiles of *rpm* ratio cases 100 and 1000 from Table 3.3. The left subfigure, with the low *rpm* ratio, shows an almost linear stator tangential velocity profile, which corresponds fully with the chord distribution at nearly constant $\beta$. The system tangential slipstream in this case is still substantial. The right subfigure shows the other case, and it is clear that the designed stator does a much better job of removing rotor swirl. Note that both cases show

nearly equal $\Delta\eta$, just like the previous analysis case.

Clearly the *rpm* difference is important with respect to the rotor slipstream velocities. Considering the anomaly found in the mathematics behind XROTOR's analysis and design procedure in Section 2.3, the *rpm* ratio gives different starting points from where XROTOR cannot really find a true optimized MIL blade.

Table 3.3: Table showing the increase in propulsion efficiency of a rotor-stator system over a rotor standalone, with constant power ratio, $C_L = 0.25$, $J = 2.2516$.

| **Parameter** | **Value** | **Value** | **Value** | **Value** | **Value** | **Unit** |
|---|---|---|---|---|---|---|
| Power ratio | 500 | 500 | 500 | 500 | 500 | [-] |
| Power | 2.2500 | 2.2500 | 2.2500 | 2.2500 | 2.2500 | [kW] |
| Design *rpm* ratio | 100 | 250 | 500 | 750 | 1000 | [-] |
| Design *rpm* | 10.200 | 4.080 | 2.040 | 1.360 | 1.020 | [*rpm*] |
| Analysis *rpm* ratio | 100 | 250 | 500 | 750 | 1000 | [-] |
| Analysis *rpm* | 10.200 | 4.080 | 2.040 | 1.360 | 1.020 | [*rpm*] |
| $\Delta\eta$ | 0.79 | 0.38 | 1.01 | 1.28 | 0.78 | [%] |

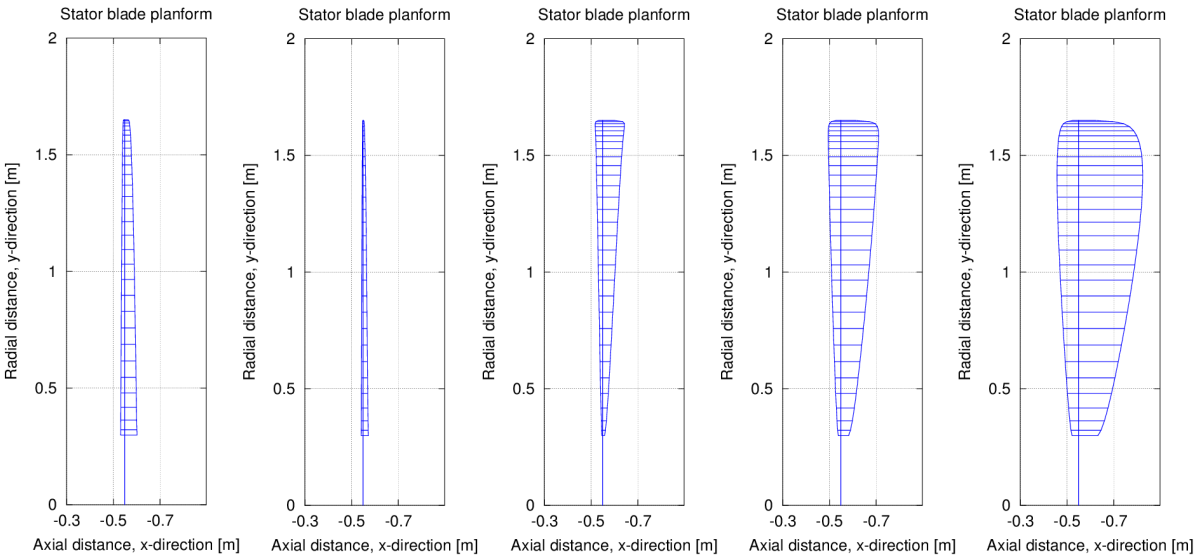


Figure 3.11: Planforms of stator designs with *rpm* design and analysis ratios of resp. 100, 250, 500, 750, and 1000, see Table 3.3 for more data.

**Stator blade performance validation**

In the foregoing sections it can be read that XROTOR is capable of designing stator blades, albeit not certain if these designs are truly optimal. To find out if the blade analysis by XROTOR is accurate, a back-of-the-envelope calculation is made. According to Tables 3.2 and 3.3, the blade with a power ratio 750 and design and analysis *rpm* ratios of 1000 gives the largest efficiency increase, and will therefore generate a substantial amount of thrust. This blade design is chosen as a validation case. According to the XROTOR `*.writ` output file, the 6-bladed rotor generates a thrust of $T = 126.0[N]$, and a torque of $Q = [4660Nm]$. Per blade this is $T_{blade} = 21[N]$ and $Q_{blade} = 776.7[Nm]$. The ambient conditions are: $V =$

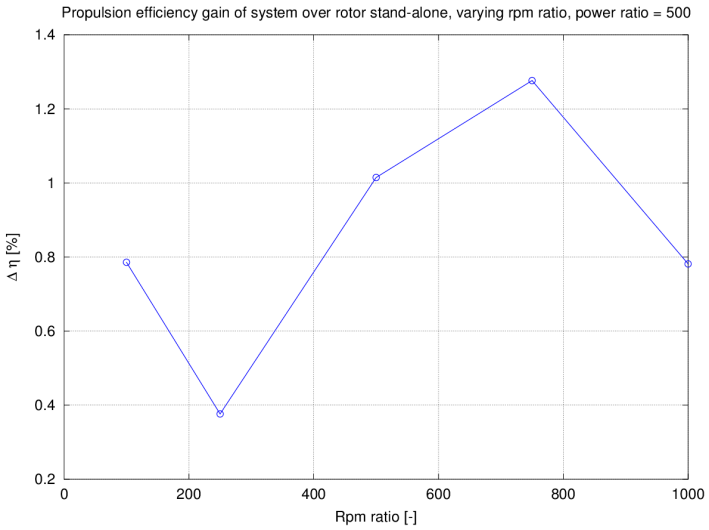


Figure 3.12: Graph of propulsion efficiency increase versus *rpm* ratio, belonging to Table 3.3.

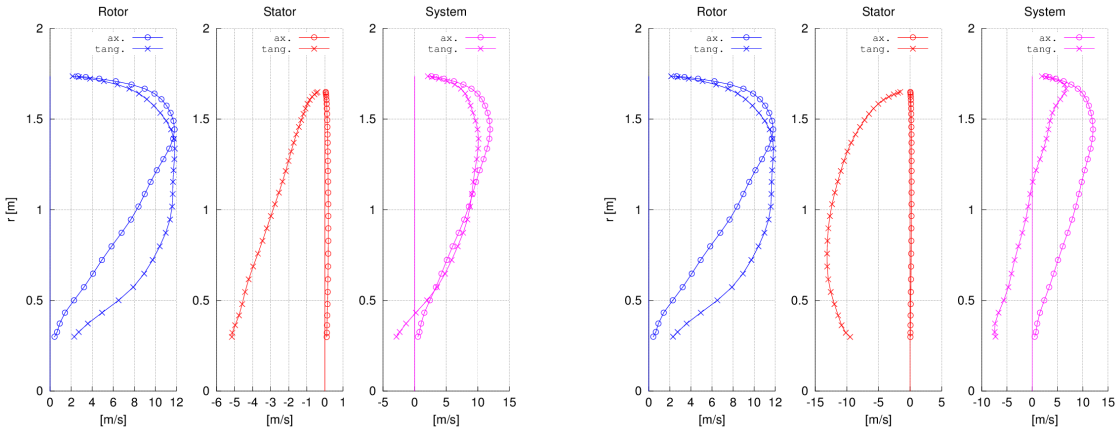


Figure 3.13: Slipstream profiles of stator designs with design and analysis *rpm* ratios of resp. 100 and 1000. Belongs to Table 3.3, and Figure 3.11. Note how the stator and system tangential velocity distributions (resp. red and magenta) are radically different, yet the efficiency increase $\Delta\eta$ as seen in the Table are nearly equal.

140.0$[m/s]$, $\rho = 0.550[kg/m^3]$, which are representative for a Fokker F50 Dowty-Rotol rotor in at cruise conditions, as used elsewhere in this document.

First a back-of-the-envelope calculation of the rotor blade at the same ambient conditions is made, to see if the method has any validity. A blade is crudely modeled as three sections by the method described in Section 2.2, with the only difference being that radial segment $dr$ is placed with its center at radius $r$, to avoid errors to get too large with such small number of segments. An overview of the three-section geometry can be seen in Figure 3.14.

Three sections are analyzed, at 29, 50, and 70% radius. By estimating the blade and rotor thrust and torque and comparing these with the XROTOR values, a validation of the accuracy can be made. Table 3.4 gives the results of the simple BEM analysis for the F50 rotor, at $J = 2.2516$. Note that for the rotor the exact airfoil shapes are not known since interpolation between other section's airfoils would be necessary. Here only the XROTOR calculated rotor airfoil $C_l$ and $C_d$ data is shown. The rotor thrust data are remarkably similar, the difference is less than 5%. The torque however, has about 30% difference. The extra multiplication by the local segment radius in the torque calculation of Equation 2.61 might add extra inaccuracy compared to the thrust calculation. Since the thrust values agree so well, the stator is also modeled using the same simple BEM. Because the stator uses a NACA 0009 airfoil, the $C_l$ and $C_d$ values can be calculated from BEM by using XFOIL, and compared to the XROTOR values as extra validation.

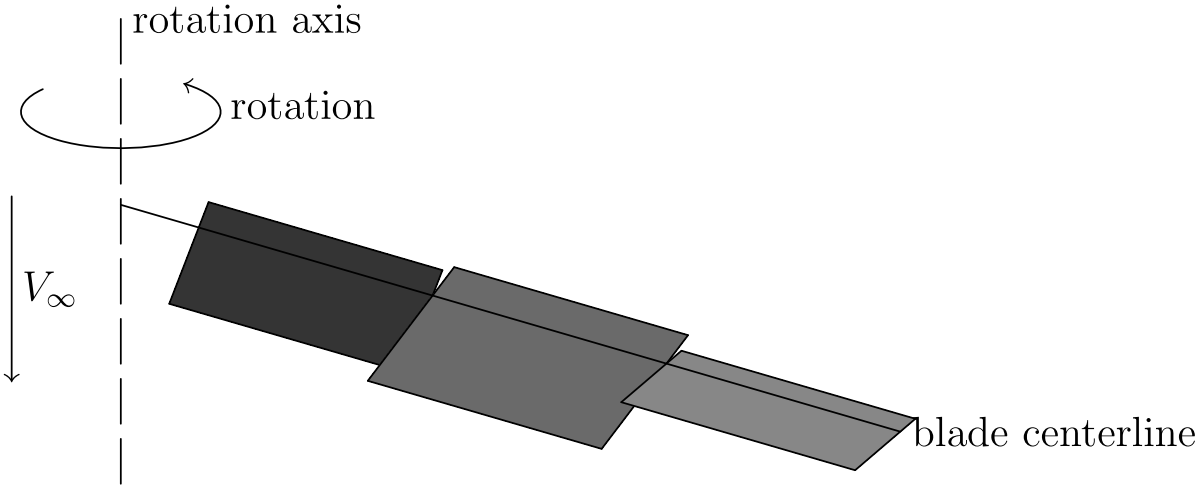


Figure 3.14: A schematic view of a three-segment model of a rotor blade. Note that each segment can have a different length and a different but constant $c$, $\beta$, and airfoil.

Table 3.5 shows the BEM results for the chosen stator, and the results are sobering. The BEM XFOIL calculated $C_l$ values are about 0.1 to 0.15 higher than the XROTOR values. This already should mean that the blade lift is substantially higher than the XROTOR blade lift, thus thrust and torque should be increased too. However, the XFOIL $C_d$ values are about twice as large as the XROTOR values; most likely a result of the airfoil polar scaling used by XROTOR which is inferior to the XFOIL airfoil analysis. Appendix B explains the polar scaling of XROTOR. A larger drag value for BEM means that the total thrust is less. This is not found from the data; the BEM thrust is more than twice as high as the XROTOR value. The thrust is mainly generated by the axial component of the lift vectors. See also Figure 1.3 as a reminder of the force vector geometry on a stator blade section. Because the velocity vector

Table 3.4: Data from a simple 3-segment BEM analysis of a F50 rotor blade. The tables contain respectively the general parameters, segment aerodynamic data, and the performance comparison with the XROTOR BEM model. The rotor was run at $J = 2.2516$.

| **Parameter** | **Value** | **Unit** |
|---|---|---|
| $r_{tip}$ | 1.8288 | $[m]$ |
| $r_{hub}$ | 0.30 | $[m]$ |
| $\rho$ | 0.54994 | $[kg/m^3]$ |
| $V_\infty$ | 140 | $[m/s]$ |
| $rpm$ | 1020 | $[rpm]$ |

| **Parameter** | **Value** | **Value** | **Value** | **Unit** |
|---|---|---|---|---|
| Radius | 29 | 50 | 70 | [%] |
| Radius | 0.5304 | 0.9144 | 1.2802 | $[m]$ |
| $c$ | 0.2785 | 0.2676 | 0.2799 | $[m]$ |
| $\beta$ | 68.67 | 57.84 | 48.59 | [°] |
| $V_a$ | 0.0 | 0.0 | 0.0 | $[m/s]$ |
| $V_t$ | 56.65 | 97.67 | 136.74 | $[m/s]$ |
| $V$ | 151.03 | 170.70 | 195.70 | $[m/s]$ |
| $\phi$ | 22.03 | 34.90 | 44.32 | [°] |
| $\alpha$ | 0.70 | 2.75 | 2.91 | [°] |
| Re | 1.51E6 | 1.64E6 | 1.97E6 | [−] |
| $C_l$ (`*.writ`) | 0.1660 | 0.4580 | 0.5740 | [−] |
| $C_d$ (`*.writ`) | 0.0087 | 0.0066 | 0.0050 | [−] |
| $dL$ | 168.72 | 359.17 | 1237.56 | $[N]$ |
| $dD$ | 8.84 | 5.18 | 10.78 | $[N]$ |
| $dT$ | 55.09 | 201.26 | 857.00 | $[N]$ |
| $dQ$ | 84.71 | 272.06 | 1143.02 | $[Nm]$ |

| **Parameter** | **Value** | **Unit** |
|---|---|---|
| Rotor thrust (simple BEM) | 6680.13 | $[N]$ |
| Rotor thrust (XROTOR) | 6960 | $[N]$ |
| % difference | -4.02 | [%] |
| Rotor torque (simple BEM) | 8998.71 | $[Nm]$ |
| Rotor torque (XROTOR) | 10500 | $[Nm]$ |
| % difference | -14.3 | [%] |

is almost fully aligned with the axial direction, $-5 < \chi < 5°$, the sine term of Equation 1.1 is very sensitive to small changes in $\chi$, whereas the cosine term is hardly affected. This is the suspected reason for the gross overestimation of stator thrust and the rather correct value of stator torque.

**Stator cropping effects**

Typical slipstream profiles such as shown in Figure 3.15 show that the system slipstream has significant finite values almost over the full radius, but that the net (summed) amount is much closer to 0 than that of the rotor slipstream. XROTOR sometimes seems to be unable to handle the low rotation and low power settings in combination with existing tangential slipstream components to design a MIL stator. The fact that the rotor slipstream has a significant finite tangential component at the stator tip (where circulation goes to zero), apparently makes the MIL routine design a stator tangential velocity distribution which does not minimize the tangential velocity at all radial locations. Instead, it seems to minimize the sum of tangential velocities: note that the negative and positive 'areas' under the tangential system curve with respect to the radial line are quite similar in size in Figure 3.15.

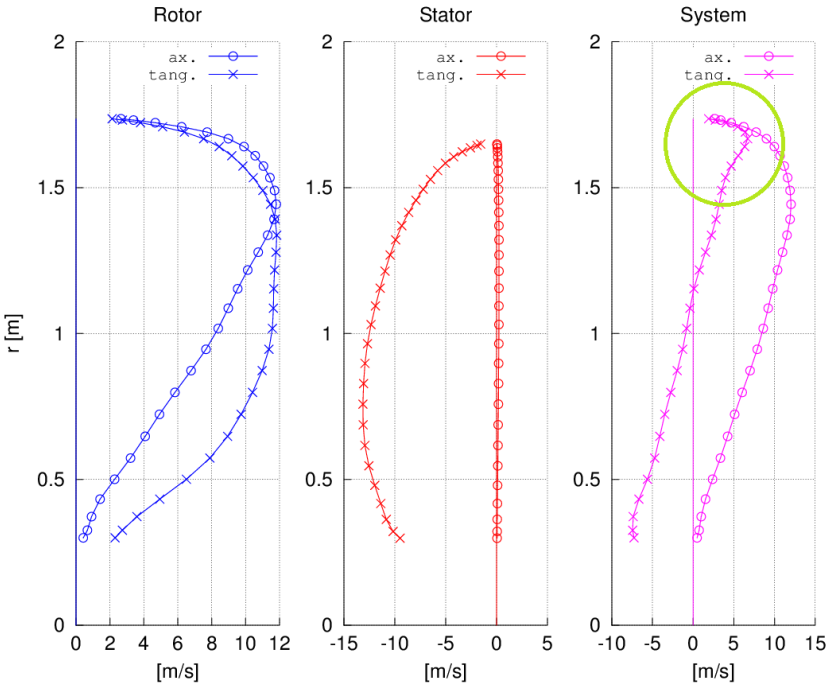


Figure 3.15: Example of rotor, stator, and system slipstream velocity distributions. The green circle indicates the nonzero swirl at the stator tip radius in the system slipstream because the differences in rotor and stator radii and associated circulation distributions.

**Design parameter influence in general**

A large variation in design parameters was used in numerous runs (not discussed here) such as lift coefficient, stator cropping, number of blades, and choice of airfoil. Consistent with the numerous runs for the APIAN rotor-stator combination described in the next section (Section 4.4) it was found that the increase in $\eta$ over the rotor-only case is affected in the following ways:

Table 3.5: Data from a simple 3-segment BEM analysis of a stator blade designed for the F50 stator. The tables contain respectively the general parameters, segment aerodynamic data, and the performance comparison with the XROTOR BEM model. The stator was designed for $C_L = 0.25$ at a rotor setting of $J = 2.2516$.

| **Parameter** | **Value** | **Unit** |
|---|---|---|
| $r_{tip}$ | 1.6505 | $[m]$ |
| $r_{hub}$ | 0.30 | $[m]$ |
| $\rho$ | 0.54994 | $[kg/m^3]$ |
| $V_\infty$ | 140 | $[m/s]$ |
| $rpm$ | 1.36 | $[rpm]$ |

| **Parameter** | **Value** | **Value** | **Value** | **Unit** |
|---|---|---|---|---|
| Radius | 29 | 50 | 70 | [%] |
| Radius | 0.4786 | 0.8253 | 1.1554 | $[m]$ |
| $c$ | 0.1110 | 0.1606 | 0.1963 | $[m]$ |
| $\beta$ | 92.78 | 92.63 | 92.53 | [°] |
| $V_a$ | 1.88 | 6.32 | 9.59 | $[m/s]$ |
| $V_t$ | 5.81 | 10.81 | 11.86 | $[m/s]$ |
| $V$ | 141.98 | 146.72 | 150.06 | $[m/s]$ |
| $\phi$ | 2.34 | 6.86 | 4.53 | [°] |
| $\alpha$ | 5.13 | 6.86 | 7.07 | [°] |
| Re | 0.57E6 | 0.85E6 | 1.06E6 | $[-]$ |
| $C_l$ (`*.writ`) | 0.4840 | 0.6340 | 0.6410 | $[-]$ |
| $C_l$ (XFOIL) | 0.5852 | 0.7530 | 0.7765 | $[-]$ |
| $C_d$ (`*.writ`) | 0.0054 | 0.0047 | 0.0043 | $[-]$ |
| $C_d$ (XFOIL) | 0.0105 | 0.0120 | 0.0113 | $[-]$ |
| $dL$ | 156.49 | 198.92 | 514.33 | $[N]$ |
| $dD$ | 1.75 | 1.47 | 3.45 | $[N]$ |
| $dT$ | 4.65 | 13.18 | 37.21 | $[N]$ |
| $dQ$ | 74.88 | 163.80 | 592.69 | $[Nm]$ |

| **Parameter** | **Value** | **Unit** |
|---|---|---|
| Stator thrust (simple BEM) | 330.28 | $[N]$ |
| Stator thrust (XROTOR) | 126 | $[N]$ |
| % difference | 162.13 | [%] |
| Stator torque (simple BEM) | 4988.23 | $[Nm]$ |
| Stator torque (XROTOR) | 4660 | $[Nm]$ |
| % difference | 7.04 | [%] |

- Less blades give less increase.
- A symmetrical airfoil performs marginally better than a cambered one.
- Airfoil thickness has almost negligible effect.
- Stator cropping is quite sensitive; larger cropping gives smaller increase.
- The choice of lift coefficient has a profound effect on the stator chord, but not always so much on $\eta$.

The program might not converge for all specified advance ratios. The 'wiggles' seen in the performance graphs such as Figure 4.4 in the next section, show that XROTOR is not fully comfortable with a rotor-stator case, where the stator analysis likely is the source of these data scatter. Theory gives no reason for those 'wiggles' to be there, and XROTOR's source codes gives no clue either. Machine accuracy might be of influence. The analyzed points that lie above the rest of the points in the performance graphs are the ones that likely are a bit too optimistic; this is what numerous runs with various input conditions show. A (parabolic) trendline through these points in the performance graph is, however, always consistent, and also consistent with literature. The largest performance gain can be found at the smallest advance ratio, and it smoothly curves down towards roughly −1% before XROTOR stops converging at these higher advance ratios. An example of a parameter sweep based on lift coefficient, stator blade number, and cropping can be found in Section 4.1.

**Conclusions**

A stator could remove a significant part of the rotor swirl, but in most cases will not be able to remove all swirl. An example is a case where the stator is cropped with respect to the rotor slipstream radius; not all of the slipstream is accessed by the stator in the first place. To analyse the sensitivity of a BEM analysis, the advanced BEM-code XROTOR was used and various stator designs for a Fokker F50 were generated and analyzed.

While XROTOR is certainly capable of designing MIL rotors, technically speaking it cannot design any stator, since it needs a non-zero *rpm* to prevent division-by-zero errors. However, by choosing a small enough *rpm*, the very slow rotating rotor can be assumed static for all practical reasons; it has then become a stator. These stator designs are plausible: the geometry is feasible and the slipstream data shows that they can indeed remove at least a part of the imparted rotor slipstream. In that sense, the XROTOR-designed stators do what they are designed for.

A simple BEM analysis for a designed rotor-stator cases showed that the XROTOR calculated rotor performance in terms of torque and thrust is reasonably well predicted by a crude 3-segment blade BEM. The comparison of simple BEM with XROTOR data gives an error below 15%. Applying the same BEM analysis to the stator did give rather similar results for torque, but grossly overestimates the stator thrust. Sensitivity of the analysis method to small-angle deviations from actual flow conditions in combination with stator blade angles near 90° are assumed to be the cause.

From the XROTOR slipstream data it is also clear that there is still quite some tangential velocity present in the system slipstream, and that it even can have both significant positive and negative values (i.e.: the system swirl rotation direction can be different at the root and the tip). Large variances in chord dimensions give small variations in overall propulsion efficiency gain, which has a value of about 1%. A literature study by the author [2] found that swirl recovery vanes or stators could have an efficiency gain up to about 4%. The little tangential slipstream data available most certainly does not show distributions with a linear behaviour such as shown in Figure 3.13. The XROTOR-based calculated efficiency gains are certainly plausible, but are on the small side. The simple BEM analysis of the stator shows a thrust value more than two times as high as the XROTOR calculated value. This is a significant difference, as the $\Delta\eta$ would be well over 2% for the simple BEM analysis, which is much closer to the values found in literature.

A valid question is of course which of the BEM methods is the more accurate one. XROTOR's routine is far more accurate than the simple BEM approach, and it is known to work well for designing and analyzing rotors. The lack of proper validation data (performance and especially geometry data of rotors and stators) available makes it very difficult to perform a proper comparison or validation. Regarding stator performance, XROTOR seems to underpredict performance a bit compared to literature values. The $\Delta\eta$ versus $J$ graph often shows some 'wiggly' behaviour, but the trend is always very clear. Although the MIL routine in XROTOR has some mathematical issues, the theory behind it is sound and should pose no problems. It was therefore decided to continue with XROTOR for both rotor analysis and stator design and analysis during this research project.

# 4

# STATOR DESIGN FOR A FOKKER F50 ROTOR AND THE APIAN-INF WIND TUNNEL TEST

## 4.1. STATOR DESIGN AND ANALYSIS FOR FOKKER F50

The modeling of the Fokker F50 rotor is already described in Section 3.2. Continuing using XROTOR for the stator design and analysis of the rotor-stator system, stators are designed for two operating conditions: take-off (TO) and cruise. Four analysis cases are defined:

- Case 1: Rotor at cruise, with stator designed for cruise.
- Case 2: Rotor at TO, with stator designed for TO.
- Case 3: Rotor at TO, with stator designed for cruise.
- Case 4: Rotor at cruise, with stator designed for TO.

Note that these cases refer to the rotor-stator combination only. The slipstream-wing interaction analysis can be found in Chapter 5.3.

The first two cases are straightforward; each case handles a certain flight regime. For the overall aircraft performance it is also wise to know the performance of the rotor-stator combination at off-design conditions, thus the third and fourth cases. The third case in particular is of interest: an aircraft that spends most of its time in cruise should not have a stator that severely reduces fuel efficiency during take-off and thereby possibly negating the overall efficiency gain.

**Case 1: Rotor at cruise, with stator designed for cruise**

This case uses the F50 rotor at cruise conditions such as found in Table 3.1. Manually varying input parameters gives a good stator design for the following stator design parameters, see Table 4.1. A stator blade has approximately the chord as a F50 rotor blade, but with a smaller radius, see Figure 4.1. As can be seen in the top view in Figure 4.2, there is little twist in the stator blade chords. A blade number of 5 is chosen to reduce noise

compared with 6 blades due to aerodynamic interference. More blades would likely increase performance slightly, but are also more heavy. For a hypothetical retrofit solution, less blades and less weight would be preferable, as the existing structure is not designed to handle these extra weights and loads. The blade shape has a very unwelcome feature, and that is that the chord gets rather small near the blade root, where structural loads are the highest. Manually editing the chord and blade angles to create a larger chord without changing the local circulation is possible, but negates the idea of using XROTOR to design a feasible stator. From an aerodynamic point of view, the planform seems very feasible, certainly when considering that the largest swirl is found on the outer section of the blade, and the chord distribution nicely mimicks this.

The rotor-stator system performance graph can be found in Figure 4.3. Although there is no absolute increase in propulsion efficiency, across a large range of advance ratios there is a performance gain of a few %. The stator is designed for a rotor operating at the design $J = 2.2516$.

The lines for $C_T$, $C_P$, $C_Q$ for $J < 1.8$ show a plateau-like behavior which was at first not expected, since the stator performance does not see a similar flattening. It should be realized that at such low advance ratios (high *rpm*) the local angle of attack on the blade becomes so large that stall occurs. Since stall, especially in it's early phase, affects drag much more than lift, it is the extra drag that decreases thrust and torque. The increase in lift still dominates the rotor slipstream, which is the reason why the flattening of the curves is not seen in the $\Delta\eta$ of the rotor-stator system. In addition to the rotor stall, it is not ruled out that for extreme large or small advance ratios away from the design advance ratio (partial) stall occurs on the stator blades too. Again, the lift component is hardly affected in the early stages of stall, which means that the stator still removes a significant amount of the swirl. Judging from Figure 4.4, stator stall seems not to occur because there is no flattening of the graphs at either low or high $J$. The increase of $\Delta\eta$ with diminishing $J$ becomes smaller, thus a drag increase of the stator negating the rotor thrust becomes more apparent at lower $J$ values. The $\Delta\eta$ of about 3% at low $J$ is similar to values found in literature. The increased local $\alpha$ at low $J$ creates a significant thrust increase leading to these $\Delta\eta$ values. However, the system is then operating at a significant lower $J$ than the value for which the stator was designed.

At the advance ratio of $J = 2.2516$, the calculated propulsion efficiency increase is just under $\Delta\eta = 1.0\%$. A performance increase could be expected when changing the cropping ratio towards $r/R = 1$, since more rotor swirl can be influenced. As the aircraft should also perform at high angles of attack and turbulence, a rather low value of $r/R = 0.90$ is used to prevent the chance of rotor tip vortices interacting with the stator.

A lift vector on a stator blade is pointing almost completely in tangential direction; its axial force component is much smaller than its tangential component. Figure 1.3 and Equations 1.1 and 1.2 show this: with a reasonably small swirl $\chi$, the resultant vector $R$ is practically equal to the tangential force generated. The stator therefore generates a large torque, which has to be carried by the support structure on which the stator is mounted. For this Case 1, the stator torque $Q = 5050[Nm]$, which is 48% of the rotor torque. Note that the rotor torque is not felt by the support structure: it is balanced against the power input of the rotor.

Table 4.1: Table containing design parameters of the F50 stator for analysis case 1.

| **Parameter** | **Value** | **Unit** |
|---|---|---|
| $C_L$ | 0.25 | [−] |
| Airfoil (NACA) | 0009 | [−] |
| $V_\infty$ | 140 | $[m/s]$ |
| $B$ | 5 | [−] |
| Rotor $J_{design}$ | 2.2516 | [−] |
| Stator cropping | 0.90 | $[r/R]$ |
| Power ratio | 750 | [−] |
| *rpm* ratio, design | 1000 | [−] |
| *rpm* ratio, analysis | 1000 | [−] |

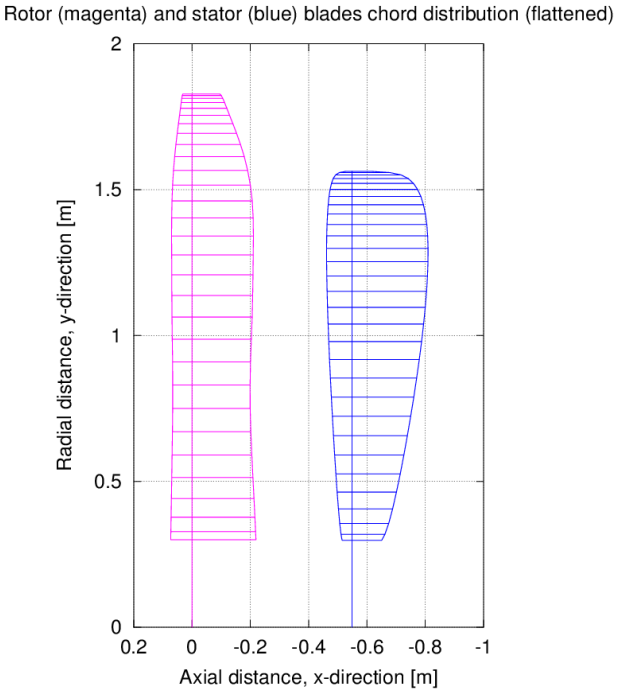


Figure 4.1: F50 rotor (magenta) and stator (blue) plan-forms; Case 1. These are not side views, but untwisted views of the blade chord distributions.

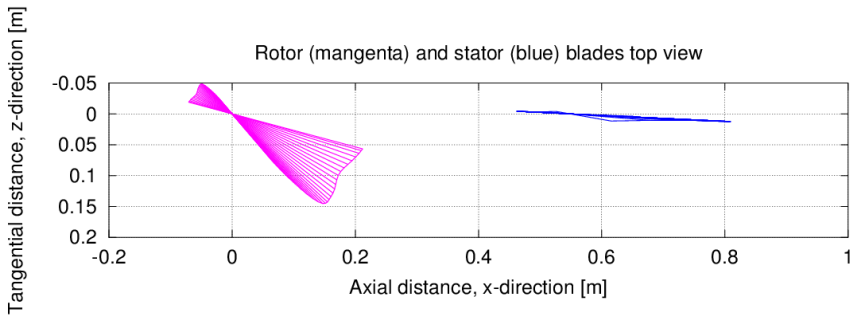


Figure 4.2: F50 rotor (magenta) and stator (blue) chords, top view; Case 1. It is the top view of the blades shown in Figure 4.1, effectively showing the blade angle $\beta$.

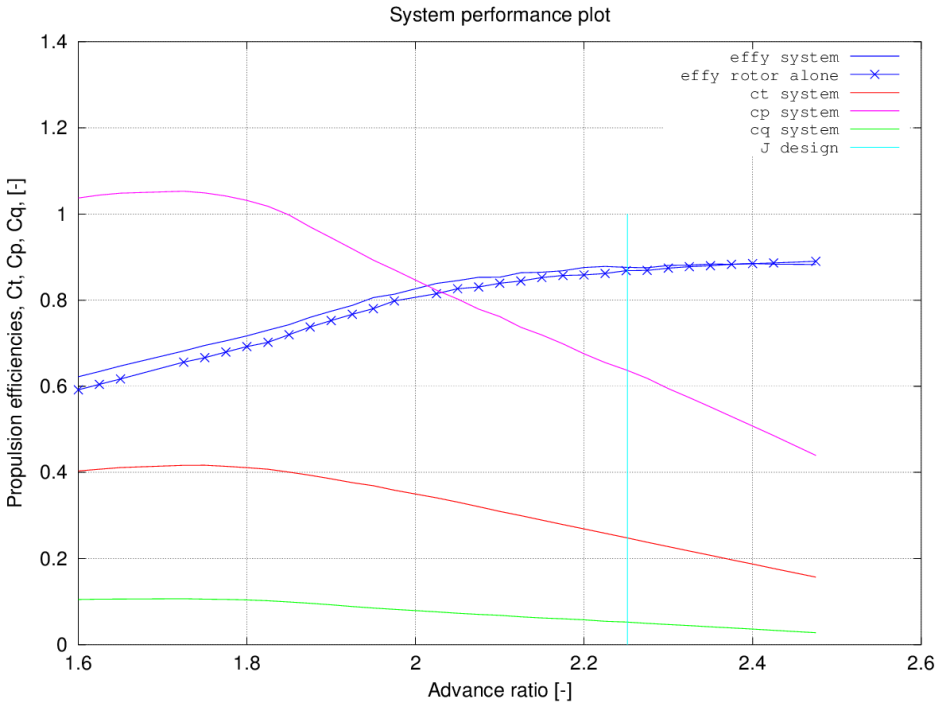


Figure 4.3: F50 rotor-stator system performance graph; Case 1. The cyan vertical line shows the rotor $J$ for which the stator was designed.

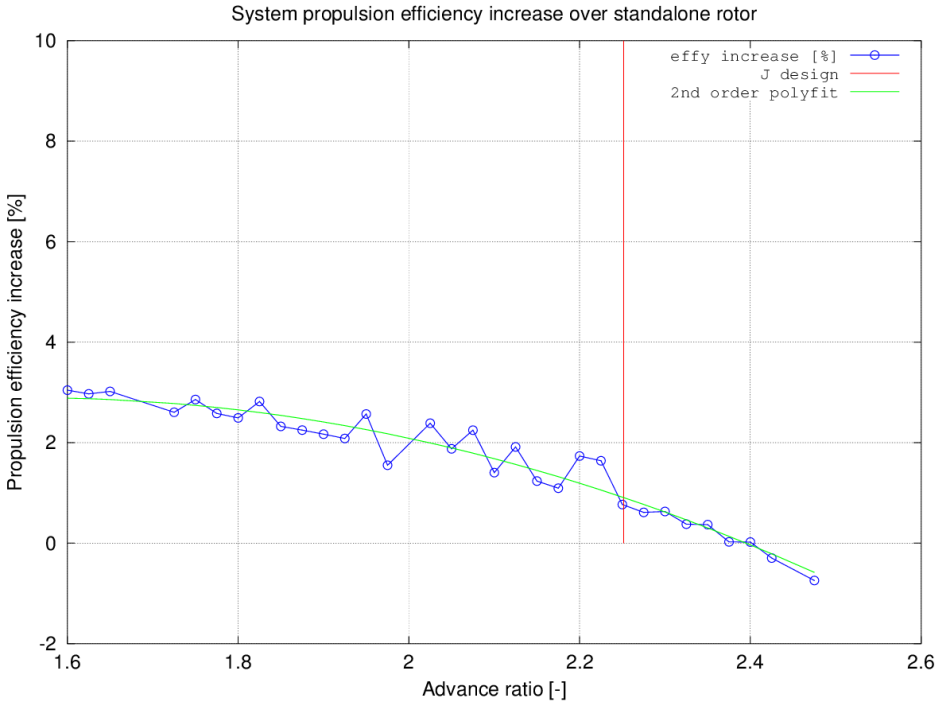


Figure 4.4: F50 rotor-stator system propulsion efficiency increase over rotor standalone; Case 1. Note the upward 'wiggles' (see text).

**Case 2: Rotor at TO, with stator designed for TO**

For this case, a stator is designed for the F50 rotor in take-off conditions (see Table 3.1.) A cropping ratio of $r/R = 0.90$ was chosen to allow for excessive angles of attack during take-off, such that the rotor tip vortices have less chance of hitting the stator blades. There is again an increase in propulsion efficiency to be found, the changes are even slightly larger than found in Case 1, now slightly above 1%. See Figure 4.5. Again 'wiggles' can be seen in the graph, such that it seems that any performance increase is small due to inaccuracies in XROTOR analysis. The trend line, a second order polynomial, seems more reliable. XROTOR does not want to converge for much of the advance ratios below $J = 0.90$, indicating that (rotor) stall issues are encountered.

At first hand there seems nothing wrong with these results. However, the stator blade plan-form, seen in Figure 4.6, has an enormous chord to radius ratio, and an even small root chord compared with Case 1. When thinking of retro-fitting aircraft with such a stator, it is clear that such a stator design has a significant impact on geometry and weight distribution of the propulsion system. It is almost certain that the root geometry of the blade needs to be altered to cope with the structural loads. Also note that the spacing versus the chord dimension is now quite small, implying that the rotor works in significant up-wash of the stator blades. Since XROTOR uses circumferentially averaged slipstream velocities to model the influence of rotor and stator on each other, such a large stator mounted this close to a rotor would probably give erroneous results when modeled with XROTOR blade element method. Such geometry is also likely to introduce aeroacoustic noise resulting from the rotor encountering large stator up-wash when blades pass each other.

More runs of the program with various airfoils such as the NACA 2412 and 4412, different constant $C_L$ values and various number of blades all result in either non-converged solutions or excessively large stator blades as described above. Table 4.2 and Figure 4.6 suggest that a higher $C_L$ results in a more feasible blade planform with smaller chord, but nonconvergence is often a result, meaning that somewhere along the blade XROTOR encounters a circulation distribution such that the MIL condition cannot mathematically be met. In most cases the twist throughout the blade is near an unrealistic 90°, hinting that XROTOR is very near its limits in handling the slipstream velocities. The conclusion is therefore that a stator designed for take-off conditions for the F50 rotor is plausible but not very realistic. Table 4.2 lists the design parameters of the take-off stator.

Torque of this stator is larger than Case 1: $Q = 8580[Nm]$. It is equal to 55% of the rotor torque, but since rotor torque is not felt by the support structure, the stator torque is the defining torque which should be carried by the support structure. The large increase in torque versus Case 1 seems to be rather proportional to the large increase in blade area, but effects of different operating conditions should not be left out, such as the dynamic pressure.

Table 4.2: Table containing design parameters of the F50 stator for analysis case 2.

| **Parameter** | **Value** | **Unit** |
|---|---|---|
| $C_L$ | 0.25 | [−] |
| Airfoil (NACA) | 0009 | [−] |
| $V_\infty$ | 62 | $[m/s]$ |
| $B$ | 5 | [−] |
| Rotor $J_{design}$ | 0.9971 | [−] |
| Stator cropping | 0.90 | $[r/R]$ |
| Power ratio | 1000 | [−] |
| *rpm* ratio, design | 1000 | [−] |
| *rpm* ratio, analysis | 1000 | [−] |

**Case 3: Rotor at TO, with stator designed for cruise**

For this case, the stator designed for Case 1 is run with the F50 rotor in take-off conditions (see Table 3.1.) There is still an increase in propulsion efficiency to be found, but the change is again rather small, about 0 to 1%. In contrast to Case 1, the performance increase is hardly larger at lower $J$. See Figure 4.7. Again 'wiggles' can be seen in the graph, such that it seems that any performance increase is small or negligible due to inaccuracies in XROTOR analysis. However, it is clear that the stator designed for cruise conditions is not at all hurting the system performance at take-off conditions. For the sake of completeness the system performance graph is given in Figure 4.8, which shows that the total system efficiency is still above 70% which seems very plausible on take-off.

The stator torque is lower than Case1, despite the higher dynamic pressure at sealevel compared to high altitude cruise flight: $Q = 2520[Nm]$, 16% of the rotor torque. This means that the cruise stator torque of Case 1 is the limiting torque case for this stator design.

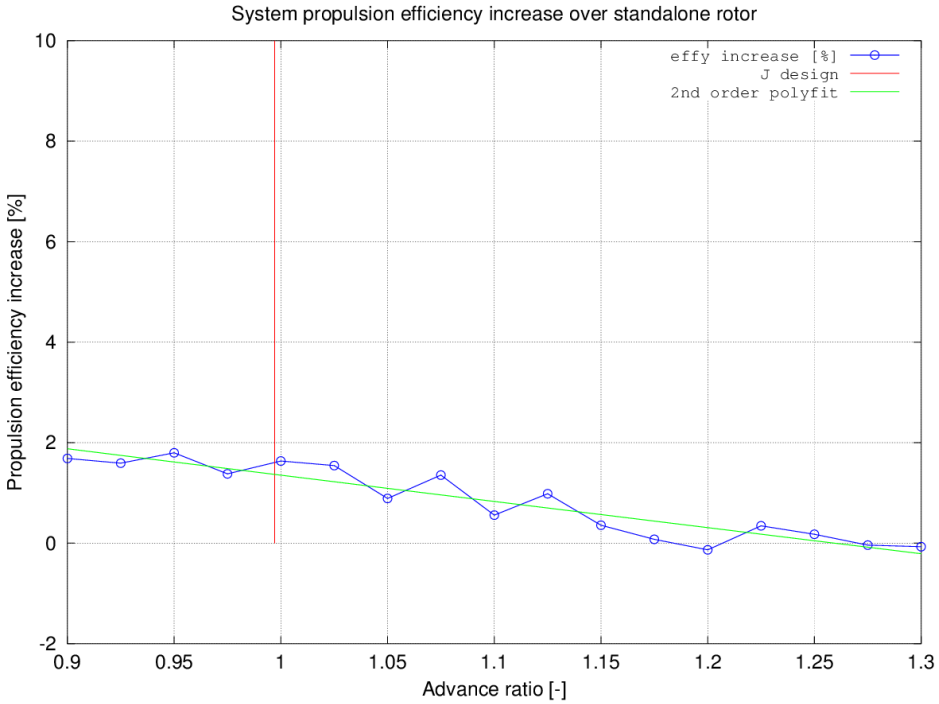


Figure 4.5: F50 rotor-stator system propulsion efficiency increase over rotor standalone; Case 2.

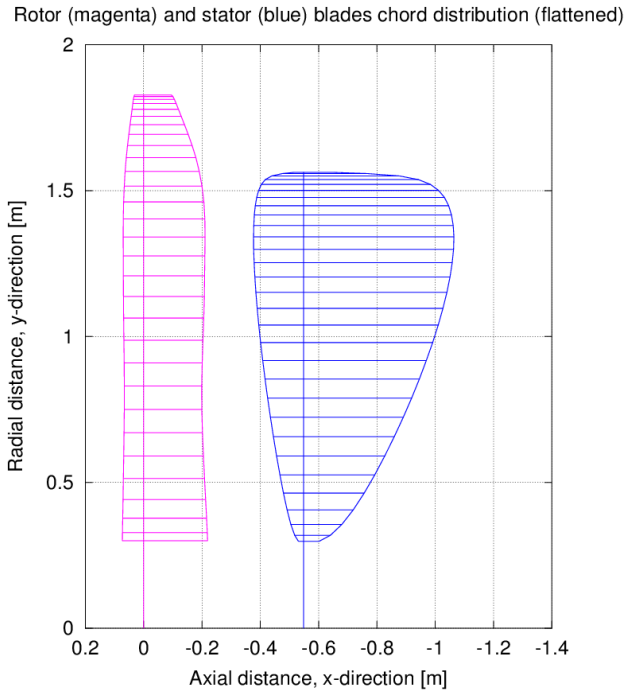


Figure 4.6: F50 rotor-stator planform; Case 2.

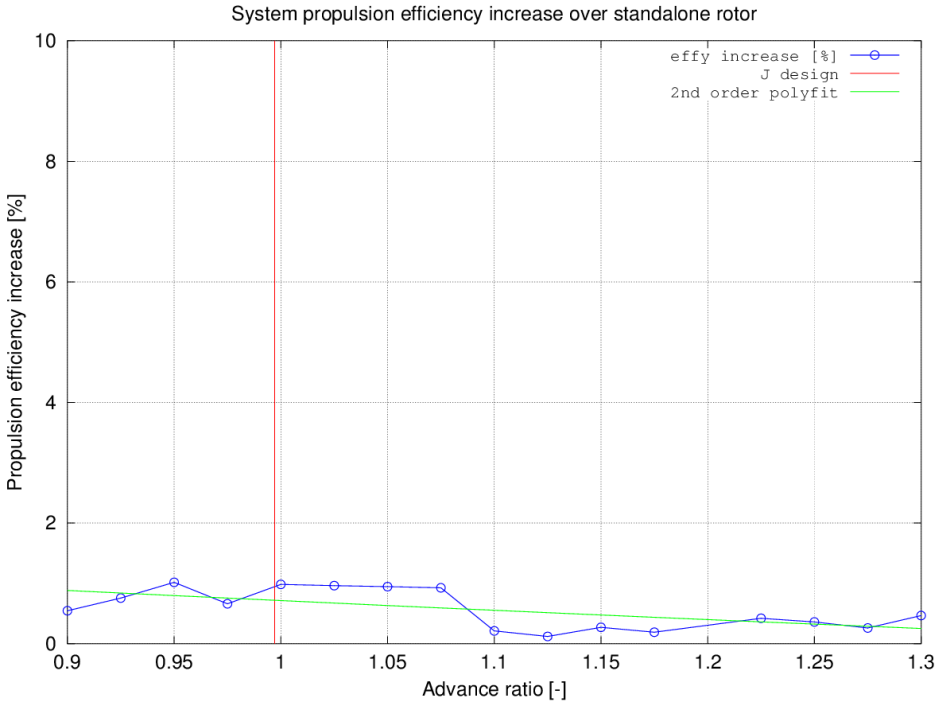


Figure 4.7: F50 rotor-stator system propulsion efficiency increase over rotor standalone; Case 3.

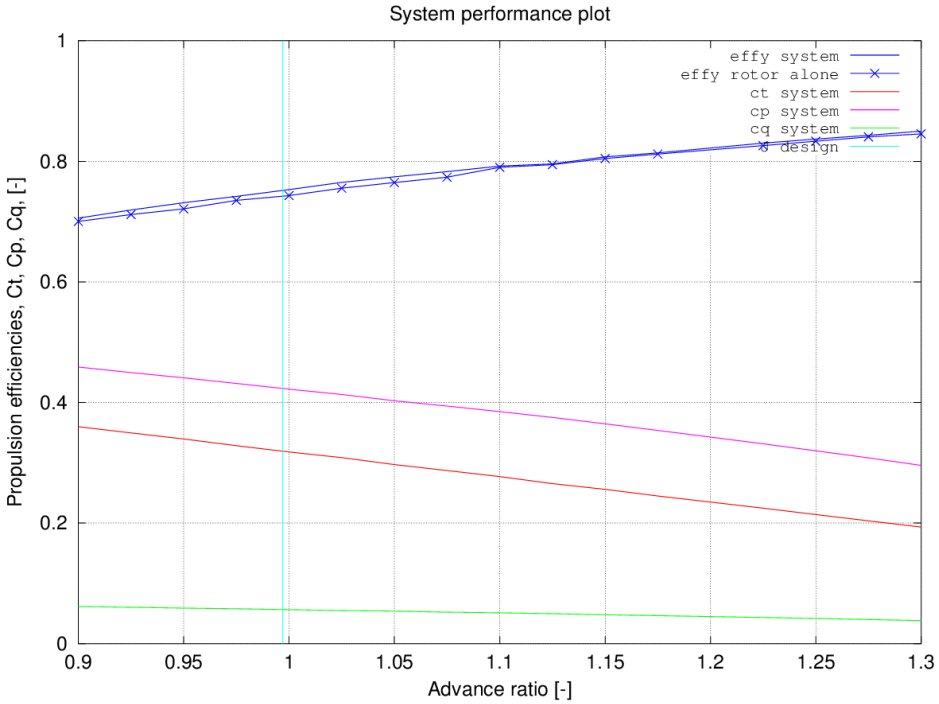


Figure 4.8: F50 rotor-stator system performance graph; Case 3.

**Case 4: Rotor at cruise, with stator designed for TO**

Considering the outcome of Case 2, in particular the blade planform, there is little incentive to model the behavior of such an unfeasibly large stator in cruise conditions. A stator designed for take-off conditions which removes only part of the slipstream could be more realistic, but since it does not attempt to remove all of the tangential slipstream component, it would likely also perform less at cruise conditions. The XROTOR-designed blade planform is deemed unacceptably large and unrealistic.

**Parameter sweep**

Considering the stator geometry and the performance in Cases 1 and 3, it seems that the stator designed for cruise performs well in both cruise and take-off conditions. A parameter sweep is done to see the effects of the following parameters on propulsion efficiency in cruise conditions.

- Number of blades.
- Lift coefficient.
- Stator cropping.

The results for cruise condition can be found in Table 4.3. What is immediately clear from the data is that the change in efficiency is rather small, in the order of 0 to 1%, for all the parameters. As expected, an increase in the number of blades raises the efficiency gain. Since XROTOR does not take into account any tip vortex interaction, it is also fully according to expectations that a larger stator radius (until equal to rotor radius) increases the efficiency gain. The effect of cropping ratio shows the same behaviour as the number of blade variation. The behavior of the overall constant lift coefficient $C_L$ is somewhat less pronounced. Any changes in efficiency are even smaller than for the other parameters considered, but the trend is clear: a higher $C_L$ gives a higher efficiency increase (in this particular case, $C_L > 0.50$ causes nonconvergence issues). The found efficiency values are still some % below literature data, and it is possible that decreasing chord dimensions for higher lift coefficients might have a negative effect on the stator drag due to decreased Reynolds number, thus limiting performance increase. Figures 4.9, 4.10, 4.11 show the system efficiency increase of all three parameter cases in graphical form.

**Conclusions and recommendations of the F50 stator analysis**

Considering the stator geometry and the performance in Cases 1 and 3, it seems that the stator designed for cruise performs well in both cruise and take-off conditions. A propulsion efficiency increase of 0.8% can be expected in cruise conditions, which might even increase a little bit (up to 1.0%) during take-off. The geometry is certainly feasible from an aerodynamic point of view, although it is expected that geometry changes near the root are necessary for structural reasons. Case 2 shows a stator design, which however aerodynamically feasible, is of such geometry that it is deemed unrealistic. These stator blades look like 'paddles', and it hints that XROTOR's MIL routine is very near its limits of designing a feasible stator. For the same reason Case 4 is not analyzed, as such a stator would be unrealistic.

Table 4.3: Table containing parameter sweep data for the rotor-stator system from Case 1. Values in bold face indicate the stator design parameters used for the stator of Cases 1 and 3. Changes in performance are given as comparison with either rotor standalone or designed stator and are rather small, in the range of 0 to 1%. Performance does not say anything about the geometric feasibility of the stator blades.

| **Parameter** | **Case A** | **Case B** | **Case C** | **Case D** | **Unit** |
|---|---|---|---|---|---|
| Number of blades | 4 | **5** | 6 | 7 | [−] |
| $\Delta\eta$ rotor standalone | 0.240 | **0.762** | 1.012 | 1.058 | [%] |
| $\Delta\eta$ designed stator | -0.522 | **0** | 0.250 | 0.296 | [%] |

| **Parameter** | **Case E** | **Case B** | **Case F** | **Case G** | **Unit** |
|---|---|---|---|---|---|
| Cropping ratio | 0.85 | **0.90** | 0.95 | 1.00 | [$r/R$] |
| $\Delta\eta$ rotor standalone | -0.077 | **0.762** | 1.135 | 1.326 | [%] |
| $\Delta\eta$ designed stator | -0.839 | **0** | 0.373 | 0.564 | [%] |

| **Parameter** | **Case H** | **Case B** | **Case I** | **Case J** | **Case K** | **Case L** | **Case M** | **Unit** |
|---|---|---|---|---|---|---|---|---|
| $C_L$ | 0.20 | **0.25** | 0.30 | 0.35 | 0.40 | 0.45 | 0.50 | [−] |
| $\Delta\eta$ rotor standalone | 0.562 | **0.762** | 0.896 | 0.985 | 1.049 | 1.089 | 1.127 | [%] |
| $\Delta\eta$ designed stator | -0.200 | **0** | 0.134 | 0.223 | 0.287 | 0.327 | 0.365 | [%] |

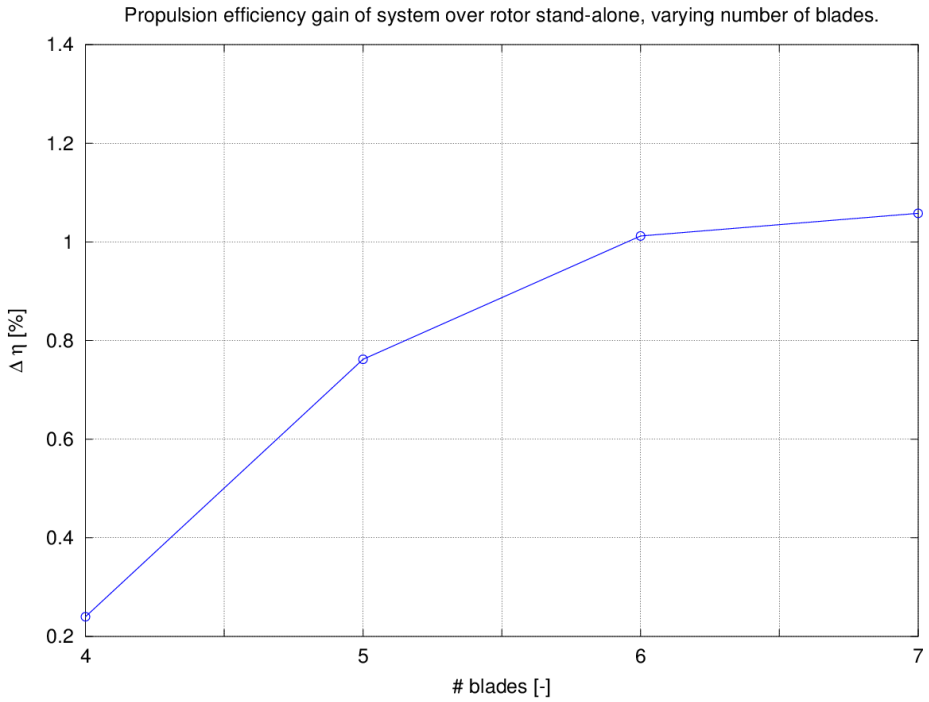


Figure 4.9: The effect of the number of stator blades on the system efficiency increase. Each point indicates a new stator design.

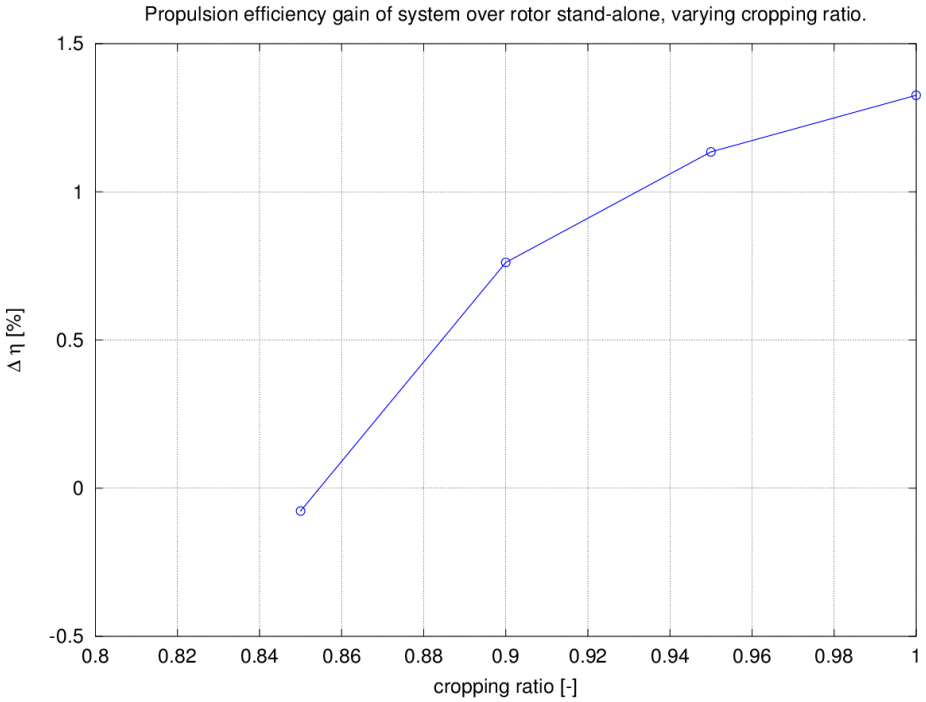


Figure 4.10: The effect of the stator cropping ratio on the system efficiency increase. Each point indicates a new stator design.

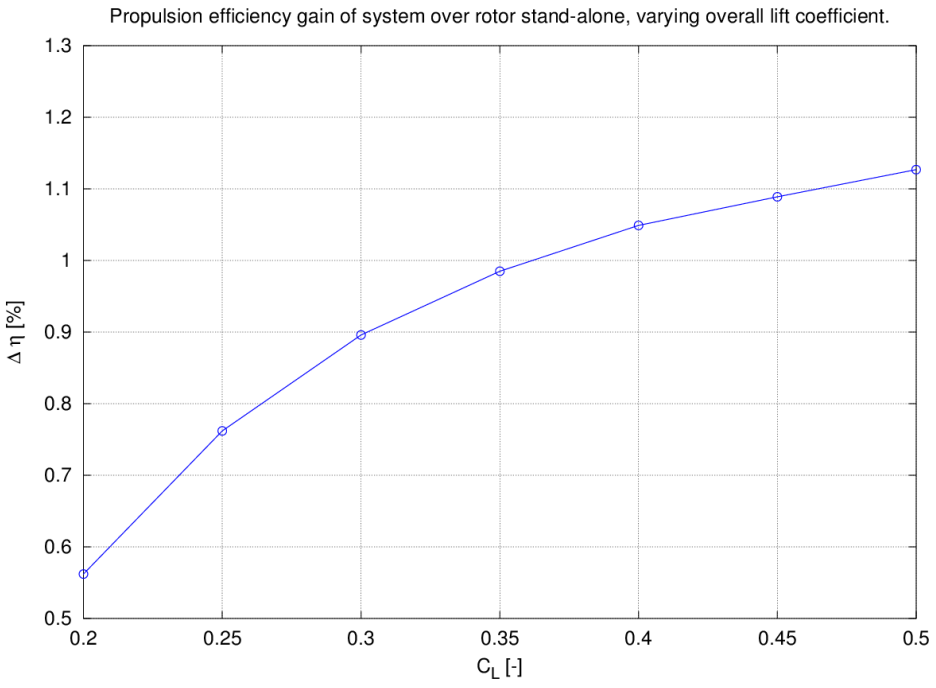


Figure 4.11: The effect of the overall stator blade $C_L$ on the system efficiency increase. Each point indicates a new stator design.

A parameter study showed that changing a number of stator design parameters has some but little effect on the increase in propulsion efficiency of the system over a rotor standalone. More blades mean better efficiency, and the less cropping is used on the stator radius, the better the efficiency gets. in both cases the gain is less than 1%. A change in design $C_L$ seems to have an optimum $C_L$ where the efficiency gain is the largest, but this gain is below 0.5%. Since XROTOR has some difficulties in designing stators, and for each analyzed point in the parameter study the stator is different, it is hard to tell if the change in $\Delta\eta$ is fully due to parameter changes. But the overall trend is valid. The torque generated by the stator is quite substantial, and for the Fokker F50, the cruise stator design of Case 1 and Case 3 generates the most torque at cruise conditions.

Detailed CFD analysis or wind tunnel testing could show if the expected gain is really there, or the amount of efficiency gain actually found. An increase of even 1% could be interesting for new aircraft designs or retrofitting existing aircraft, since it is likely that the fuel save by better performance is larger than the fuel increase from installing stator blades.

## 4.2. APIAN-INF WIND TUNNEL VALIDATION OF STATOR PERFORMANCE

As a validation of the rotor-stator analysis program a wind tunnel test was conducted using the APIAN propeller. APIAN is an European project between industry and universities to investigate the performance of a six-bladed transonic propeller at a wide range of operating conditions, such as angle of attack and *rpm* at various velocities from $M = 0.2$ to $M = 0.7$. It was possible to use one day of the wind tunnel test program APIAN-INF ('APIAN In Non-uniform Flow') during 15 to 30 September 2014 at DNW in Marknesse, the Netherlands. The APIAN-INF test involved partners such as Airbus, DLR, DNW, INCAS Budapest, TsAGI, and several universities such as Braunschweig, Cambridge and Delft, and used the Large Low-speed Facility (LLF), which is discussed below. A picture of the APIAN-INF test setup can be seen in Figure 4.12. Modeling the rotor is described in the next section, Section 4.3, and the stator design for this test is described in Section 4.4.

**Stator test programme**

A stator was designed for the APIAN rotor, modeled by an early version of the author's rotor-stator code. Because the stator test was an extra test added later to the test program, the stator mounting was not optimal. It was mounted behind the APIAN rotor on the support boom, which housed the drive-train for the rotor. This meant that the stator hub radius was substantially larger than the APIAN hub radius, which could be cause for substantial radial flow which cannot be modeled with standard BEM. The mounting also prevented the use of rotating balance to measure the stator thrust and torque directly. Although the rotor did have a rotating shaft balance, direct system thrust calculation by adding rotor and stator thrust was therefore not possible. A wake rake was not available and would have proven cumbersome because of various reasons. A second support boom which would support a wing in front of the APIAN rotor for other APIAN-INF tests could have restricted access for a wake rake system. A more important reason to decide against a wake rake is the fact that the stator slipstream is almost stationary downstream: time-averaging at a certain point in the slipstream would not yield a circumferentially averaged velocity profile such as would

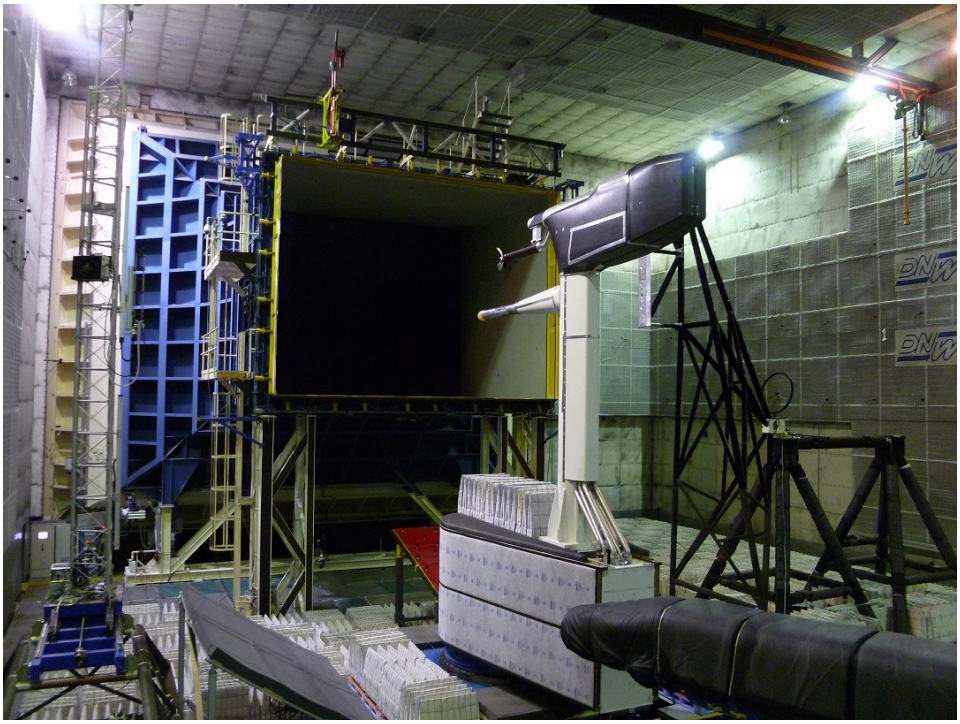

Figure 4.12: The APIAN-INF test setup in the LLF. The rotor and stator are located on the very end of the uppermost horizontal boom, attached to a support structure housing the drivetrain and measurement systems. The PIV tower is the metal lattice tower seen on the very left side of the picture, and the black lattice tower is a traversing microphone array for acoustic measurements. Photo by author.

be the case in a rotor slipstream.

A PIV measurement tower installed to measure slipstream velocities around the rotor was also used to measure the slipstream around the stator. Given the PIV laser and camera geometry, which was again not optimal, 11 longitudinal planes could be measured, equally spaced between two successive stator blades, where plane 1 and 11 are located directly behind a stator blade.

The complete setup was tested at rotor advance ratios ranging from $J = 1.05$ to 1.75 at a pitch angles between of $\alpha = -6$ and 6°. Various microphone arrays were installed at various locations in the wind tunnel to asses the aeroacoustics of the rotor-stator combination. For the stator thrust performance only the $\alpha = 0°$ case was of interest as the analysis methods used cannot handle asymmetric flow conditions.

Because the stator test was added quite late to the test program, PIV results were not yet fully available at the time of writing, so unfortunately there is yet no conclusion on the APIAN stator performance. Preliminary PIV results do show that the rotor slipstream radius is practically constant, for both the isolated rotor and the rotor-stator system, as shown in Figure 4.13. This is consistent with the slipstream shape mentioned in Section 2.1.

**DNW Large Low-speed Facility**

The LLF [29] is closed-circuit atmospheric wind tunnel with continuous flow. It can have an open jet configuration such as used for the APIAN-INF tests, or a closed test section can be used. For the open jet case, the jet has dimensions of 8 by $6m$ (width by height), and the velocity can range from 0 to $80m/s$. A aerial photo of the LLF complex is shown in

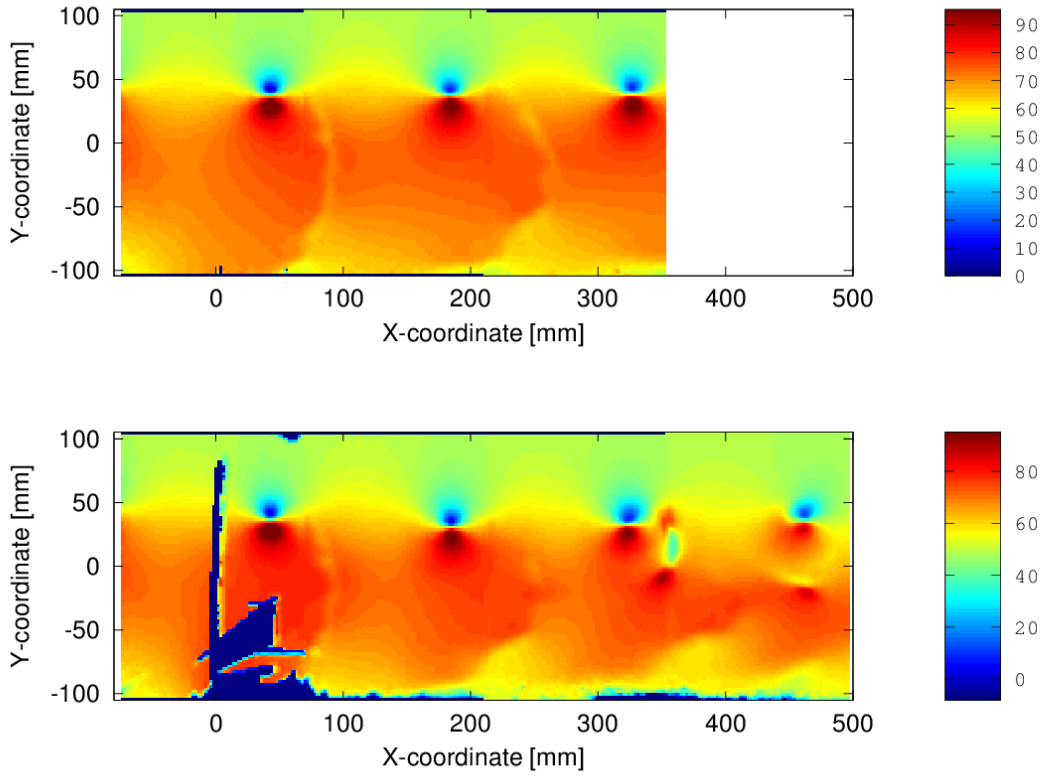


Figure 4.13: Two PIV images from the APIAN-INF test programme, one of the isolated propeller (top) and one of the propeller with stator behind it (bottom). The images both show the axial velocity in a plane spanned by the axial and radial directions. It is clear that the radius of the tip vortex centers, depicted by the red-blue 'pinches', is very constant. The lower picture shows an irregular shaped dark area; the stator LE is located around $x = 0$ and some reflections are masked leading to this area. At the time of writing the post-processing was not fully complete, so the graph axes reference locations are not yet correct but the scale is. The color bars indicate axial velocity in $m/s$. Images created by T. Sinnige.

Figure 4.14, and an impression of the empty test section in open jet configuration is shown in Figure 4.15. The massive fan is shown in Figure 4.16.

Figure 4.14: An overview of the LLF complex, with the test section drawn on top of the aerial photograph. Taken from DNW website [29].

Figure 4.15: The open jet test section of the LLF wind tunnel. Taken from DNW website [29].

Figure 4.16: The fan of the LLF wind tunnel. Note the person standing at the bottom of the fan for scale. Taken from DNW website [29].

## 4.3. THE APIAN ROTOR

A description is given how the APIAN rotor geometry data was extracted from a 3D CAD file, and how this data was used to recreate the APIAN rotor in XROTOR. The XROTOR model is validated against 5 wind tunnel PIV cases, with good matching results. A discussion about the slipstream shape and velocities concludes this chapter.

**Rotor geometry**

The APIAN propeller has 6 blades with nonlinear sweep. The chord is rather wide, making it a turbofan propeller rather than resembling the 'ideal' actuator disk. The NLR via DNW and the TU Delft Aerospace faculty has provided the propeller geometry as a 3D CAD file (CATIA, `*.igs`, and `*.stp` files). For an overview of one propeller blade with spinner, see Figure 4.17. The filenames all start with 'Pr5680-Spinner and Blade'.

**APIAN rotor model for XROTOR**

To create input for XROTOR, one propeller blade needs to be sliced at various radial positions in chordwise sections to obtain the local radius ratio $r/R$, local chord ratio $c/R$ and local blade angle $\beta$. Using the CATIA 3D CAD software, drawings were made of each cross-section. See Figure 4.18 for the radial locations of the sections and Figure 4.19 shows an example of measurements of one cross-section. The radial positions started from $r = 65mm$ with intervals of $5mm$ near the root and tip and a more coarse interval of $10mm$ in between. The reason for the smaller interval at the root and tip is to have a more accurate geometry definition where the changes in the blade angle and/or chord dimensions are the largest. XROTOR will create its own radial distribution based on this input, which again has a smaller interval near the root and the tip.

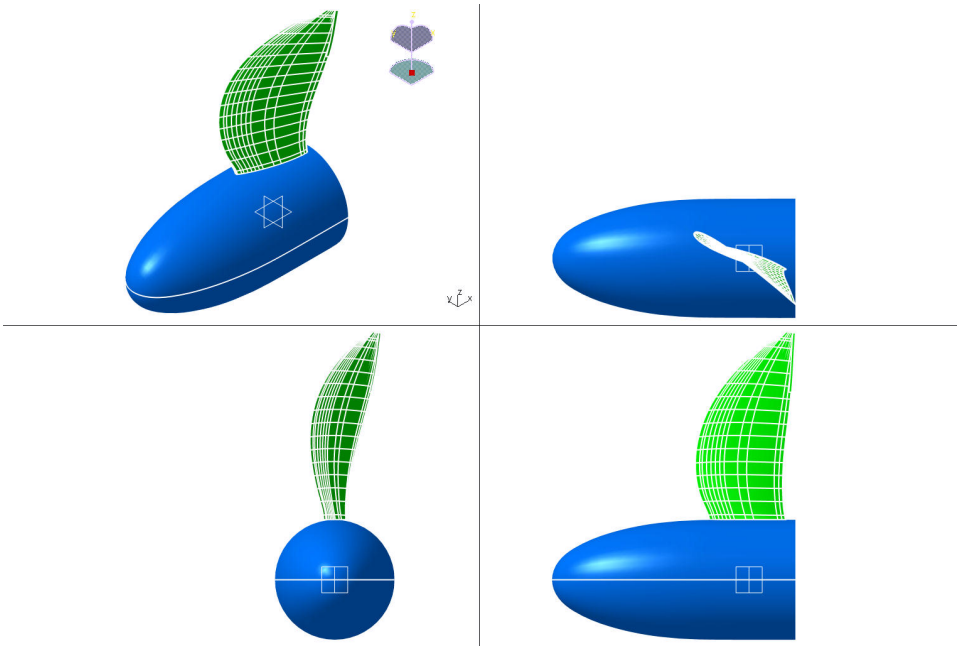

Figure 4.17: 3D view and 3-view of CATIA CAD model of APIAN propellerblade with hub.

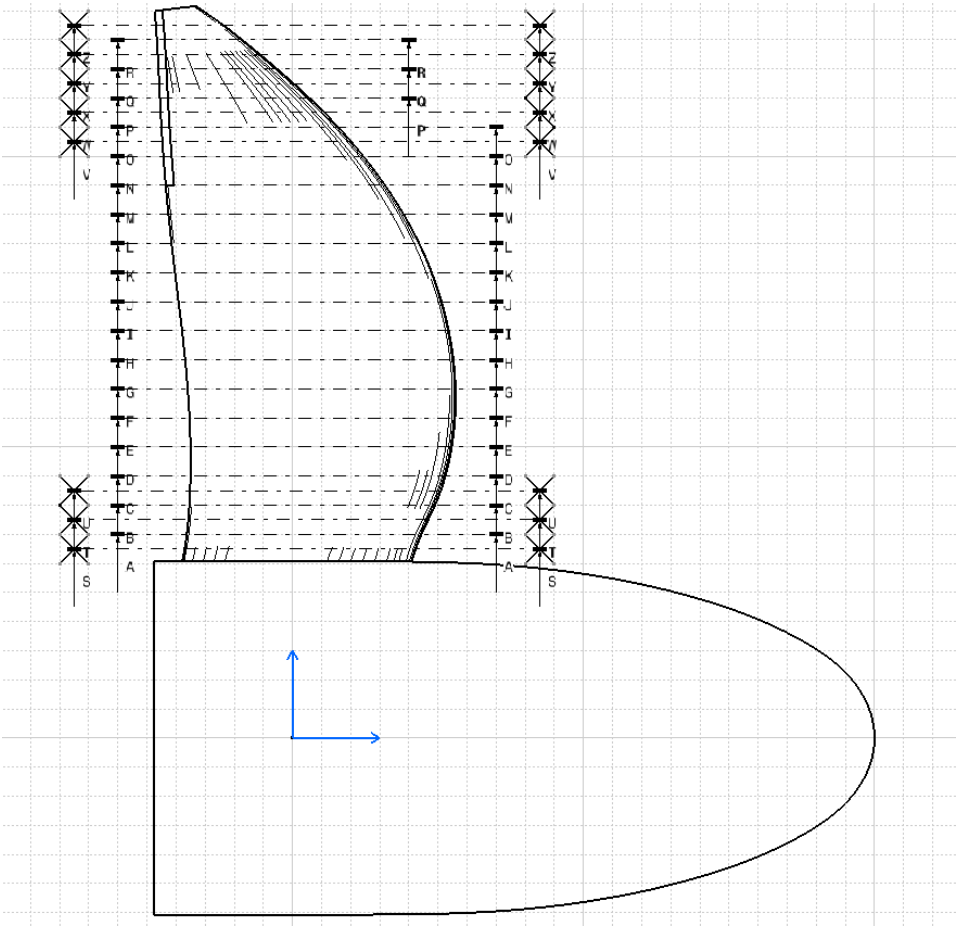

Figure 4.18: Side view of blade and hub showing the radial locations of the measured chord sections (horizontal black dashed lines).

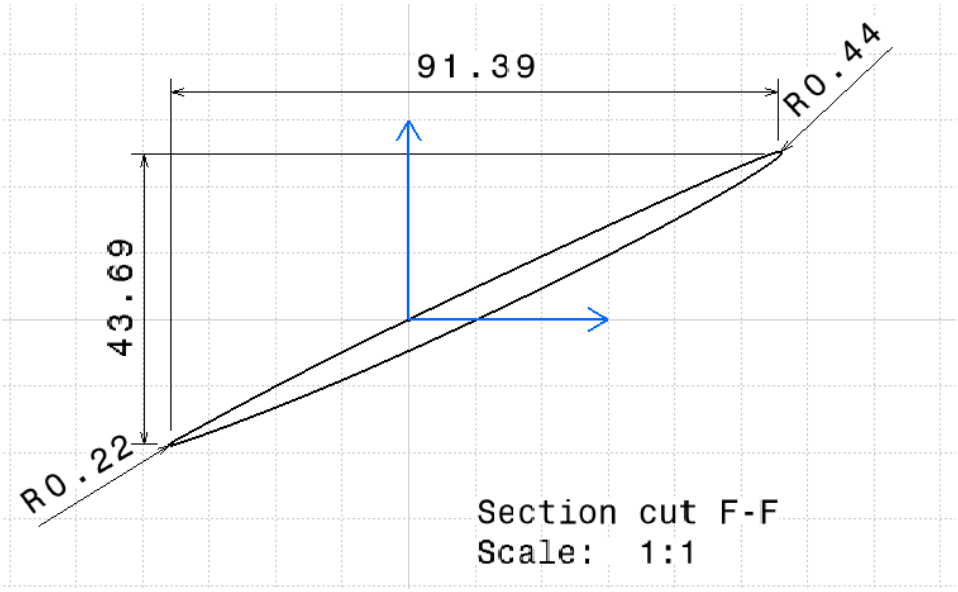


Figure 4.19: Section cut of the blade, showing the $x$ and $y$ dimensions (resp. horizontal and vertical) and the LE and TE radii. All dimensions in $mm$.

Note that XROTOR cannot analyze swept rotors. The initial APIAN rotor for XROTOR is thus the APIAN propeller without sweep. The standard XROTOR airfoil is used for analysis, since it is not known which airfoils are used on the APIAN propeller. At all cross-sections however, the airfoil is relatively thin and has little camber and little thickness variation. The default XROTOR airfoil is used for analysis.

The leading edge (LE) and trailing edge (TE) are rounded, making the localization of the chord line slightly difficult. The solution is to measure the $x$ and $y$ distances (resp. axial and tangential direction) between the center points of the LE and TE arcs. The temporary local blade angle $\beta$ was then defined as:

$$\beta_{temp} = \arctan\left(\frac{y}{x}\right) \tag{4.1}$$

The temporary local blade angle is measured from the vertical direction, which here is aligned with the rotational axis. The blade angle as it is usually defined, as the angle between the tangential direction and the blade chord, is obtained hereafter:

$$\beta = \frac{\pi}{2} - \beta_{temp} \tag{4.2}$$

Using Pythagorean theorem the total distance between the LE and TE arcs center points can be found. To obtain the total chord length, the LE and TE radii are added.

$$c = \sqrt{\left(x^2 + y^2\right)} + r_{LE} + r_{TE} \tag{4.3}$$

The final rotor blade geometry data can be found in Table 4.4.

**Comparison of APIAN rotor model with wind tunnel measurements**

Data from the DNW wind tunnel tests [30] is hard-copied into the code to obtain comparison plots with XROTOR results. The following test cases are analyzed:

- Case 1: 1a, run 22, point 788, $M = 0.23$, $\alpha = 0$, $J = 1.118$
- Case 2: 4a, run 27, MC 864, $M = 0.7$, $\alpha = 0$, $J = 3.115$
- Case 3: 5a, run 27, MC 981, $M = 0.701$, $\alpha = 0$, $J = 2.690$
- Case 4: 6a, run 29, MC 1184, $M = 0.719$, $\alpha = 0$, $J = 3.114$
- Case 5: 3b, run 21, MC 655, $M = 0.2$, $\alpha = 0$, $J = 1.015$

Other cases could not be analyzed since their angle of attack was nonzero, making it impossible to compare XROTOR's $\alpha = 0$ analysis results. All used wind tunnel measurements were made at the axial location of $x/R = 0.7$ or $x = 175mm$. The accompanying documentation does not tell if the measurements are corrected for slipstream contraction. Calculating the slipstream contraction at $x/R = 0.7$ with conventional slipstream contraction methods like Durand's method [31] result in a contraction ratio much larger than found in the measurement data. These conventional slipstream contraction models are therefore not used, the reason is given in Section 2.1. A possible explanation for this specific rotor is that since the $c/R$ ratio of the blades is so large that the rotor cannot be idealized as an actuator disk

Table 4.4: Table containing geometric data from APIAN rotor as measured from the CATIA model.

| Radius [$r/R$] | Radius [$mm$] | Chord [$c/R$] | Chord [$mm$] | Blade angle [°] |
|---|---|---|---|---|
| 0.26 | 65 | 0.333 | 83.27 | 72.702 |
| 0.28 | 70 | 0.339 | 84.85 | 72.338 |
| 0.30 | 75 | 0.349 | 87.21 | 71.756 |
| 0.32 | 80 | 0.359 | 89.79 | 71.060 |
| 0.34 | 85 | 0.369 | 92.23 | 70.272 |
| 0.36 | 90 | 0.377 | 94.25 | 69.457 |
| 0.40 | 100 | 0.390 | 97.50 | 67.806 |
| 0.44 | 110 | 0.401 | 100.22 | 66.136 |
| 0.48 | 120 | 0.413 | 103.17 | 64.581 |
| 0.52 | 130 | 0.418 | 104.39 | 62.774 |
| 0.56 | 140 | 0.420 | 105.12 | 61.210 |
| 0.60 | 150 | 0.421 | 105.15 | 59.727 |
| 0.64 | 160 | 0.418 | 104.38 | 58.311 |
| 0.68 | 170 | 0.409 | 102.33 | 56.932 |
| 0.72 | 180 | 0.395 | 98.67 | 55.578 |
| 0.76 | 190 | 0.374 | 93.40 | 54.291 |
| 0.80 | 200 | 0.347 | 86.64 | 53.111 |
| 0.82 | 205 | 0.330 | 82.46 | 52.578 |
| 0.84 | 210 | 0.312 | 77.89 | 52.053 |
| 0.86 | 215 | 0.291 | 72.76 | 51.496 |
| 0.88 | 220 | 0.268 | 67.07 | 50.975 |
| 0.90 | 225 | 0.243 | 60.80 | 50.512 |
| 0.92 | 230 | 0.216 | 54.10 | 50.019 |
| 0.94 | 235 | 0.188 | 46.99 | 49.520 |
| 0.96 | 240 | 0.159 | 39.65 | 48.968 |
| 0.98 | 245 | 0.128 | 31.87 | 48.567 |

and that the actual measurement location is significantly much closer to the blade TE than the blade axis ($x = 0$).

Cases 2, 3, and 4 are high-speed cases, and XROTOR's analysis does not match the measured velocities well. This might partly be due to the fact that XROTOR cannot handle velocities larger than $M = 1$, and will clip any higher velocity found to $M = 0.99$ while using a simple correction for compressibility. For the high Mach number cases XROTOR would not converge with some ranges of angle of attack, leading to quite large differences for Case 3 and Case 4.

Cases 1 and 5 are run below $M = 0.3$, and can be regarded as being run in incompressible fluid. Here the velocities found by XROTOR match reasonably well with the PIV data. The large $c/R$ ratio, which gives a maximum chord of about 40% of the rotor radius and the swept, curved blade shape will in reality have a significant effect on the velocity profiles in the slipstream. For instance, radial components cannot be analyzed by XROTOR, it being a blade element method, but are almost certainly present in the APIAN rotor slipstream.

Figure 4.20 show for each of these two cases the measured (DNW) and calculated (XROTOR) axial and tangential velocity ratios. The APIAN propeller pitch was changed for all cases to obtain the closest fit, but no pitch change was required for a good fit for the low-speed cases.

The measurement data from the DNW wind tunnels also gives an opportunity to analyze slipstream contraction and changes in axial velocity, since the PIV measurements are made at 3 locations behind the rotor plane. The ratio of axial velocity versus freestream velocity is plotted versus axial distance downstream in the left plot in Figure 4.21. The slipstream radius is defined by the author as the ratio of radial location where the measured induced velocities change sign over the rotor radius. This velocity changeover happens at the blade tip due to presence of a tip vortex. The results are shown in the right plot of Figure 4.21. The conclusion is that for the APIAN rotor, in the downstream range where a possible stator could be placed, there is virtually no change in axial velocity and hardly any change in rotor slipstream radius. For practical purposes the rotor slipstream is considered to have a constant velocity equal to far field velocity and no contraction.

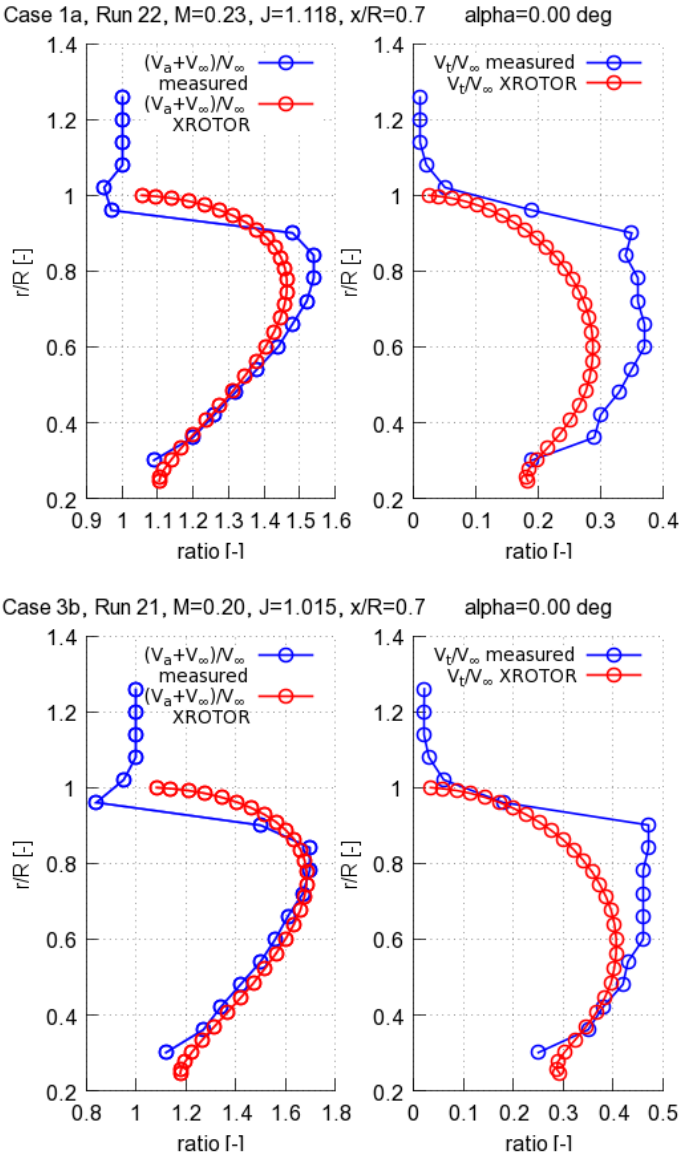


Figure 4.20: Comparison plots of axial and tangential velocity ratios of the two low-speed cases mentioned in the text. Reading left to right, with two graphs per case: Case 1, and Case 5. The 'alpha' value indicates the difference in constant blade angle of attack used to match the data. The rotor axis is aligned with the flow direction.

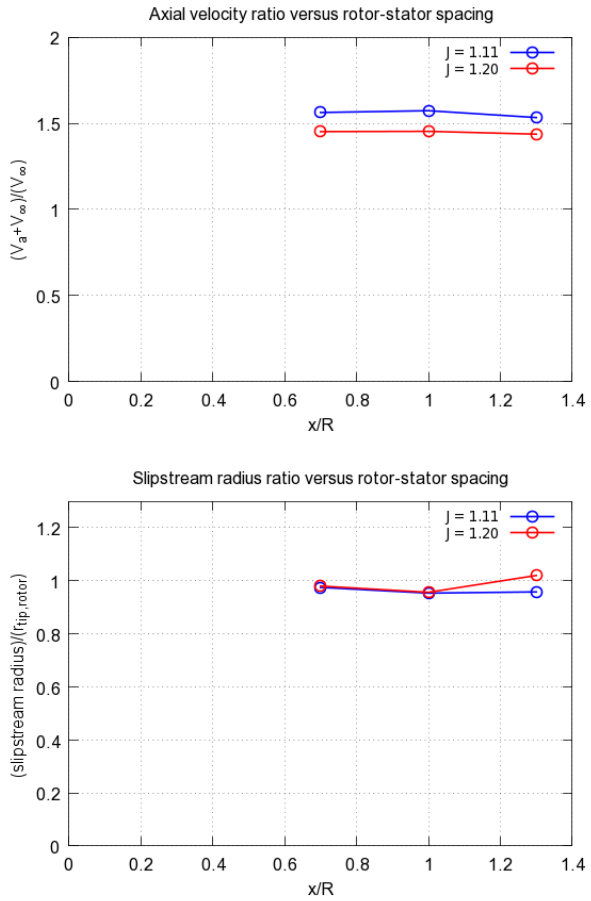


Figure 4.21: Comparison plots of axial velocity ratio and slipstream radius ratio for two different advance ratios, versus axial distance behind the rotor (as multiple of rotor tip radius). It is clear that there is hardly any change in the increase of axial velocity, and that the slipstream radius ratio is rather constant too. The slipstream radius is derived from measurements; defined as the radial location where the measured induced velocity changes from negative to positive at the blade tip.

## 4.4. THE APIAN STATOR

This chapter explains how the stator for the APIAN-INF wind tunnel test program was designed. For more information about APIAN-INF, see Section 4.2. Due to agenda constraints regarding the test program, the rotor-stator analysis program by the author was temporarily frozen during development to design a stator for the APIAN rotor in the summer of 2014. The stator design is therefore not made with the current version of the program. A description of a number of analyzed cases from the program output, and how the 3D CATIA model of a stator blade is made from the data files.

**APIAN Stator design with XROTOR**

XROTOR was used for stator design to make use of the minimum induced loss design routine of XROTOR. The DESI menu asks for certain geometric parameters such as tip radius, hub radius, and number of blades, and general parameters such as flight speed and constant $C_L$ over the blade. The number of blades was initially kept equal to the APIAN rotor for convenience only. The final stator design has 5 blades, to prevent excessive aeroacoustic noise due to rotor and stator blade interference effects. By having a different number of blades, the interference is less as not all rotor blades pass all stator blades at the exact same moments. Increasing the number of blades would also have been an option, but manufacturing issues and the wish to take PIV measurements on one blade settled the number of blades on 5.

The APIAN rotor data shown in Section 4.3 show that for two different advance ratios there seems to be very little slipstream contraction, and no change in axial velocity. Figure 4.21 clearly shows that there is no slipstream contraction, but that the tip vortex center can be found at about 95% of the rotor tip radius. It is this validation of the theory that decided to keep the stator tip radius at 95% of the rotor tip radius and constant for any distance between rotor and stator. No axial velocity corrections such as Durand's method [31] are applied. The hub radius of the APIAN rotor is constant in axial direction, and therefore the stator hub radius is assumed equal to the rotor hub radius. The hub wake radius, needed for XROTOR's analysis, is kept equal to the rotor hub wake radius for the same reason.

A very low rotational speed of $rpm = 1$ is specified since XROTOR cannot handle zero rotational speed. With a rotor *rpm* in the order of a several thousand, for all practical purposes the very slowly rotating stator can be considered static indeed. Note that at that stage of program development the rotor-to-stator power and *rpm* ratios were not yet introduced, power and *rpm* values were hard-copied into the code.

The minimum induced loss routine sizes the chord and blade angle distributions considering a lift distribution with a constant overall lift coefficient over the blade to get an optimal blade loading distribution. As is explained in Appendix C, an iterative process using the slipstream velocities of the rotor as stator flow field input and vice versa results in an converged system where the stator sees an incoming slipstream with nonzero tangential velocities. The combination of local slipstream angle and local blade angle work out such that the local lift vector has a small forward component, which adds to the total system thrust.

**Analyzed cases**

The APIAN rotor data shows that the rotor was analyzed at the high and low advance

ratios, and that the blade pitch angle was changed by several °. The unswept APIAN rotor had to be rotated in blade pitch by several degrees to observe quite close matches to the original wind tunnel data for high Mach numbers ($M = 0.7$), but no rotation was needed for the cases where the Mach number was close to $M = 0.2$. The stator was designed for an advance ratio of $J = 0.90$. The peak increase in propulsion efficiency generally lies near smaller advance ratios. The analyzed advance ratios were $J = 0.35, J = 0.60, J = 0.80, J = 0.90$. Note that the APIAN propeller geometry and pitch angle were not changed; they were as presented in the CATIA model, with a blade angle of $\beta(0.75r/R) = 40.4°$.

After the main program had analyzed numerous cases, a small program read in all the analyzed cases and found the case with the largest efficiency increase for a given airfoil or given stator $C_L$ value. The rather low $C_L$ values give a stator chord comparable to and slightly smaller than the APIAN propeller. The results are shown in Table 4.5. The general trend is that there is a significant increase in propulsion efficiency for the system versus the rotor stand-alone. This increase is the largest at the low advance ratios, and decreases in a more or less linear fashion to a small decrease in efficiency at the design advance ratio. As an example, Figure 4.22 shows the increase in propulsion efficiency versus advance ratio for a stator with NACA 0009 airfoil and a constant $C_L$ value of 0.15 (the version of the code at the time showed a good performance at a rather low $C_L$ value). A more general performance plot for the same case can be seen in Figure 4.23. Here the system power, system torque and system thrust coefficient distributions are visible too.

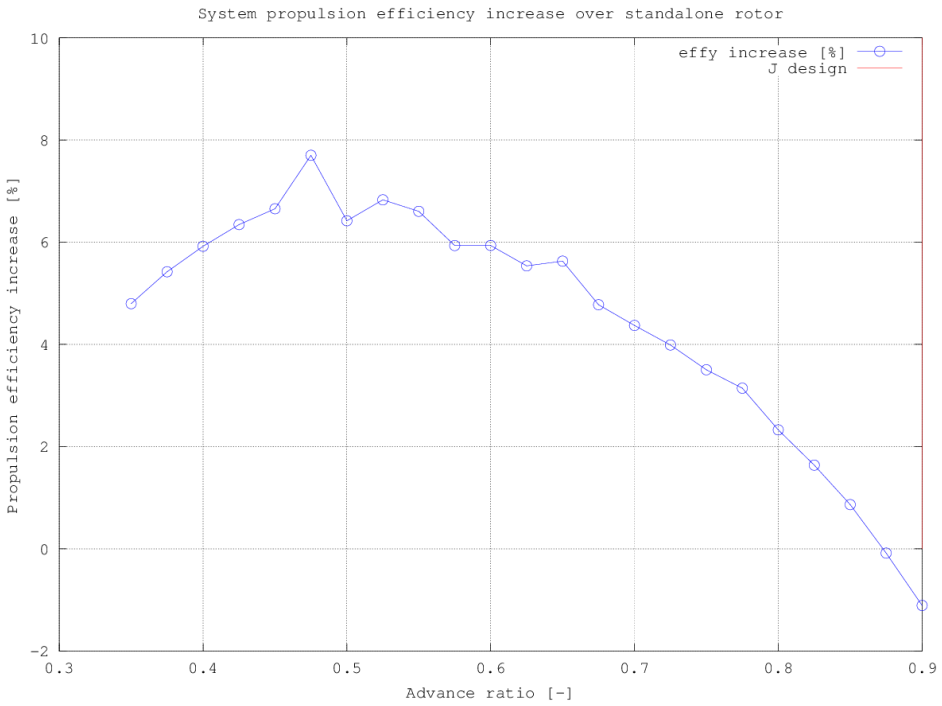


Figure 4.22: Increase in propulsion efficiency versus advance ratio for a stator with airfoil NACA 0009 and a constant $C_L$ value of 0.15. The general shape of the curve is representative of most considered cases. It is assumed that numerical computation effects are the reason for the small sawtooth behaviour. Note that thi s plot was made with an early version of the code, and without stator cropping.

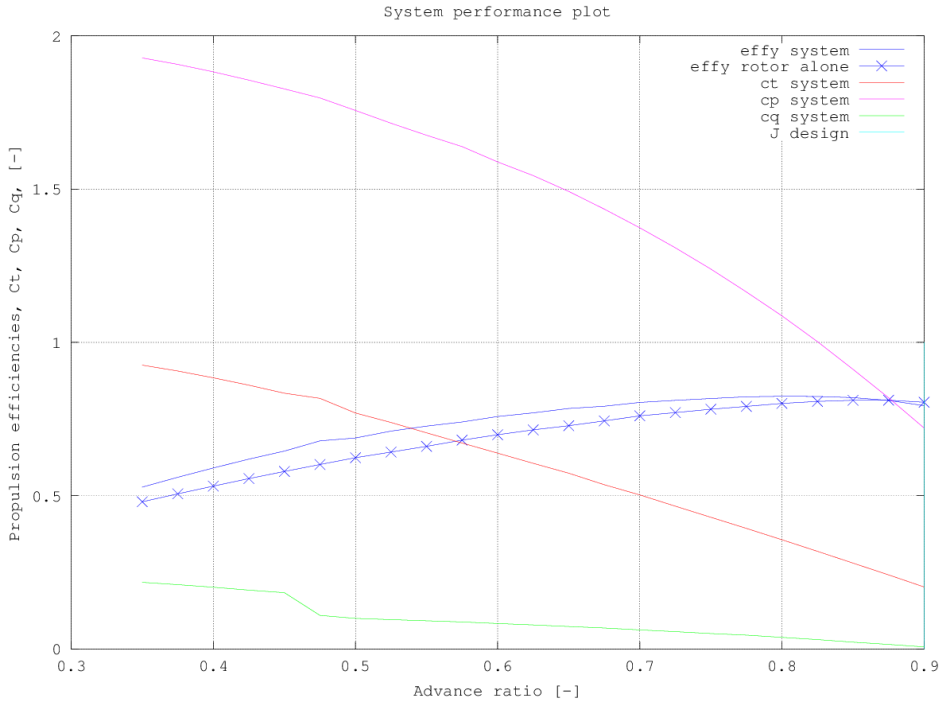


Figure 4.23: Performance plot of the total system. Rotor is APIAN rotor, stator has airfoil NACA 0009 and a constant $C_L$ value of 0.15.

Also note that the cambered NACA 4412 section still shows efficiency improvement at the design advance ratio instead of the performance decrease of the symmetrical NACA 0009 section, but that the chord ratios are very different. Cases 1 and 9 give an almost equal performance increase, which leads to the idea that the blade chord might be a more important parameter for overall performance than choice of airfoil sections.

The main program also outputs x,y,z-coordinate files for the chord section at each radial station. These can be imported into CATIA to create a point cloud or 3D surface. Note that each airfoil section is made by drawing a spline through the points, and that therefore the trailing edge of the airfoil is still open. The 3D surface is created by making a loft through all airfoil sections.

An overview of the geometry of a stator blade from cases 2, 4, 6, and 8 is shown in Figures 4.24 and 4.25. This stator blade uses a NACA 0009 airfoil and has a constant $C_L = 0.15$. It was designed for a freestream velocity of 60 $m/s$ and an advance ratio of $J = 0.90$.

**Suggested stator design for validation**

From Table 4.5 it is clear that for a given $C_L$ matching the APIAN rotor chord, of all analyzed airfoils the NACA 0009 airfoil gives consistently the best efficiency improvement. If the operating advance ratio stays below approximately $J = 0.85$, the system is predicted to perform better than the rotor standalone. The author would suggest using the stator design belonging to the following parameters:

- Airfoil: NACA 0009
- $C_L$: 0.15 [-]

- $V_\infty$: 60 [m/s]
- $J_{design}$: 0.90 [-]
- Stator tip radius over rotor tip radius: 0.95 [-]

A 3-view and 3D CAD drawing of the blade are shown in Figure 4.24 and Figure 4.25 respectively.

Table 4.5: Selected cases from program output. Note the significant increase in propulsion efficiency, especially at low advance ratios.

| **Stator constant $C_L$** | | | | |
|---|---|---|---|---|
| **Case** | **J** | **$C_L$** | **NACA airfoil** | $\Delta\eta$ % |
| 1 | 0.35 | 0.10 | 0009 | 6.178 |
| 2 | 0.35 | 0.15 | 0009 | 4.798 |
| 3 | 0.60 | 0.10 | 0009 | 4.504 |
| 4 | 0.60 | 0.15 | 0009 | 5.935 |
| 5 | 0.80 | 0.10 | 0009 | 1.065 |
| 6 | 0.80 | 0.15 | 0009 | 2.326 |
| 7 | 0.90 | 0.10 | 0009 | -1.626 |
| 8 | 0.90 | 0.15 | 0009 | -1.110 |

| **Stator constant airfoil** | | | | |
|---|---|---|---|---|
| **Case** | **J** | **$C_L$** | **NACA airfoil** | $\Delta\eta$ % |
| 9 | 0.35 | 0.25 | 4412 | 6.184 |
| 10 | 0.60 | 0.25 | 4412 | 6.282 |
| 11 | 0.80 | 0.40 | 4412 | 3.498 |
| 12 | 0.90 | 0.40 | 4412 | 1.126 |

**Final stator design for APIAN-INF wind tunnel test**

While the code was still under development, various stator designs were already made for the APIAN rotor for the APIAN-INF test program of September 2014. In July 2014 a stator design was chosen and 'frozen' while code development continued, the reason being that the stator needs to be produced by the faculty workshop and integrated in the overall test setup. The chosen design is by no means the very optimum design attainable, but as Figure 4.26 shows, it will deliver an efficiency increase of about 2.5% in the lower end of the advance ratio range. Such behavior is typical for many stator designs found for the APIAN rotor. Full design details can be found in Table 4.6. For simplicity the stator originally was assumed to have the same number of blades as the rotor, but conventional wisdom holds that while this might not affect performance, aerodynamic interference creates unwelcome noise. More blades would increase production time and material costs, and therefore a blade number of 5 was chosen to stay as close to 6 blades as possible. The code showed that the performance decrease between 5 and 6 blade cases would be small. The stator was designed for a rotor advance ratio of $J = 1.75$, since it was assumed that the rotor-stator combination should have good performance at cruise conditions, which would ask for high

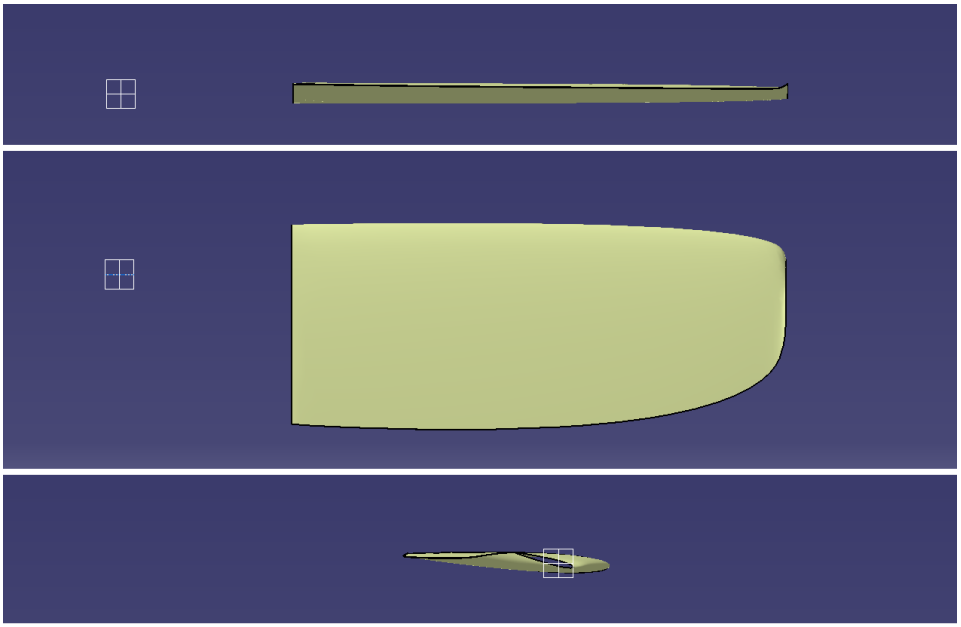

Figure 4.24: 3-view of statorblade from cases 2, 4, 6, and 8, in CATIA. The white mark denotes the origin at the rotational axis.

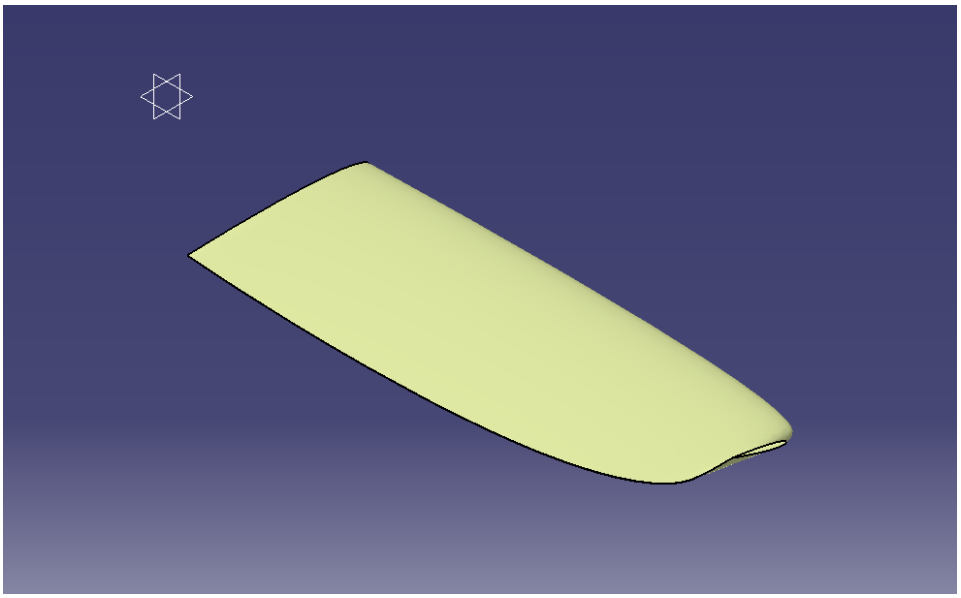

Figure 4.25: Isometric view of statorblade from cases 2, 4 ,6, and 8, in CATIA. The white mark denotes the origin at the rotational axis. Flow direction: upper right to lower left.

advance ratios. A power of $1W$ and a *rpm* of 1 where used to create the stator. Numerous runs with varying input parameters showed that a symmetrical airfoil performs about as good or better than a cambered airfoil. Decreasing thickness improves airfoil performance too, but practical, structural limitations led to a choice of a NACA 0009 airfoil for the final stator design. The stator was produced by the TU Delft Aerospace Faculty workshop from 7075 aluminum. The performance graph can be found in Figure 4.27, and a top and aft view of a statorblade in Figures 4.28 and 4.29.

As can be seen in Figure 4.30, the stator blades are connected to the hub by flanges. These flanges together form a ring of $5mm$ thickness, which adds to the local hub diameter. As the actual flange thickness was not determined yet at design freeze point, it was not taken into account in designing the stator. E. J. van den Bos of the TU Delft Aerospace faculty later designed the flanges and incorporated them into the CATIA design file to finalize them for milling operations. Since radial flow will exist in the blade root part, which cannot be modeled by XROTOR anyway, the issue was deemed to be not so important. The front edge of the flanges were gradually thinned to create a rather smooth connection with the rotor support structure. Each blade was connected by four bolts to the support tube. The spacing does not have an influence on the stator design, it was a fixed value due to the hub geometry, but is given here for completeness. Figure 4.31 shows three views of a completed statorblade with hub, neatly showing the large twists near the blade root and tip.

Table 4.6: Final APIAN stator design parameters, design 'frozen' in July 2014 for wind tunnel tests. The assumed 'Slipstream contraction' refers to an imaginary case where the hub radii of rotor and stator are equal. Appropriate slipstream scaling for nonequal hub radii is taken care of by the program.

| Final APIAN stator design parameters | | |
|---|---|---|
| **Parameter** | **Value** | **Unit** |
| Airfoil | NACA 0009 | [−] |
| Constant $C_l$ | 0.35 | [−] |
| Airspeed | 60 | $[m/s]$ |
| Rotor advance ratio | 1.75 | [−] |
| Rotor-stator spacing | 0.6 | $[s/R]$ |
| Number of blades | 5 | [−] |
| Hub radius | 90 | $[mm]$ |
| Tip radius | 221.95 | $[mm]$ |
| Slipstream contraction | 0.95 | $[r/R]$ |
| Stator cropping | 0.90 | $[r/R]$ |

The stator tip radius is found by the scaling method described in Section C. The increase in hub radius is assumed to push the streamtube outwards such that the streamtube radius equals $258.67mm$ at the stator plane. Multiplying this figure by the slipstream contraction ratio and the stator cropping ratio, results in a stator tip radius of $r_{tip} = 221.16mm$. The very small discrepancy in stator radius of $0.79mm$ must be sought in the XROTOR blade modeling routine, which might not place the most outward section at the exact blade tip, and calculation machine accuracy.

A document was prepared for DNW to show that the proposed stator blade design, milled from Al 7075, is in accordance with their structural requirements for objects to be mounted in the wind tunnel. It can be found in Appendix A.

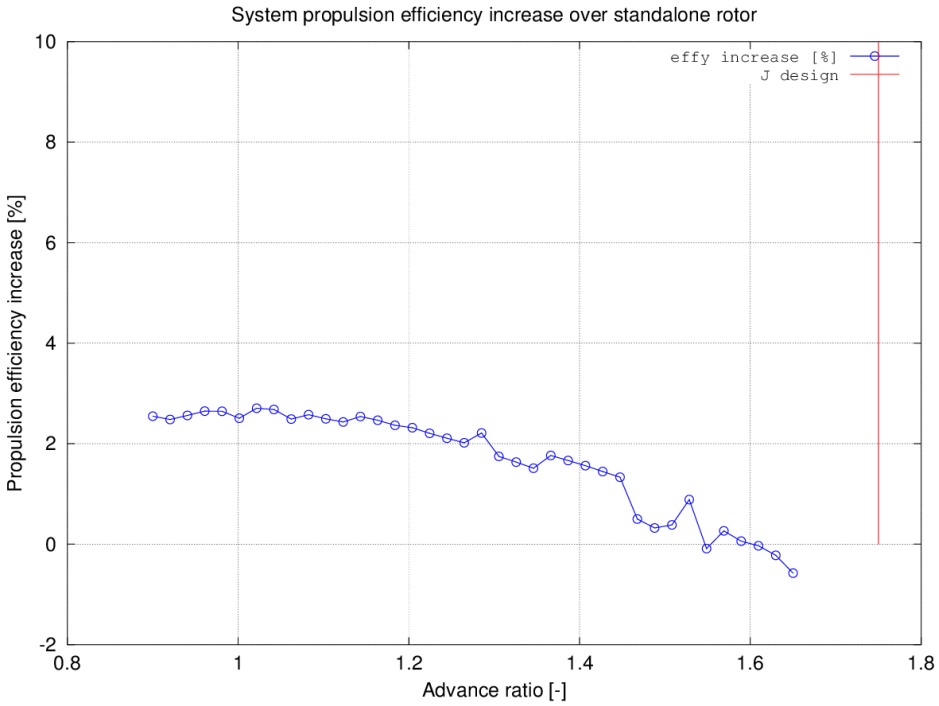


Figure 4.26: Propulsion efficiency increase in % of the rotor-stator system over a stand-alone rotor for the APIAN-INF wind tunnel test. The upward 'wiggles' seen at the right end of the graph are due to convergence issues which were not fully resolved in the code at the time. The red vertical line indicates the design rotor advance ratio for which the stator is designed.

**Simple BEM validation of stator design**

In the same way as the F50 simple BEM method, the APIAN stator design is checked. Due to the large difference in hub ratio and stator cropping, a significant slipstream contraction takes place. Therefore it is not longer valid to assume that the location of the three rotor BEM segments correspond to the stator BEM segments. Figure 4.32 shows the new distribution of segments, whereby the the segment edges are placed on the same streamlines.

The results for both APIAN rotor and APIAN stator are displayed in Table 4.7. Alike the F50 results of Section 4.1, the rotor values match quite reasonably. Again the thrust is a bit more off than the torque, with respectively 14 and 3% overprediction by simple BEM. The stator results are much different. The stator torque values are only 1% different, which is again close, but the exceptionally good match is probably a concidence as there is no solid reason why a three-segment BEM would match so closely with the more refined XROTOR BEM model. A large difference can be seen in the thrust values: a staggering difference of $-142\%$ is found, although the absolute value is much smaller than the rotor value with $0.17N$ versus $46.1N$ for the simple BEM results. With blade angles of near 90° for the stator, the lift vector is almost aligned with the torque direction. Therefore it is not surprising that the torque values match so well, as they are mainly generated by the $\cos(\chi)$ component of the lift. Since the thrust values are much more sensitive due to their dependence on the

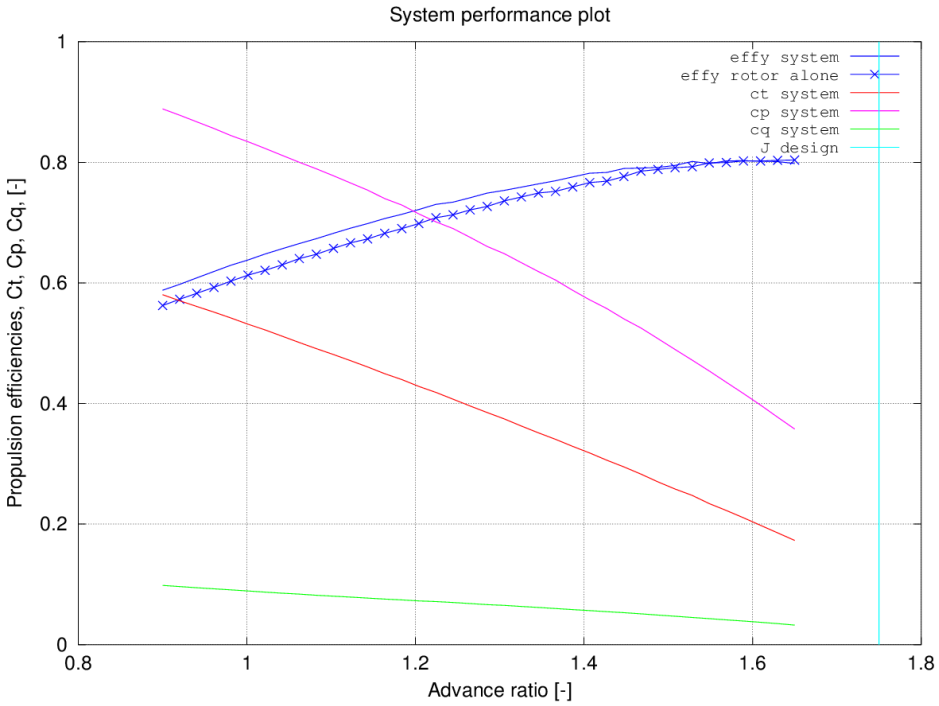


Figure 4.27: Performance graph of the rotor-stator system for the APIAN-INF wind tunnel test. The upward 'wiggles' seen at the right end of the graph are due to convergence issues which were not fully resolved in the code at the time. The cyan vertical line indicates the design rotor advance ratio for which the stator is designed.

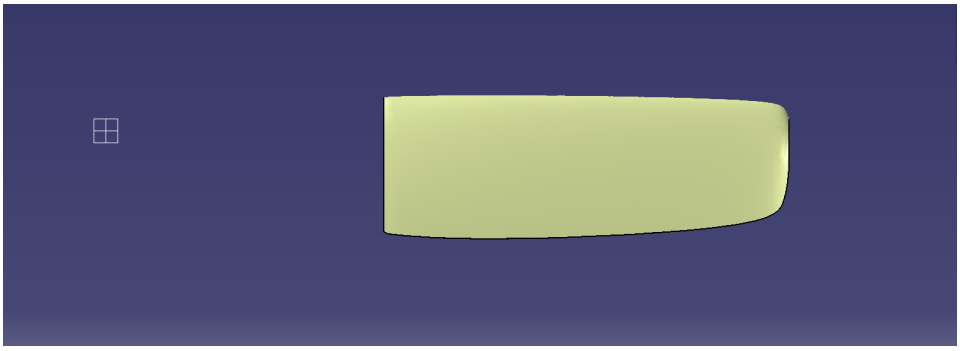

Figure 4.28: Top view of designed stator blade. The rotation axis runs vertically through the white mark on the left, with the air flow from top to bottom. Stator hub not shown.

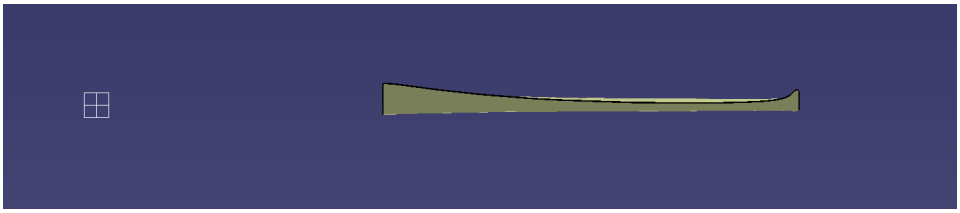

Figure 4.29: Aft view of designed stator blade. The blade angle distribution can clearly be seen, especially the large change in blade angles near the blade tip. Stator hub not shown.

Figure 4.30: Finished stator in the workshop, front side shown. The chamfered flange leading edge and bolted connections can clearly be seen. The support tube is 180$mm$ in diameter. Photo by author.

Figure 4.31: Three views of a completed stator blade with hub, painted in anti-reflective paint for PIV measurements. The middle image clearly shows how the twist near the root and tip gets quite large. The blade is located on the upstream part of the hub.

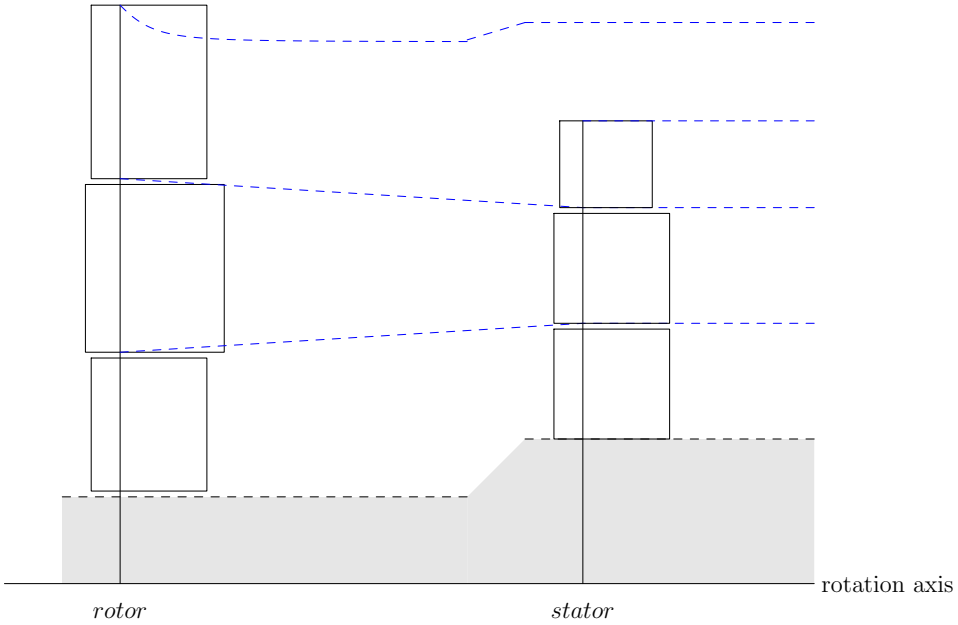


Figure 4.32: Schematic view of 3-segment rotorblade and 3-segment statorblade as used for the simple BEM analysis, with streamlines indicated with dashed blue lines. Note how due to stator cropping the tip segment of the stator does not see the full slipstream of the rotor tip segment. Also note how the stator segments vary in size compared to the rotor segment due to different stator radii compared to rotor radii.

$\sin(\chi)$ components of the lift vector, the large difference in percentage can be explained. Again the overall conclusion is that the simple BEM is reasonable ($< 10\%$) for torque predictions, rather reasonable for rotor thrust predictions, but not trustworthy for stator thrust predictions due to large sensitivity to $\sin(\chi)$.

Table 4.7: Data from a simple 3-segment BEM analysis of the APIAN rotor and stator. A performance comparison of the simple BEM model with the XROTOR BEM model. The rotor was run at $J = 1.75$.

| **Parameter** | **Value** | **Unit** |
|---|---|---|
| Rotor thrust (simple BEM) | 46.1 | $[N]$ |
| Rotor thrust (XROTOR) | 40.3 | $[N]$ |
| % difference | 14.39 | [%] |
| Rotor torque (simple BEM) | 7.43 | $[Nm]$ |
| Rotor torque (XROTOR) | 7.23 | $[Nm]$ |
| % difference | 2.75 | [%] |
| Stator thrust (simple BEM) | 0.17 | $[N]$ |
| Stator thrust (XROTOR) | -0.40 | $[N]$ |
| % difference | -141.62 | [%] |
| Stator torque (simple BEM) | 5.00 | $[Nm]$ |
| Stator torque (XROTOR) | 4.93 | $[Nm]$ |
| % difference | 1.23 | [%] |

# 5

# ROTOR-STATOR SLIPSTREAM AND WING INTERACTION

## 5.1. THE LANCHESTER-PRANDTL LIFTING LINE MODEL

The lifting line is a fast and simple method to analyze the aerodynamic performance of a wing. A wing is built up of 2D airfoil sections, and as such the lift and drag of a total wing can be calculated due to the wing geometry. The performance of an airfoil can be measured in the reaction forces perpendicular and parallel to the flow due to circulation along the airfoil; lift and drag. However, there is an extra drag component present: the induced drag, or 'drag-due-to-lift'. Because a wing has a finite span, the pressure difference at the wingtips must go to zero. This influences the flow over the whole wing, which manifests itself as an extra drag component, and a variation in local angle of attack along the wing. The lifting line method, discovered by Lanchester but improved on by Prandtl, is an excellent method of calculating the induced drag of a wing by making use of this angle of attack variation. The lifting line method is explained in many study books and websites, but the book on aerodynamics by Anderson [32] gives an excellent overview of both the lifting line theory and it's history. A short overview of the method is given below, and an additional section explains how a rotor slipstream influences the circulation distribution found by the lifting line method.

**The origin: electromagnetism and vortices**

The Biot-Savart law could be used to describe the effect of a vortex filament on a certain point. Originally the equation was used to describe the magnetic field around an electric current running through a wire. One of the simplest forms deals with an infinitely thin wire through which an constant current $I$ flows. The resultant magnetic field $\mathbf{B}$ at a point $\mathbf{r}$ is found by evaluating a line integral over the wire (shown without derivation):

$$\mathbf{B} = \frac{\mu_0}{4\pi} \int_C \frac{I\mathbf{dl} \times \mathbf{r}}{|\mathbf{r}|^3} \tag{5.1}$$

Helmholtz saw analogies with a vortex filament in aerodynamics: line with a certain circulation could replace the electric current running through a wire, and the velocity induced on a point outside the line replaced the magnetic field. He also established two principles which hold for the vortex behavior in inviscid, incompressible flow:

- A vortex filament has constant strength along its length
- A vortex filament cannot end in a fluid; it must form a closed path or extend to $\infty$.

**Modeling a wing**

A wing can be seen as a device which adds circulation to a flow. An airfoil section placed in a freestream steady flow creates a certain circulation. In incompressible and inviscid flow, the complex flow around the airfoil can be modeled as simply the sum of an undisturbed freestream flow plus circulation. A vortex is a good way of modeling such circulation. If the airfoil is now extruded to infinity, a wing of infinite span is created. It can thus be modeled as a vortex line or vortex filament, placed in an undisturbed flow. The infinite wing does not exist, as real wings have a finite span. However, a vortex filament cannot just end at a wingtip according to the vortex filament principles by Helmholtz. A solution is to add an additional vortex filament to each wingtip, extending to $\infty$. By placing these filaments in the freestream direction instead of spanwise, they do not add to the lift of the system, but only increase the downwash. Figure 5.1 shows how this vortex filament system looks.

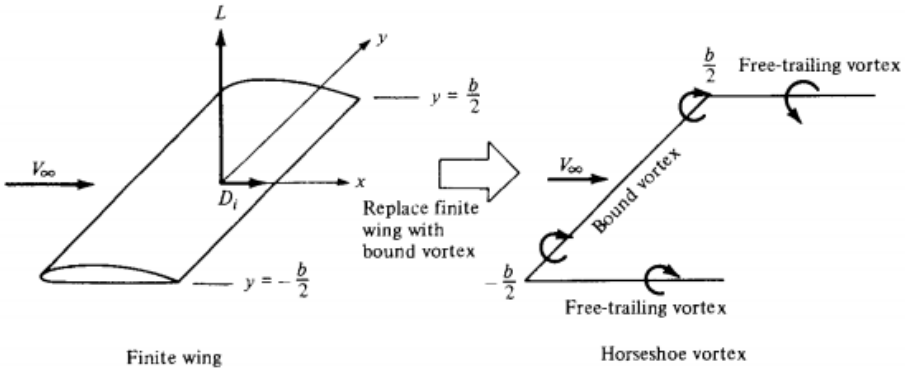


Figure 5.1: Modeling a finite wing by using a bound vortex. Taken from Anderson, [32]

**Discretization**

There is however a problem with this model; at the wingtips the downwash, induced by the trailing vortices, increases to $\infty$ strength, see Figure 5.2. This is not physically possible and the downwash distribution is not very accurate compared to the real-life situation. A solution is to superimpose a number of horseshoe vortices of different length, along a single line: the lifting line. See Figure 5.3. Each spanwise step in circulation creates a trailing vortex with a strength equal to the step in circulation. With this model, the lift distribution can be approximated much more accurately, and all trailing vortices together give a much more accurate downwash distribution.

The limit case is of course a lifting line consisting of an infinite amount of superimposed horseshoe vortices, The circulation distribution becomes continuous, as the step size between two successive vortices goes to zero. Figure 5.4 shows such a model; the downwash imposed on a point along the wingspan by all trailing vortices can be calculated by using the following integral:

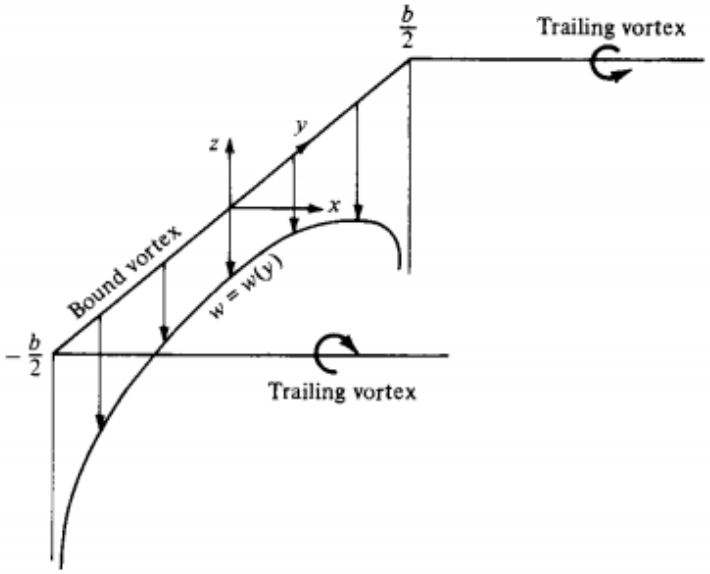


Figure 5.2: The problem: the downwash becomes infinitely strong at the wingtips by using only one horseshoe vortex. Taken from Anderson, [32]

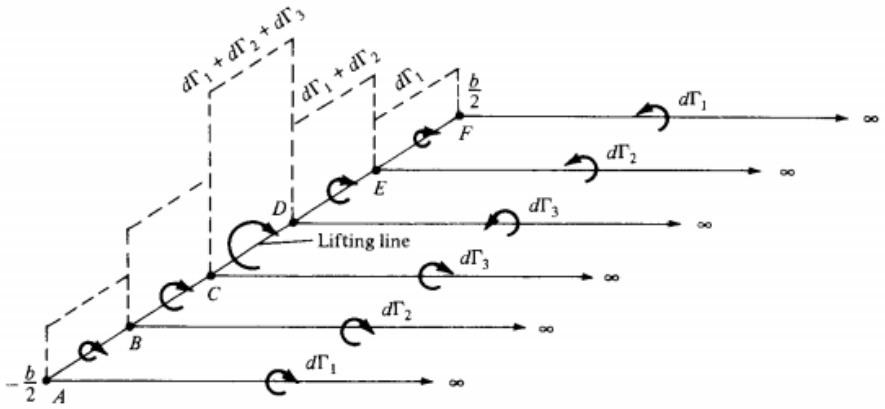


Figure 5.3: The solution: model the wing using multiple horseshoe vortices along the lifting line. Taken from Anderson, [32]

$$w(y_0) = -\frac{1}{4\pi}\int_{-b/2}^{b/2}\frac{(d\Gamma/dy)\,dy}{y_0 - y} \tag{5.2}$$

While this equation relates the downwash to the trailing vorticity, it assumes that the circulation distribution is known beforehand in order to calculate the downwash and induced drag. This is generally not the case, but the angle of attack distribution of a given wing is known. Without giving the full derivation, which is present in many textbooks on the subject, the local geometric angle of attack is of great importance, and can be expressed as follows:

$$\alpha_{geo} = \alpha + \alpha_0 + \alpha_i \tag{5.3}$$

In lifting line theory the lift slope is assumed to be $2\pi[1/rad]$. Because cambered airfoils can have nonzero lift at $\alpha = 0$, for the calculations it is necessary to add this $\alpha_0$ to find the total or geometric angle of attack as 'seen' by the lift slope. The induced angle of attack is added to allow for downwash effects, and will generally be negative as to reduce $\alpha_{geo}$. This is why the circulation and therefore lift diminish near the wing tips. Writing out Equation 5.3 in full for the influence of the full circulation on a certain point $y_0$ on the lifting line gives:

$$\alpha_{geo}(y_0) = \frac{\Gamma(y_0)}{\pi V_\infty c(y_0)} + \alpha_0(y_0) + \frac{1}{4\pi V_\infty}\int_{-b/2}^{b/2}\frac{(d\Gamma/dy)\,dy}{y_0 - y} \tag{5.4}$$

This equation is the very core of Prandtl's lifting line method. By dividing a wing into a number of spanwise nodes, and setting up this equation for each node, a system of equations is formed which can be solved by elementary matrix operations. The solution then contains the circulation distribution from which the total lift of the wing can be found. The induced drag can be found from the induced angle of attack distribution. Summing the induced drag and the profile drag of a wing gives the total drag of that wing.

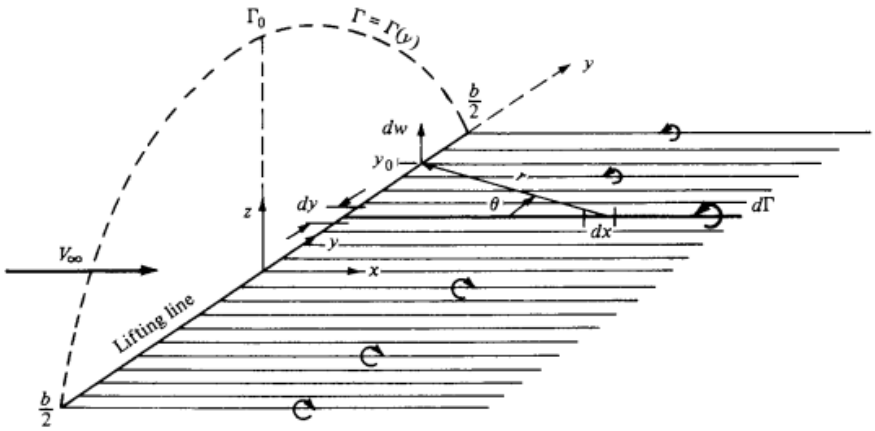


Figure 5.4: Limit case; the superposition of $\infty$ horseshoe vortices along the lifting line. Taken from Anderson, [32]

## 5.2. ROTOR-STATOR SLIPSTREAM AND WING INTERACTION

This chapter discusses the aerodynamic interaction between a rotor or stator slipstream with a wing mounted downwind. A method is sought to assess the influence of rotor or stator slipstream on a wing, with the emphasis on being quick and yet reasonably accurate. The limitations of the current rotor or stator slipstream model and its effects on the aerodynamic modeling of the wing are explained next. The implementation of the lifting line method from Section 5.1 is explained. The code can be found in Appendix D.

**Limitations and difficulties of modeling a wing in a rotor or stator slipstream**

A few assumptions are made up front:

- The wing is in a steady horizontal symmetrical flight; it therefore sees a constant velocity (free-stream velocity) along the whole span.
- The lifting line is assumed to be straight; the wing is unswept and has no dihedral.
- The slipstream velocities of a rotor, or a rotor-stator system, are circumferentially averaged and as such considered to have reached far wake values when they intersect the wing.
- The rotor's rotational axes are perpendicular to the wing, aligned with the free-stream velocity vector and in-plane with the lifting line.
- The axial slipstream of a rotor, or a rotor-stator system is added to the free-stream velocity, such that the total lift of the wing changes.

The second item mentions that the the lifting line is straight. At first glance it seems that the method is rather limited since only unswept wings with no dihedral can be analyzed. As propeller aircraft are generally flying not too fast, $M < 0.7$ it is not uncommon to see unswept wings or wings with only small sweep. The lifting line might be a adequate tool for preliminary analysis, in lieu of more advanced panel methods which can handle much more geometric freedom. Most aircraft wings have dihedral values less than 5°, such as the Fokker F50, which has a dihedral of 2° on the outer wing sections. Such wings can easily be modeled accurately by the lifting line method since the out-of-plane component remains negligible.

Concerning the last item in the list above, XROTOR's output gives slipstream velocity profiles as were they circumferentially averaged. For a rotor-wing combination, where the rotor *rpm* is rather high as with most contemporary aircraft, this is acceptable. Seen from the wing, the wakes of every blade passage follow in quick succession and a time or rotor disk averaged model such as the far wake, circumferentially averaged model of XROTOR is a good approximation. A stator, however, does not rotate and therefore the blade wakes are trailing downstream with little rotation. The position of a stator blade with respect to the wing has therefore a large influence in the slipstream velocity components seen by each part of the wing downstream of a stator. Since there is no way to know how the stator blades are mounted on an actual model or aircraft, it was decided to still use the circumferentially averaged far wake model of XROTOR in lieu of a better approach. Ideally the stator removes

most if not all of the tangential slipstream component imparted by the rotor, and the axial component of the stator is small. This means that in the ideal case, there should be no problem using the circumferentially averaged model as there is hardly any trailing wake seen.

**Lifting line with slipstream modeling**

An aircraft wing is modeled as a symmetrical wing with no dihedral and no sweep. Each wing half consists of two trapezoidal panels. Each wing half plan-form is defined by the root chord $c_{root}$, the tip chord $c_{tip}$, the chord at the joining of the two trapezoidal panels, $c_{kink}$, the half wingspan $b/2$, and the kink spanwise location; see Figure 5.5. This chord section joining the two trapezoidal panels is called 'kink' due to the kink in the leading and trailing edges seen at many combinations of chords and kink spanwise locations, and can be found at spanwise location $y_{kink}$.

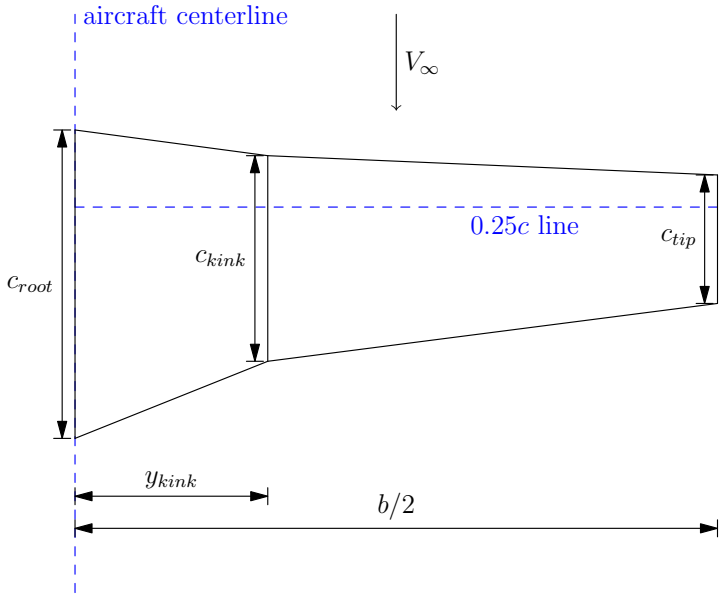


Figure 5.5: Geometry of one wing half. The three defining chord sections are placed on a straight $0.25c$ spanwise line perpendicular to the flow $V_\infty$, which will become the lifting line. It can clearly be seen why the inbetween chord section is called 'kink': both LE and TE have a kink.

For plotting purposes the airfoils are assumed to have their aerodynamic center at $0.25c$, placed on a straight spanwise line. Furthermore at each of the three spanwise locations an angle of attack can be defined, and an airfoil. Wing twist is thus included in the angles of attack. The program will automatically run XFOIL for each airfoil to find the $\alpha_0$. The user can also opt to manually input these zero-lift angles in case there are no airfoil files available.

With the angle of attack, zero-lift angle of attack, and chord distributions in place, a cosine distribution of $N$ nodes (user input) is made over the full span. Figure 5.6 shows how such a distribution can be made by using $N$ points placed on a half circle, spaced equidistant by angle $\theta = \frac{\pi}{N}$. Note that the lifting line theory cannot have a node at the end of the lifting line, as this would make the change in circulation infinite. The first and last nodes are therefore spaced by $\frac{\theta}{2}$.

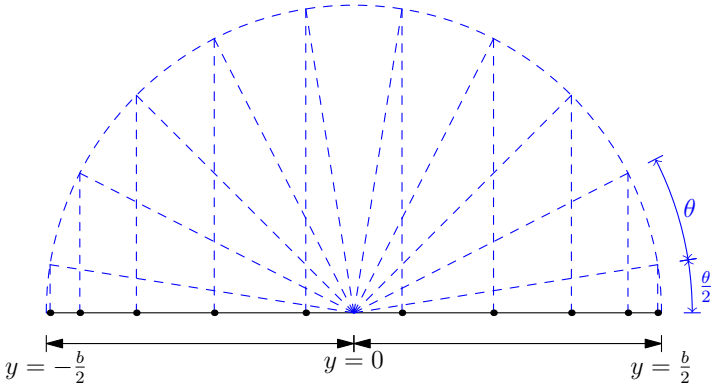


Figure 5.6: Geometry of the lifting line. Nodes (black dots) are placed with a cosine distribution along the lifting line. The dashed arc and vertical lines indicate how a cosine distribution can be geometrically built from points spaced with equal angle $\theta$ along a half circle. Because the lifting line method cannot mathematically have a node at the very end of the lifting line, the node distribution starts at $\frac{\theta}{2}$ along the arc.

At each of these nodes $c$, $\alpha$, and $\alpha_0$ are found by interpolation. A velocity of $V_\infty$ is seen in the axial direction. The out-of-plane component (z-component) is 0 for the uninstalled case, but can be nonzero in the rotor or system slipstream. The program therefore analyses three cases; it starts with installed tractor rotors as baseline configuration, then a case with installed rotor-stator systems, and finally as comparison the uninstalled case without any propulsion elements but at the same lift. Rotor or system slipstreams are read in from `*.vput` files, and also the tip and hub radii are found. The rotors are placed at a spanwise distance $y_{rotor}$ of the wing centerline. It is the user's responsibility to choose a valid value for this distance, such that the streamtubes to not fall outside the wing tips or overlap at the wing center.

The lifting line nodes which are found inside the slipstream tube are affected in both the x-component and z-component velocities. Both the axial and tangential slipstream velocity distributions are fitted to a polynomial from which the actual velocities at each node can be found. The velocity in x-direction becomes $V_\infty + V_a$. For a node behind an upward rotating blade, the velocity in z-direction becomes $0+V_t$, and for a downward rotating blade it simply becomes negative; $0-V_t$. Figure 5.7 shows how such velocity distributions might look over a wing with two rotors in uninstalled and installed case.

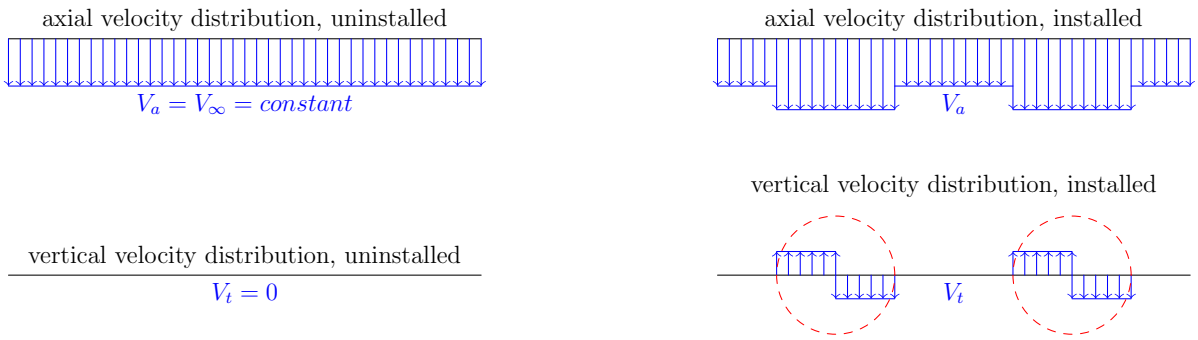


Figure 5.7: Schematic view of axial and vertical (tangential) velocity distributions over a wing in respectively top view and aft view, in uninstalled and installed cases. Both rotors turn in the same direction, and in this example the axial and tangential velocity increases are constant over the slipstream radius. The spanwise locations of the slipstreams can be inferred from the red dashed circles in the lower right figure.

The second and third case will see a constant $\Delta\alpha$ over the full wingspan, to have the wing operate at the same lift as the first case. This is done to be able to compare span efficiency values.

Note that there is a difference between the much-used Oswald factor and the span efficiency. Lifting line theory assumes that the profile drag coefficient of the section is constant regardless of $\alpha$ or $C_l$, which is approximately true for a limited $\alpha$ range around the design condition. The Oswald factor takes into account a quadratic profile drag estimation, which gives better results over a far greater $\alpha$ range. For this analysis used in this report, the profile $C_{d0}$ is set by the user. The overall wing incidence angle change $\Delta\alpha$ is small between installed and uninstalled cases, and thus the use of span efficiency factor $e$ is warranted.

A change in overall angle of attack from the baseline configuration also means that the wing-mounted engines are also operating at an angle of attack. Since this $\Delta\alpha$ is rather small, typically in the order of a few $^\circ$ at most, is the effect of this $\Delta\alpha$ on the propulsion system is neglected, as for small $\alpha$ it holds $\cos(\alpha) \approx 1$. Similarly, the vertical or z-component of the propulsion system which would add to the lift of the system, is even less influenced ($\sin(\alpha) \approx 0$) neglected as well.

Referring to Equation 5.3, the combination of axial and tangential velocities in effect change the angle of attack $\alpha$ of that particular node of the lifting line by an amount $\Delta\alpha$:

$$\Delta\alpha = \arctan\left(\frac{V_t}{V_\infty + V_a}\right) \tag{5.5}$$

The vertical component $V_t$ increases or decreases $\Delta\alpha$ depending if it is respectively the upward moving or downward moving blade. The increase in horizonal component $V_a$ always very slightly decreases the change by increasing the total axial velocity. See Figure 5.8 for a schematic view of this velocity triangle, for both upward and downward moving blades.

The combination of increased $V$ and a change in $\alpha$ changes the local circulation. The lifting line method takes care of finding the influence of all of such changes onto each other, and the result is a circulation and lift coefficient distribution which have distinct 'lying-S' shaped undulations at the location of the slipstreams. The variations in circulation point to increased vorticity in the wing wake, which is a measure for induced drag.

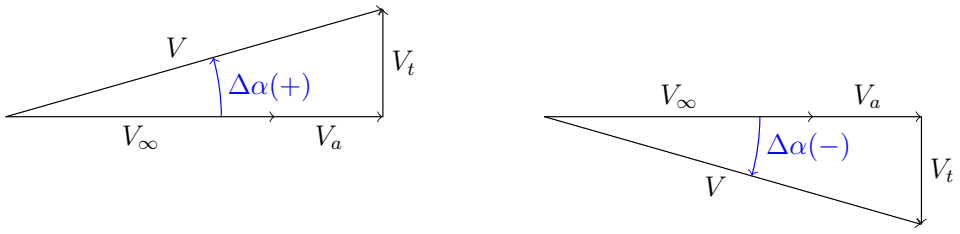


Figure 5.8: Schematic views of changes in local angle of attack due to slipstream tangential velocity components. The left figure shows the case where a rotor blade passes in upward direction, creating an upward slipstream velocity component. The right figure shows a downward passing blade case.

**Effect on aircraft performance**

The case considered here is an aircraft in steady, symmetric, and horizontal flight conditions. Such an aircraft can be considered a point mass for this analysis, see Figure 5.9, and adheres to the following equations:

$$L = W \tag{5.6}$$

$$T = D \tag{5.7}$$

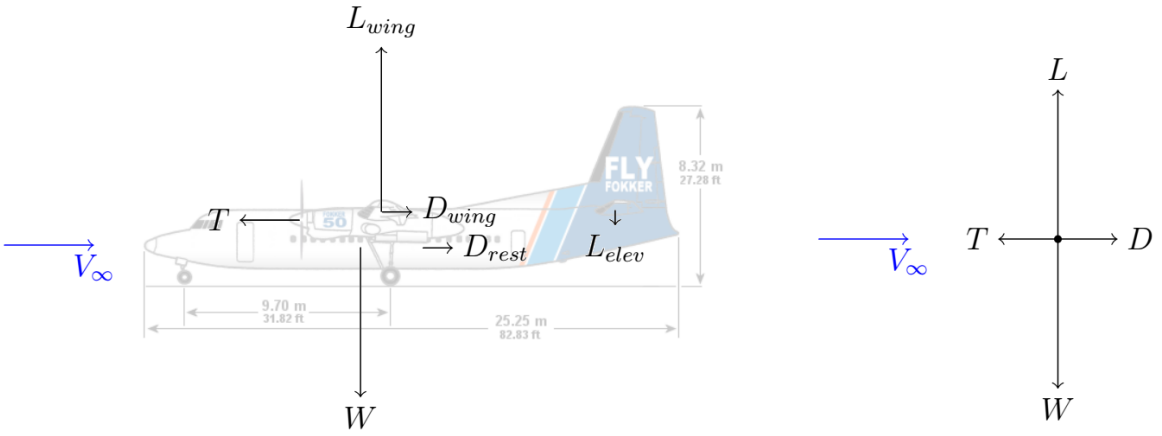


Figure 5.9: An aircraft (Fokker F50) in steady horizontal symmetric flight (left), and the same situation idealized as a point mass (right). Fokker F50 side view from the Fokker website [33].

Any component in the airstream will generate lift and drag. The two main lift generating components are the wing and the elevator, where the latter generally has a downward component for control stability reasons.

$$L = L_{wing} + L_{elev} \tag{5.8}$$

Since the downward lift on the elevator is generally small compared to the main wing, for the lifting line analysis here it is assumed that the aircraft lift is fully and only generated by the wing;

$$L = L_{wing} \tag{5.9}$$

Assuming that the weight is constant for the three cases explained earlier, the lift is therefore equal too. The aircraft drag can be split up in two main components in this example:

$$D = D_{wing} + D_{rest} \tag{5.10}$$

Where $D_{rest}$ is the combined drag of all aircraft parts that are not the wing, and is assumed constant. This includes the engine nacelles since these are not modeled by the wing's lifting line analysis, although they might be mounted on the wing. The wing drag $D_{wing}$ consists of a profile drag and induced drag part. The latter is found using lifting line theory, the former can include viscous effects depending on the airfoil analysis method. It is evident that when then the total drag changes, the required thrust changes too. For the two installed cases mentioned in this chapter, it means that the rotor or system thrust and their slipstreams are different too. An iterative approach is needed to combine a rotor or rotor-stator system analysis with a wing model which has equal lift in all uninstalled and installed cases.

Propulsion efficiency is generally expressed as:

$$\eta = \frac{TV}{P} \tag{5.11}$$

It is clear that in equilibrium flight when $T = D$ and $D = \frac{P}{V}$, the aircraft efficiency $\eta' = 1$ for all slipstream cases. It is impossible to implement the wing performance into the efficiency equation this way. The overall aircraft efficiency could be expressed as the reciprocal of the propulsion efficiency, and considering that $D_{rest}$ can be assumed constant for all configurations, the equation becomes:

$$\eta' = \frac{P_{aircraft}}{T_{wing+propulsion}V} = \frac{P_{aircraft}}{D_{wing+propulsion}V} \tag{5.12}$$

Although it strictly not the correct way of defining a propulsion efficiency, it can give a good estimate on the relative performances of the uninstalled and installed cases. If, for a given power setting, the $D_{wing+propulsion}$ increases, the overall efficiency ratio decreases, which is intuitively correct also. In a case when $P = 0$, such as a all-engines-out case or a powered sailplane during the sailing phase, the aircraft efficiency also becomes zero. It must then be understood that this expression of aircraft efficiency is for powered conditions only in order to be meaningful.

## 5.3. INTERACTION CASE: FOKKER F50 WING WITH ROTORS AND ROTOR-STATOR SYSTEMS

As an example of the method described in Section 5.2, and to add to the Fokker F50 example used earlier, a F50 wing was modeled as a lifting line. Wing data of a model used by Veldhuis [34] was used, such that a comparison could be made. This wing is very close to the actual F50 wing, with the main difference being that the wing span is increased from 29 to $30m$. Further geometry details can be found in Table 5.1, and a top view image of a Fokker F50 can be seen in Figure 5.10. The entries with 'inboard up' in the table refer to the rotation direction of the rotor: if the blade pointed towards the fuselage moves up, it is said that the rotor rotates 'inboard up'. Because both F50 rotors rotate in the same direction, one rotates 'inboard up' and the other 'inboard down'. The stator design for F50 cruise conditions from Section 4.1 is used.

Just like the rotor-stator system mentioned earlier in this document, the cruise situation is assessed at an airspeed of $140m/s$ and an altitude of $7.620km$. The value for the airfoil two-dimensional lift-to-drag ratio only affects the $C_{d0}$ and $C_d$ value of the wing. This ratio has to be estimated using airfoil polar data, but is of no importance for the span efficiency, lift coefficient, and circulation distribution. As a check of the lifting line model, the $C_l$ distribution in the clean wing configuration is compared to the calculated vortex-lattice-method (VLM) values of Veldhuis, Figure 5.11, and to the solution of the open-source lifting line and panel method code XFLR5 [35]. The comparison is interesting. Both the author's lifting line method as well as XFLR5 have the same shape, but are different from Veldhuis' VLM solution. Although the two lifting line solutions have the same shape, the XFLR5 solution seems to scaled in vertical direction. It is thought that XFLR5's nonlinear lift line method uses a better approximation to the lift slope of the lifting line theory ($2\pi$). A comparison of three XFLR5 analysis methods; lifting line, panel method, and VLM, are shown

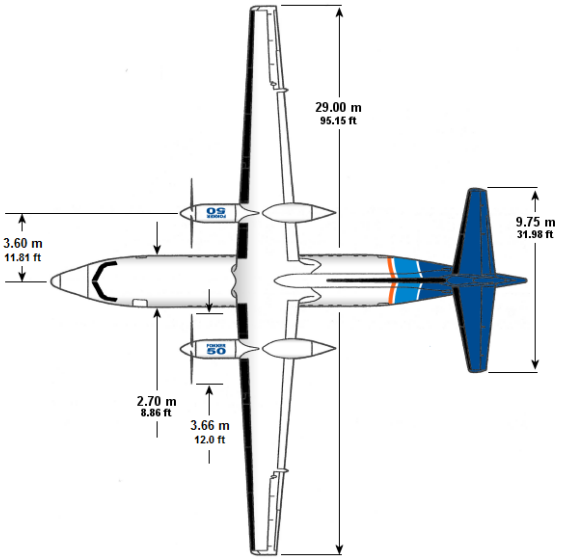


Figure 5.10: Fokker F50 top view, from the Fokker website [33]. Note the long engine nacelles, giving ample space for a stator retrofit. Rotor spanwise distance and rotor diameter added by author.

in Figure 5.12. The lifting line analsys of the author is rather consistent with the panel and VLM analyses of XFLR5, but surprisingly the lifting line analysis of XFLR5 gives slightly higher $C_l$ values. The reason is not known. The rotor-stator slipstream is assumed to have a constant radii downstream, and it is therefore implied that the engine nacelle is found within this hub radius. As can be seen from Figure 3.6, the F50 engine nacelle is indeed slim and apart from the cooling inlet at the bottom of the nacelle, the approximation is deemed valid for this particular aircraft.

**F50 output**

The full lifting line routine output of the F50 wing and rotor slipstream model consists of a `*.txt` file with all relevant wing, rotor slipstream, and system slipstream data, which are displayed here in Table 5.2. It is immediately clear that the span efficiency of the uninstalled clean wing is the best of the three cases; which should come as no surprise. The wing efficiency of the rotor installed case is more than 10% lower than that of the clean wing, because of disturbances in the circulation which causes excessive induced drag. This is also seen in the graphs below. The rotor-stator system case already shows a large improvement in wing span efficiency, in fact, it is quite close to the clean wing case with a difference of about 3%. The disturbances in the circulation distribution are smaller too. Because the F50 has two rotors rotating in the same direction, the slipstream distributions over the wing are not symmetrical along the wing centerline. This means that a nonzero rolling moment is present. That the rotor-stator system has effectively removed a lot of swirl is proven from the fact that the rolling moment for that case is about 3.4 times less than the first case. The highest wing 3D L/D ratio cannot be found at the clean wing case, but is found at the rotor-stator system case. The wing pitch angle has to be changed in order to have equal lift for all three cases. This influences the overall $C_l$ and $C_d$ values. Although the span efficiency is larger for the clean wing case, the increase in $\alpha$ causes the total drag to be slightly higher than the rotor-stator system case.

To obtain the aircraft efficiency as defined in Equation 5.12 for the two installed cases it

Table 5.1: Table containing wing and slipstream geometry and analysis parameters from the F50 wing model, based on the model used by Veldhuis [34].

| **Parameter** | **Value** | **Unit** |
|---|---|---|
| $V_\infty$ | 140.0 | $[m/s]$ |
| $\rho$ | 0.5499 | $[kg/m^3]$ |
| $b$ | 30.00 | $[m]$ |
| $S$ | 72.45 | $[m^2]$ |
| $AR$ | 12.42 | $[-]$ |
| Kink position | 7.5 | $[m]$ |
| Chord, root | 3.46 | $[m]$ |
| Chord, kink | 2.415 | $[m]$ |
| Chord, tip | 1.37 | $[m]$ |
| $\alpha$, root | 3.27 | $[m]$ |
| $\alpha$, kink | 2.27 | $[m]$ |
| $\alpha$, tip | 1.27 | $[m]$ |
| Airfoil, root | NACA $64_2421$ | $[-]$ |
| Airfoil, kink | NACA $64_2418$ | $[-]$ |
| Airfoil, tip | NACA $64_2415$ | $[-]$ |
| Airfoil L/D (2D) estimate | 120 | $[-]$ |
| Slipstream radius | 1.7362 | $[m]$ |
| Slipstream hub radius | 0.2996 | $[m]$ |
| Spanwise location rotation axis | 3.75 | $[m]$ |
| Left rotor rotation inboard up | no | $[-]$ |
| Right rotor rotation inboard up | yes | $[-]$ |

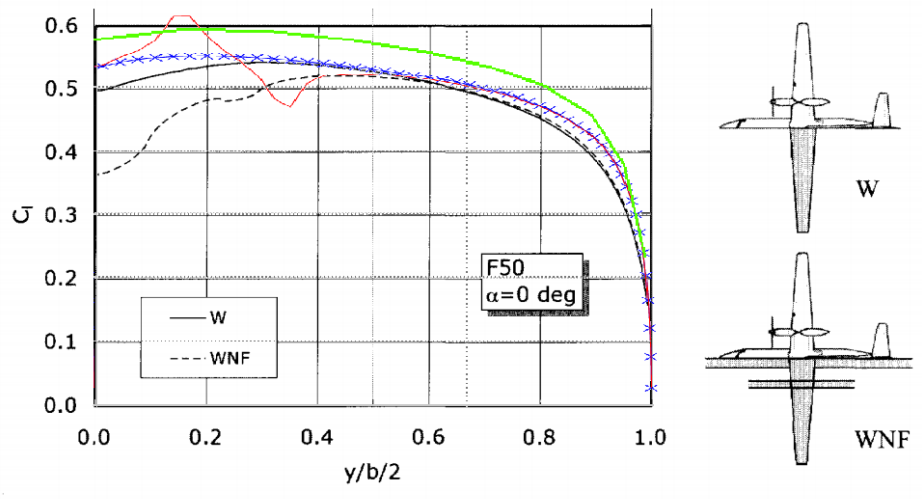


Figure 6.15: *Lift distributions predicted with VLM for the clean wing (W) and the wing-nacelle-fuselage (WNF) configuration ; Fokker 50 model at $\alpha = 0°$ ; props off.*

Figure 5.11: Comparison of lift coefficient distribution for the lifting line wing with calculated data from Veldhuis [34]. The blue line indicates the uninstalled F50 wing lifting line output, and should be compared to the solid black curve. It seems that the lifting line slightly over-predicts the $C_l$ distribution, which might be caused by the fact that the lift slope is exactly $2\pi$ in the mathematical model, and slightly smaller in the actual airfoil polar and VLM method.

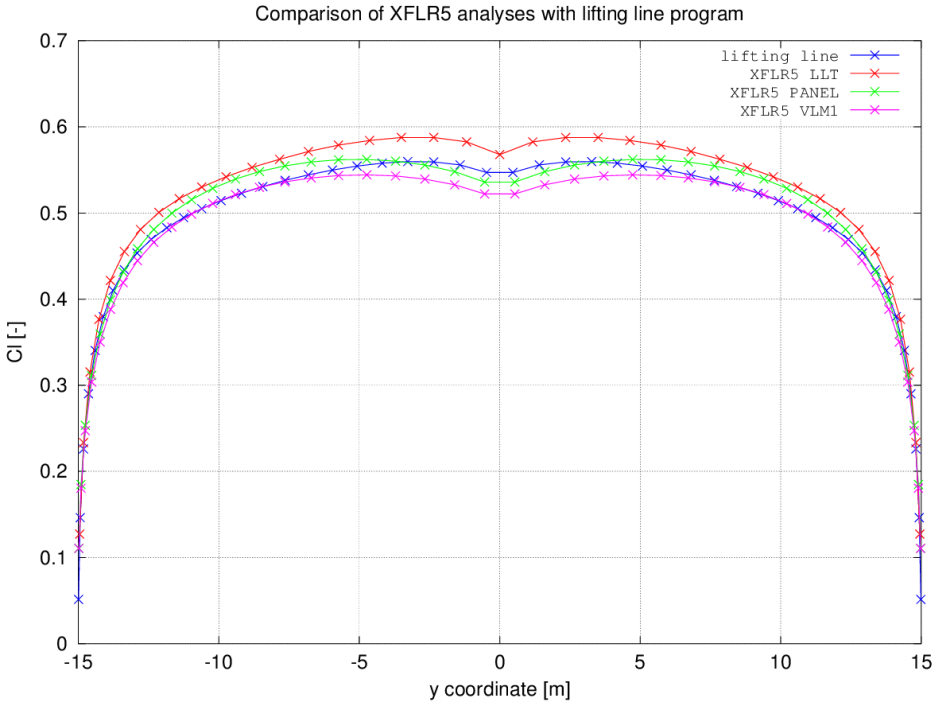


Figure 5.12: Comparison of lift coefficient distribution for the lifting line wing with XFLR5's lifting line, panel, and VLM methods.

is necessary to first obtain $D_{rest}$. The uninstalled case is used to estimate $D_{rest}$:

$$\begin{aligned} D_{rest} &= \frac{P}{V} - D_{wing,uninstalled} \\ &= \frac{2 * 1225\text{E}3}{140} - 4524 \\ &= 12976[N] \end{aligned} \tag{5.13}$$

The aircraft efficiencies are then calculated and are related to the uninstalled case which has an efficiency of exactly 1:

$$\begin{aligned} \eta'_{rotors\ installed} &= \frac{2 * 1225\text{E}3}{(4983 + 12976) * 140} \\ &= 0.9744 \end{aligned} \tag{5.14}$$

$$\begin{aligned} \eta'_{systems\ installed} &= \frac{2 * 1225\text{E}3}{(4516 + 12976) * 140} \\ &= 1.0005 \end{aligned} \tag{5.15}$$

The differences are small, and it can be seen that the systems installed case has an aircraft efficiency larger than 1. Note that this is possible as it is not a true efficiency value, but a comparison with the uninstalled case as baseline.

The systems installed case has an improvement of 10.34% over the rotors installed case in cruise conditions. It is clear that by adding SRVS to rotors the overall aircraft efficiency significantly increases.

Table 5.2: Table containing analysis results for the three cases for the Fokker F50.

| **Parameter** | **Value, Case 1** | **Value, Case 2** | **Value, Case 3** | **Unit** |
|---|---|---|---|---|
| Wing span efficiency | 0.8279 | 0.9381 | 0.9629 | [−] |
| $C_l$ | 0.5075 | 0.5075 | 0.05216 | [−] |
| $C_{d0}$ | 0.0042 | 0.0042 | 0.0043 | [−] |
| $C_{di}$ | 0.0080 | 0.0070 | 0.0072 | [−] |
| $C_d$ | 0.0122 | 0.0113 | 0.0116 | [−] |
| Wing L/D | 41.60 | 45.05 | 45.02 | [−] |
| Wing roll moment | -29676 | -8702 | 0 | $[Nm]$ |
| Wing lift | 203507 | 203457 | 203646 | $[N]$ |
| Wing drag | 4893 | 4516 | 4524 | $[N]$ |

Figure 5.13 shows a top-view of the wing planform in $[m]$, with the rotor or system slipstream boundaries drawn as lines. It gives a simple overview of the chord distribution, and the kink geometry (if present).

Figure 5.14 shows for all three cases the final spanwise distributions of angle of attack $\alpha$ and induced angle of attack $\alpha_i$. The zero-lift angle of attack distribution $\alpha_0$ which is constant for all three cases, is given too. Again the rotor and system slipstream edges are displayed as vertical lines.

The next plot, Figure 5.15, shows the spanwise $C_l$ distribution for all three cases. Figure 5.16 shows all nondimensional circulation distributions. Slipstream edges again made

visible by vertical lines. The effect of the slipstreams on the distributions can clearly be seen; for each slipstream a 'tilted S' shape is introduced in the circulation, creating more induced drag.

Figures 5.17 and 5.18 show the lift coefficient and circulation distributions in a 3D-view of the rotors installed case. Note that the distributions do not have a scale but are for illustration only. The system slipstreams are shown as a wireframe tubes intersecting the wing.

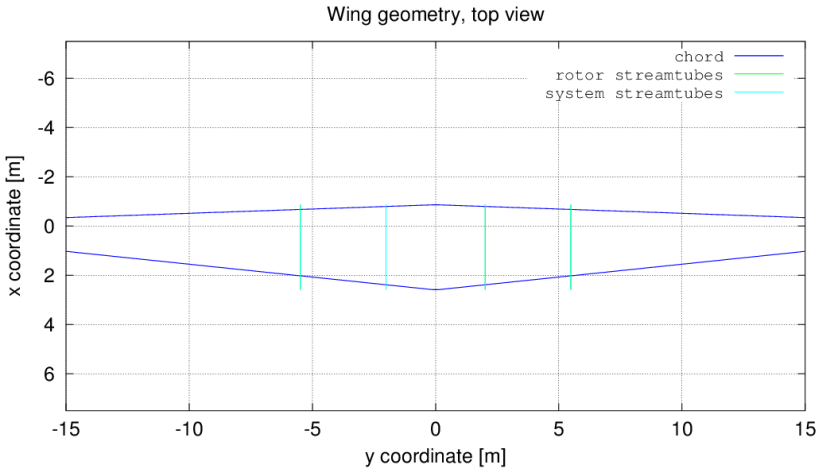


Figure 5.13: Geometry (top view) of a Fokker F50 wing, used as input for the lifting line model. Rotor-stator system slipstream edges are shown as cyan and green lines. Since a wing half is modeled as a single trapezoidal shape, no kink can be seen in either LE or TE for this particular wing geometry.

**Remarks on the model**

When the rotors or rotor-stator systems are 'switched on', the axial velocity increase effectively increases the total lift of the wing. An iteration routine was added to the model such that the angle of attack distribution is decreased in steps until the difference in total lift is below a certain very small treshold. Ideally the difference goes to zero such that all cases have equal lift, which is needed for a fair comparison of aerodynamic properties. Figure 5.14 shows that this change in angle of attack is quite small; $< 0.1°$. It also shows the induced angle of attack distributions which also show this behavior, but with a larger difference due to their dependency on the circulation and not just the geometry of the wing. Based on the angle of attack difference due to tangential velocities in the slipstream, a rather large change in $C_l$ would be expected. As can be seen from the induced angle of attack, the actual angles as seen by the wing are smaller and as such the difference in $C_l$ is smaller too. Figure 5.15 confirms this. Figure 5.16 clearly shows that the non-dimensional circulation distribution is practically the same for both cases, except around and behind the rotor slipstream locations. The larger changes in circulation for the in-

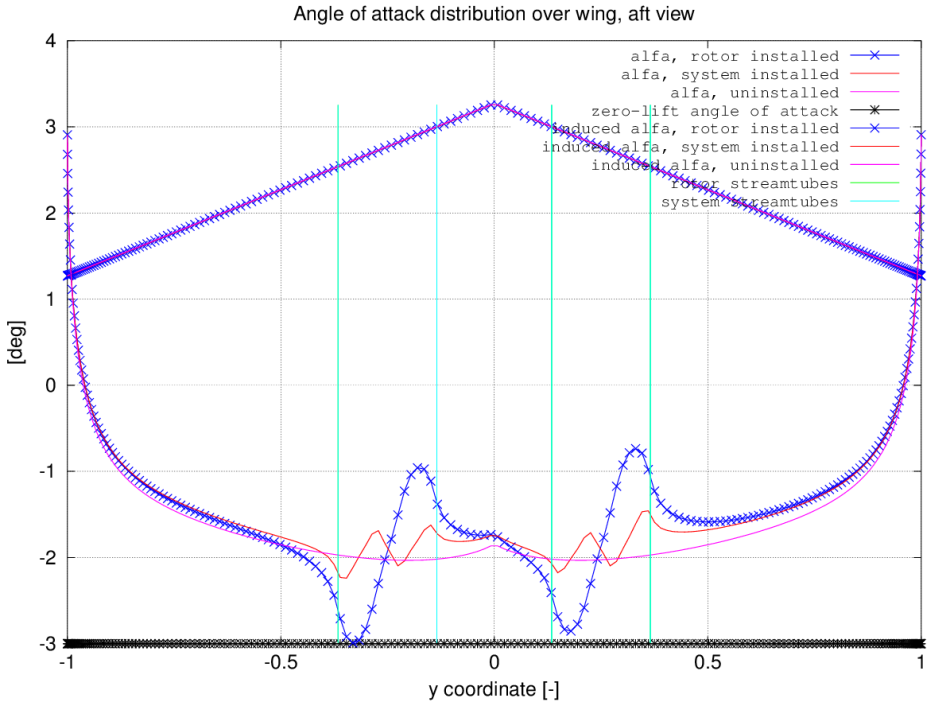


Figure 5.14: Lifting line model of Fokker F50 at cruise condition. Shown are the spanwise distributions of angle of attack and zero-lift angle of attack, all calculated using 200 nodes with cosine spacing. The vertical cyan lines show the boundaries of the slipstream tubes of both rotors. The zero-lift angle of attack (black) here is seems constant at $-3°$, but this might differ for other geometries or airfoils.

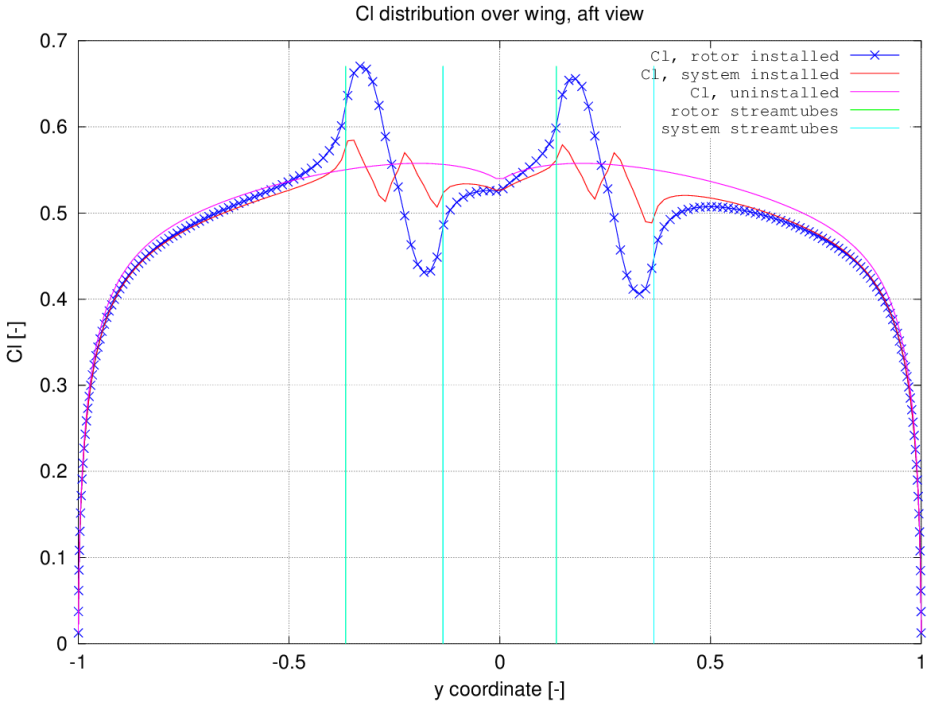


Figure 5.15: Lifting line model of Fokker F50 wing at cruise condition. Shown are the spanwise lift coefficient distributions for uninstalled and installed conditions, all calculated using 200 nodes with cosine spacing. The vertical cyan lines show the boundaries of the slipstream tubes of both rotors. The slight dip of $C_l$ near the wing center is caused by the geometry created by joining two trapezoidal wings. It is present in all three conditions.

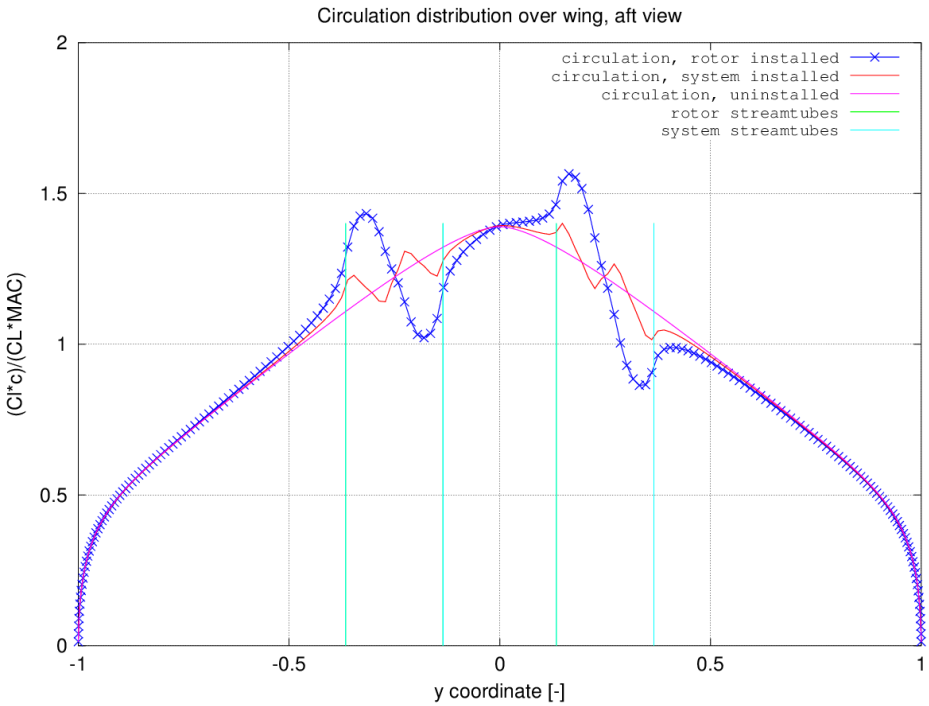


Figure 5.16: Lifting line model of Fokker F50 wing at cruise condition. Shown are the spanwise circulation distributions for uninstalled and installed conditions, all calculated using 200 nodes with cosine spacing. On the vertical axis the circulation strength is made nondimensional parameter to be able to compare all three conditions. The vertical cyan lines show the boundaries of the slipstream tubes of both rotors. It is clear any installed system creates large changes in circulation, therefore increasing induced drag.

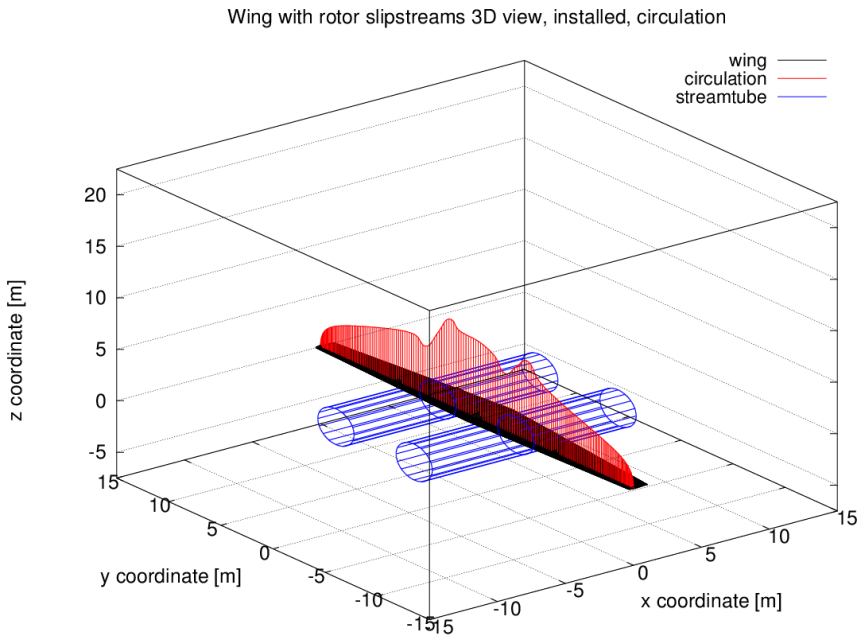


Figure 5.17: 3D-representation of lifting line model of Fokker F50 wing at cruise condition, rotors installed. Shown are the circulation distribution, calculated with 200 nodes at cosine spacing, the wing and the rotor streamtubes. Streamtube diameter here is equal to the diameter as seen by the wing.

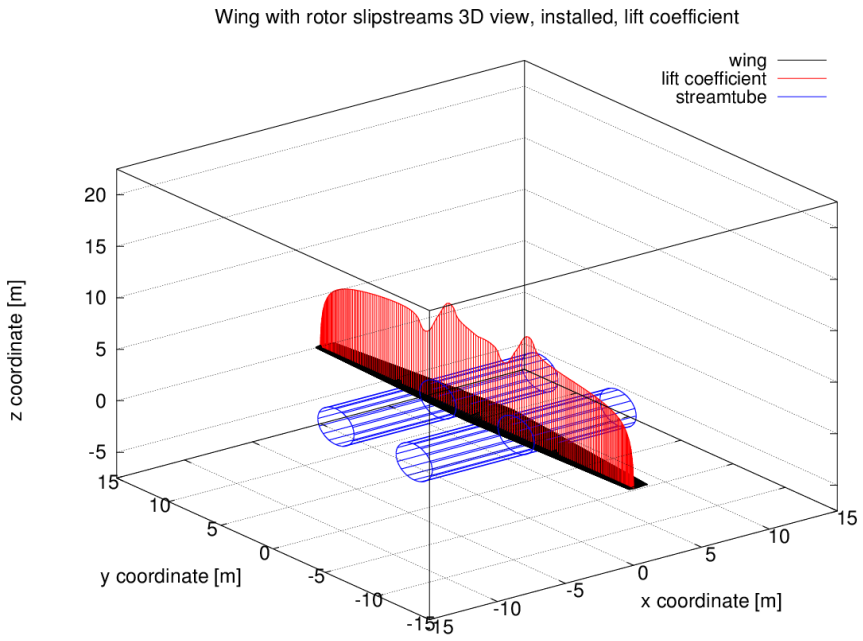


Figure 5.18: 3D-representation of lifting line model of Fokker F50 wing at cruise condition, rotors installed. Shown are the lift coefficient distribution, calculated with 200 nodes at cosine spacing, the wing and the rotor streamtubes. Streamtube diameter here is equal to the diameter as seen by the wing.

stalled case creates more vorticity which increases the induced drag of the wing, reducing span efficiency. It might very well be that an increase in propulsion efficiency due to use of a stator is completely negated by the decrease in span efficiency. If both rotors have the same rotational direction, the tangential slipstream creates an asymmetrical lift distribution over the wing, leading to a roll moment. The Fokker F50 aircraft is an example of that, where the left rotor is 'inboard down' and the right rotor 'inboard up', referring to the blade movement when it is pointing at the fuselage. Regarding the aircraft controls, the stator torques should be added to the wing roll moment. This is not done for two reasons; the main reason being that the aerodynamic effects on the wing are here analysed separately. The other reason is that the value for the Fokker F50 with stator torque is still substantially below the stand-alone rotor torque, with a value of $M = -8702 - (5050 * 2) = -18802[Nm]$ versus $M = -29676[Nm]$.

Regarding the assumed equilibrium of forces, the increased thrust of the rotor-stator system means that the aircraft is no longer in equilibrium: the thrust is now larger than the drag. Either the aircraft will speed up (increased $V_\infty$), or will start to ascend ($L > W$) at the original $V_\infty$. In the first case, the new airspeed means that the rotor-stator system is not working at the design airspeed. A large iterative procedure should be used to converge the rotor-stator system design and aircraft design to both be optimized for the design $V_\infty$, such that the forces are in equilibrium again. The relatively small difference in performance between the rotor-only and rotor-stator system cases (respectively Case 1 and Case 2) show that for a first conceptual analysis, overlooking the relatively small thrust increase can be justified as the ideal final rotor-stator system design (with forces in equilibrium again) is likely to be very close to the currently analyzed design.

# 6

# CONCLUSIONS AND RECOMMENDATIONS

## 6.1. CONCLUSIONS

**Slipstream contraction and modeling**

Various theoretical models regarding rotor slipstreams, such as actuator disk theory and even more elaborate models ([31]), show an equal contraction of the flow before it enters the rotor and after it exits the rotor plane. Experimental data from literature shows that the contraction mainly takes place in front of the rotor, and that any contraction behind the rotor is small and reaches steady-state (constant slipstream tube radius) rather quickly. Experimental data from the APIAN programme showed that slipstream contraction was small and had a quite constant radius downstream. These results made clear that rotor-stator spacing as a variable would have negligible effect on performance, since the rotor slipstream could easily be assumed equal for the axial distances at which a typical stator would be mounted (half the rotor radius or larger). Concerning the stator, the increase in axial velocity imparted by the stator is generally so small that it is safe to assume that the stator slipstream does not experience any contraction. While it seems counterintuitive that a thrust-producing stator has no slipstream contraction (this goes against actuator disk theory, for example), the thrust here is a byproduct of the tangential forces only.

**Airfoil data and analysis**

A blade element method needs airfoil performance parameters for each section. As each section is assigned a 2D airfoil, the values for $C_l$ and $C_d$ can be readily be estimated using existing airfoil analysis methods, or read in from existing airfoil polars. For high rotor tip speeds or high flying speed in general, airfoil analysis methods suited for high subsonic speed or appropriate compressibility correction methods should be used after airfoil analysis to account for transonic effects, especially beyond the drag divergence Mach number. In XROTOR it is possible to define a number of airfoil sections at different radial positions along the blade. Instead of using direct airfoil polar values, it uses aerodynamic parameters to create a model of the airfoil aerodynamic behavior by using linear $C_l$ versus $\alpha$ and parabolic $C_d$ versus $\alpha$ relations for attached flow conditions and a different model to mimic stall behavior. The user specifies this airfoil behavior at a given *Re*, and XROTOR takes care of appropriate airfoil polar scaling when the analysis *Re* is different. Clearly, this method is an approximation at best of actual airfoil behavior, especially at low *Re*. XROTOR also uses a compressibility correction for high subsonic speeds. It is strange that the excellent

airfoil analysis tool XFOIL, created by the same person, is not coupled or incorporated into XROTOR. Robustness of the XROTOR analysis at or near blade section stall with the more simple method might be one of the possible reasons for this.

Concerning the APIAN rotor, airfoil sections were not available and at best the camber line and chord could be inferred from a 3D CAD model. It was already apparent from the very thin airfoil sections that XFOIL could have difficulties converging to a solution, as turned out to be the case. No accurate airfoil data was obtained from either the 3D CAD model or XFOIL. As mentioned above, XROTOR's less than perfect but more robust airfoil analysis was used to generate a propeller model of the APIAN rotor using the XROTOR default airfoil settings.

**Rotor and stator analysis**

A BEM code which can analyze a rotor can also analyze a stator, as there are no fundamental differences between them with the stator simply being a rotor with $rpm = 0$. For low speed conditions a BEM will generally give good results. XROTOR is a BEM which is written for subsonic rotor analysis and works great, given suitable input values the program analysis and design routines will almost always converge. In exceptional cases where no convergence takes place or when questionable input values are used, it is not always possible to create slipstream output files although the program did not crash. This is the cause that the rotor-stator analysis program described in this thesis has to check for existence of said slipstream files in order to continue.

Stator analysis with XROTOR works rather well, but there are some issues which would not be expected from theory. For example, XROTOR cannot handle $rpm = 0$, and is made to model a stator by seeing it as an isolated and exceptionally slow rotating rotor. Also the way in which some performance parameters are calculated or defined, such as $\eta_{stator}$ and $J$, sometimes give strange results. Key points are here that the stator design should be reasonable and plausible, such that analysis parameters such as $J$ or $rpm$ are not too far off the design point, otherwise the analysis might not converge. The overall rotor-stator system efficiency and other performance parameters are calculated outside of XROTOR, and give correct results.

**Stator design with XROTOR MIL routine**

As described above, XROTOR's minimum induced loss (MIL) design routine works fine for rotors, but has its limits when it comes to stator design. XROTOR was simply not intended to design non-rotating devices. The obvious work-around is to trick XROTOR into designing a very slowly rotating rotor, which for all practical purposes can be regarded as non-rotating, thus a stator. Unfortunately the way the design routine is written to converge to a design seems to be the main culprit. It is possible to input a nonzero complete blade $C_L$ value, while the vector geometry ends up having zero tangential velocity. The overall blade efficiency as defined by XROTOR multiplies by this tangential velocity component, such that it is possible to have a blade which creates lift but has zero induced efficiency. This is mathematically sound in the way the method is set up, but it is physically not possible. Such a situation can only possibly exist when the blade angle is near 90°, or almost aligned with the freestream direction, which unfortunately is the case for stator blades.

In the stator design cases where XROTOR converged, the stator designs proved to be very sensitive to input conditions as power and *rpm* values. The changes in blade angle were very small, but the chord distribution would sometimes vary wildly for seemingly almost identical input conditions. Results of the F50 stator parameter sensitivity study show that for various stator chord widths the efficiency increase is roughly the same, in the order of $0.7 < \Delta\eta < 1.3\%$. Here the rotor over stator power ratio was varied while the stator *rpm* was kept constant. When changing the *rpm* ratios and keeping the power ratio constant it was found that the chord width changes even more, and that towards smaller *rpm* ratios the planform shape also starts to change to a wider blade root. Again the changes in efficiency are rather small, $0.3 < \Delta\eta < 1.1\%$.

It seems that XROTOR has trouble finding an optimum solution in some cases, and as such it is suspected that it does not find the absolute optimal solution at all. A crude simulation of a stator blade by using a simple 3-element BEM solution showed that the XROTOR design performance is in the ballpark however, thus the performance seems believable, but possibly not too accurate. Sometimes a strange twist in the very outer portion of the blade is seen, such as is the case with the APIAN stator design. It is believed that XROTOR tries to negate a finite rotor swirl component while the circulation near the stator tip goes to zero: a case which becomes impossible towards the stator blade tip. It must be concluded that the way the XROTOR MIL design routine is written is suboptimal at best, and it is hard to believe that it produces a real optimum stator design.

Various runs with different rotors or stator design input have consistently shown that when the stator is designed with the rotor operating at a higher $J$ than the actual isolated rotor $J$, and afterwards again analyzed at this (correct) isolated $J$, the graph of $\Delta\eta$ versus $J$ is basically shifted to the right, raising the efficiency over the full $J$ range. There is no clear physical reason why this should happen, although the $\Delta\eta$ versus $J$ behaviour is seen in literature as well.

**APIAN stator design**

The stator designed for the APIAN-INF wind tunnel test program was made by an earlier version of the author's rotor-stator analysis code when it was still under development. The advance ratio of the rotor was $J = 1.75$ for the stator design, and during the wind tunnel test the rotor was run at $J = 1.05, 1.40, 1.75$. Performance plots show that the expected gain in propulsion efficiency for these advance ratios is near to $\Delta\eta = 2.5, 1.6, -1.0\%$, where the earlier version of the program would not converge beyond $J = 1.65$ so the data is extrapolated from the performance plot. The $C_T$, $C_P$, and $C_Q$ values over this range of advance ratios show smooth behavior indicating that no stall occurs on either rotor or stator.

The geometry of the stator showed an almost rectangular blade, with only a slight chord increase along the middle of the radius. The blade twist distribution became a bit extreme near the blade tip and to lesser extent also the blade root. A reason for the tip twist must be sought in the combination of large rotor tangential slipstream velocities present near the stator tip, where circulation goes to zero. XROTOR's MIL routine tries to change the local blade angle by large amounts to make up for loss of circulation to counter the swirl velocities. For manufacturing reasons the design $C_L$ was not chosen too high such that

the blade chord would not become too small for milling operations on aluminum. For the same reason a NACA 0009 airfoil was used, as thinner airfoils (with almost negligible performance gain) would become too thin to manufacture accurately. The outer few $mm$ of the wing tip, and the root airfoil section of the blade were manually 'de-twisted' by a slight amount to prevent excessive blade angles as well as ease of manufacturing.

**Fokker F50 stator design and sensitivity analysis**

Propeller aircraft such as the turboprop Fokker F50 could have a longer economic life if the fuel efficiency can be improved. Adding SRVs to the rotors might be an option to do so. In order to design one or more stators, the propellers of the F50 had to be modeled in XROTOR. Geometry data was available of the XPROP rotor used in wind tunnel tests by NLR and TU Delft, which is a 1/9 scale model of the Dowty-Rotol six-bladed rotor used on the Fokker F50. Airfoil data of various sections along the blade were also available. The geometry and airfoil data were used to create a model of XPROP and a model of the F50 rotor. The comparison of XPROP $C_T$ and $C_P$ values with NLR test data shows a reasonable fit. Especially near the $J$ seen in F50 rotor cruise conditions the match is good, although this is purely coincidental. Based on the reasonable match, the F50 model was used for stator design.

Two stators were designed and four analysis cases were analyzed. First a stator was designed for the rotor in cruise conditions and one for take-off conditions.

The first analysis case dealt with both rotor and the cruise-designed stator in cruise conditions. The stator planform is plausible, although the decreasing chord size and airfoil thickness near the blade root might cause structural problems, possibly requiring manual adjustment of the geometry. The gain in propulsion efficiency is slightly under 1% at the design $J = 2.2516$. With decreasing $J$ the gain increases to 3% at $J = 1.6$. If the aircraft were to fly faster for a given rotor $rpm$, at $J = 2.375$ the efficiency gain has decreased to zero. The stator generates a torque of $Q = 5050[Nm]$.

The second analysis case dealt with both rotor and take-off-designed stator in take-off conditions, $J = 0.9971$. Although XROTOR did converge and outputted a stator design, the chord size turned out to be so immense near the wing tip, about half the stator radius, that such design can be called unfeasible from an operations point of view. Again the chord size near the wing root became very small, possibly requiring manual geometry adjustment. The performance gain, however, was still in the order of 1% around the design $J$.

The third case dealt with the cruise-designed stator in take-off conditions. Mildly surprising, the stator performed reasonably well for this off-design case, showing an increase in propulsion efficiency of 1.0% at $J = 0.9971$. It must be said that due to XROTOR's 'wiggly' analysis behavior it can be seen in the performance plots that the actual performance gain lies in the range of 0 to 1%. This means that the stator designed for cruise conditions still has a small but positive effect on the propulsion efficiency even at off-design conditions such as take-off. The stator generates a torque of $Q = 2520[Nm]$, about half of the value found for Case 1. It means that for Cases 1 and 3, which use a stator designed for cruise conditions, the stator generates the highest torque of $Q = 5050[Nm]$ at cruise conditions.

With an unfeasible stator designed in case two, it was decided not to analyze the take-off-designed stator in cruise conditions, case four, as the blade geometry was deemed unfeasible.

It seems therefore that the stator designed for the Fokker F50 in cruise conditions would give an 1.0% gain in propulsion efficiency in both cruise and take-off conditions, and could therefore be a valuable retrofit to the aircraft. Note that this behavior might not be readily copied to other aircraft propulsion configurations, as the F50 has a variable pitch propeller (take-off and cruise essentially have a different rotor). Flying a bit slower would increase the gain slightly.

**The lifting line method for slipstream-wing interference**

The lifting line method of Prandtl and Lanchester is a well-known, fast, simple, and reasonably accurate way to model the circulation distribution over a wing. The wing (or aircraft) is assumed to be in steady, symmetric and horizontal flight. The number of nodes should be high enough to model the circulation accurately enough. Especially when secondary effects such as a propulsion system slipstream come into play, the number of nodes should be high enough to capture the possibly large changes in circulation at and near the wing sections affected by the slipstream. The lifting line method is only suitable for unswept wings without dihedral. A vortex lattice method, or even a panel method would make it possible to assess other wing geometries too. The Fokker F50 wing as used as an example analysis case has a very slight dihedral and virtually no sweep, which can both be safely ignored during a conceptual analysis as shown in this thesis report.

To be able to compare different installed or uninstalled wing configurations, it was decided to use the wing lift force as a constraint, to allow the assumption of horizontal flight (lift equals weight) for all cases. An installed rotor case is used as a baseline configuration. The installed system or uninstalled case each have the pitch angle of the wing changed in order to achieve equal lift as the baseline case, and this angle change is often very small, between 0 to 0.5°.

Regarding the assumed equilibrium of forces, the increased thrust of the rotor-stator system versus the rotor only case means that the aircraft is actually no longer in equilibrium: the thrust is now larger than the drag. Either the aircraft will speed up (increased $V_\infty$), or will start to ascend ($L > W$) at the original $V_\infty$. In the first case, the new airspeed means that the rotor-stator system is not working at the design airspeed. A large iterative procedure should be used to converge the rotor-stator system design and aircraft design to both be optimized for the design $V_\infty$, such that the forces are in equilibrium again. The relatively small difference in performance between the rotor-only and rotor-stator system cases seen shows that for a first conceptual analysis overlooking the relatively small thrust increase can be justified, as the ideal final rotor-stator system design (with forces in equilibrium again) is likely to be very close to the currently analyzed design.

**Analysis of the Fokker F50 rotor-stator wing interaction**

The three cases analyzed were: a clean wing, the wing with rotors installed, and the wing with rotor-stator systems installed. The installed rotors case was was used as baseline case, as this is the configuration the Fokker F50 uses in real life. Both other cases were compared to this baseline case, with equal lift as constraint.

The span efficiency of the uninstalled clean wing is the highest of the three cases; which is no surprise, as there are no external factors affecting the circulation distribution. The increase in span efficiency of the rotor-stator system case over the rotor case is 10%. The clean wing case has a span efficiency 3% higher than the rotor-stator system case. The

spanwise circulation distributions support these results as the disturbances in the circulation are reduced too.

Because the F50 has two rotors rotating in the same direction, the slipstream distributions over the wing are not symmetrical along the wing centerline. This means that a nonzero rolling moment is present. That the rotor-stator system has effectively removed a lot of swirl is proven from the fact that the rolling moment for that case is about 3.4 times less than the first case. However, concerning the aircraft controls, the stator torques should be added to the wing roll moment. This is not done here for two reasons; the main reason being that the aerodynamic effects on the wing are here analyzed separately. The wing 3D L/D ratio, surprisingly, is not the highest for the clean wing case; the rotor-stator system case is. Keep in mind that the wing pitch angle has to be changed in order to have equal lift for all three cases. This influences the overall $C_l$ and $C_d$ values. Thus even though the span efficiency is larger for the clean wing case, the increase in $\alpha$ causes the total drag to be slightly higher than the rotor-stator system case.

**Short answers to the research sub-questions**

Some short answers are given to the research sub-questions given in Section 1.2. These questions have been answered throughout the report, but a very concise summary is given below:

- What is the effect of rotor-stator spacing on the propulsion efficiency?
  - Very small, as the slipstream contraction behind a rotor is small compared to the upstream effects. In most cases the wake is rather constant for various spacing values.
- What is the effect of rotor and stator number of blades on the propulsion efficiency?
  - More stator blades increase the propulsion efficiency, as more rotor swirl can be negated at lesser overall stator blade $C_L$. The wake behind the stator becomes more uniform also.
- Does the propulsion efficiency of rotor-stator system increase over a rotor stand-alone?
  - Yes, see below:
- How does the increase in propulsion efficiency of a rotor-stator system over a stand-alone rotor change with advance ratio?
  - A well-designed stator will generally raise the propulsion efficiency in the order of 1 to 2% at design $J$, and up to about 3 to 4% at lower $J$.
- What is the effect of rotors or rotor-stator system slipstreams on a wing mounted behind the rotors or systems?
  - It introduces disturbances in the wing circulation distribution, thereby lowering the overall span efficiency of the wing. In most cases the rotor-stator system gives less disturbance than the rotor only.

- What is the overall aircraft efficiency increase of the rotor or system installed case over an uninstalled case?
  - Both installed cases have significant less span efficiency and thus less overall aircraft efficiency than the uninstalled case. The rotor-stator system has less efficiency decrease than the rotors only case.

## 6.2. RECOMMENDATIONS

**Slipstream contraction and modeling**

As the slipstream contraction seen in real life applications is much smaller than expected from simple theoretical models, it would be wise to compile more wind tunnel data on various rotor designs at various operating conditions to create an empirical model for the slipstream contraction; both the contraction value and at which distance behind the rotor plane the slipstream radius can be assumed constant downstream.

**Airfoil data and analysis**

An improvement on the XROTOR airfoil routine would be to either incorporate airfoil analysis using XFOIL, or to extend the current method for better (stall) approximations. Another improvement might be to include 3D flow effects on $C_l$ and $C_d$ as an attempt to simulate radial flow as commonly seen in the root section of rotor blades. For propellers running with high tip speeds, and heavily loaded stator blades at high flying speed it is advisable to incorporate a good drag divergence correction into the BEM code to correctly capture transonic effects.

**Rotor and stator analysis**

Increasing the robustness of XROTOR's design and analysis routines might decrease the number of occurrences where no slipstream file can be written and the rotor-stator analysis program cannot subsequently analyze the rotor-stator performance.

**Stator design with XROTOR MIL routine**

If a stator should be designed by the XROTOR MIL routine, the author suggests that the minimum induced loss start conditions and convergence routine should be adapted such that they are more robust. No longer should the program iterate on dummy angle $\psi$, but directly on the circulation for example. It is thought that this will prevent the paradoxical case of blade sections creating finite lift while having zero induced efficiency.

**Fokker F50 stator design and sensitivity analysis**

To improve on the Fokker F50 rotor-stator analysis, it would be worthwhile to look into actual rotor advance ratios and operating conditions along the full velocity range from stand-still (take-off roll) to maximum speed, and assess the rotor-stator system performance to get a better overview of the gain by employing stators. The two analyzed cases already show that there is a benefit. Designing stators using XROTOR might not give the best results as mentioned in Section 6.1, and a better stator design routine might give even better performance increase.

**The lifting line method for slipstream-wing interference**

The lifting line method works fine and is reasonably fast. To allow for a fully equilibrium situation in all analyzed cases, a further iteration loop combining stator design, rotor-stator analysis, and wing interaction analysis could be made. Such a procedure would converge to a rotor or rotor-stator system which might fly at different $V_\infty$, but equal lift.

A further improvement could be to use a panel method, which could also incorporate secondary geometries such as engine nacelles. A CFD solution would yield even more accurate results, but very likely at a great increase in runtime. If the analysis would be extended to include the slipstream effects on wing movables such as flaps and slats, or even tail surfaces, the lifting line method is inadequate and a sufficiently detailed panel method should be used, or a VLM as intermediate step.

# BIBLIOGRAPHY


[1] M. M. Munk, *Reduction in Efficiency of Propellers due to Slipstream,* Technical Notes. No. 170. National Advisory Committee for Aeronautics (NACA) (1923).

[2] J. van Kuijk, *MSc Thesis Literature Review. The effect of design parameters on the propulsion efficiency of Swirl Recovery Vane (SRV) rotors.* Report, Delft University of Technology, the Netherlands (2014).

[3] J. H. Dittmar and D. G. Hall, *The Effect of Swirl Recovery Vanes on the Cruise Noise of an Advanced Propeller,* in *13th Aeroacoustics Conference* (1990).

[4] W. Yangang, L. Qingxi, G. Eitelberg, L. L. M. Veldhuis, and M. Kotsonis, *Report on Numerical Calculation of Swirl Recovery Vane,* Unpublished (as of November 2013) (2013).

[5] J. A. Gazzaniga and G. E. Rose, *Wind Tunnel Performance Results of Swirl Recovery Vanes as Tested with an Advanced High Speed Propeller,* in *AIAA/SAE/ASME/ASEE 28th Joint Propulsion Conference and Exhibit* (1992).

[6] C. J. Miller, *Euler Analysis of a Swirl Recovery Vane Design for Use With an Advanced Single-Rotation Propfan,* in *AIAA/SAE/ASME/ASEE 24th Joint Propulsion Conference* (1988).

[7] W. M. Benson, *Tests of a Contra-Propeller for Aircraft,* Technical Notes. No. 677. National Advisory Committee for Aeronautics (NACA) (1938).

[8] G. E. Rose and R. J. Jeracki, *Effect of Reduced Aft Diameter and Increased Blade Number on High-Speed Counterrotation Propeller Performance,* in *27th Aerospace Sciences Meeting* (1989).

[9] E. P. Lesley, *Tandem Air Propellers,* Technical Notes. No. 689. National Advisory Committee for Aeronautics (NACA) (1939).

[10] E. P. Lesley, *Experiments with a Counter-Propeller,* Technical Notes. No. 453. National Advisory Committee for Aeronautics (NACA) (1933).

[11] C. P. Coleman, *A Survey of Theoretical and Experimental Coaxial Rotor Aerodynamic Research,* NASA Technical Paper 3675, Ames Research Center (1997).

[12] D. Biermann and W. H. Gray, *Wind-tunnel tests of single- and dual-rotating pusher propellers having from three to eight blades,* NACA Wartime Report, Langley Memorial Aeronautical Laboratory (1942).

[13] D. Biermann and W. H. Gray, *Wind-Tunnel Tests of Eight-Blade Single- and Dual-Rotating Propellers in the Tractor Position,* NACA Wartime Report, Langley Memorial Aeronautical Laboratory (1941).

[14] D. Biermann and E. P. Hartman, *Wind-tunnel tests of four- and six-blade single- and dual-rotating tractor propellers,* Report No. 747, Langley Memorial Aeronautical Laboratory (1940).

[15] G. Schouten, *Theodorsen's Propeller Performance with Rollup and Swirl in the Slipstream,* J. AIRCRAFT, VOL. 36, NO. 5: ENGINEERING NOTES (1999), [Online; accessed 2014-05-21].

[16] Y. Yang, D. Ragni, L. Veldhuis, and G. Eitelberg, *PROPELLER INDUCED GROUND VORTEX,* 28TH INTERNATIONAL CONGRESS OF THE AERONAUTICAL SCIENCES (2012), [Online; accessed 2014-06-05].

[17] L. Veldhuis, TU Delft, personal communication (2014).

[18] M. Drela and H. Youngren, *XFOIL Subsonic Airfoil Development System,* http://web.mit.edu/drela/Public/web/xfoil/ (2013), [Online; accessed 2014-07-25].

[19] A. Betz, *Airscrews with minimum energy loss,* Report, Kaiser Wilhelm Institute for Flow Research (1919).

[20] S. Goldstein, *On the vortex theory of screw propellers,* in *Proceedings of the Royal Society, page 123* (1929).

[21] T. Theodorsen, *Theory of Propellers* (McGraw-Hill, New York, USA, 1948).

[22] E. E. Larrabee and S. E. French, *Minimum induced loss windmills and propellers,* in *Journal of Wind Engineering and Industrial Aerodynamics, Volume 15, pages 317-327* (1983).

[23] M. Drela, *QPROP Formulation,* http://web.mit.edu/drela/Public/web/qprop/qprop_theory.pdf (2006), [Online; accessed 2014-07-03].

[24] L. Prandtl and A. Betz, *Vier Abhandlungen zur Hydrodynamik und Aerodynamik* (Universitätsverlag Göttingen, Göttingen, Germany, 1927).

[25] *VH-FKV departing Adelaide (picture),* http://www.recreationalpilots.com.au/gallery/data/media/7/img_4554—alliance-fokker-f50—vh-fkv_filtered.jpg (2011), [Online; accessed 2014-09-22].

[26] NLR, *NLR shoptest data (no title),* (1989).

[27] R. Janssen, *Thrust forces and torque XPROP propeller and TDI model 1999A Air Turbine Motor performance,* - (2014).

[28] H. Snel, R. Houwink, and J. Bosschers, *Sectional Prediction of Lift Coefficients on Rotating Wind Turbine Blades in Stall,* ECN Report, ECN-C–93-052 (1994).

[29] DNW, *LLF,* http://www.dnw.aero/wind-tunnels/llf.aspx (2014), [Online; accessed 2014-11-10].

[30] DNW, *APIAN programme Low Speed Test (LST) and High Speed Test (HST) data,* Unpublished.

[31] W. F. Durand, *Aerodynamic Theory. A General Review of Progress. Volume IV.* (Julius Springer, Berlin, Germany, 1935).

[32] J. D. Anderson, *Fundamentals of Aerodynamics* (McGraw-Hill, New York, USA, 2007).

[33] Fokker, *Fokker F50 top view (picture),* http://www.flyfokker.com/Introduction (2014), [Online; accessed 2014-09-19].

[34] L. L. M. Veldhuis, *Propeller Wing Aerodynamic Interference*, Ph.D. thesis, Delft University of Technology (2005).

[35] A. Deperrois, *XFLR5,* http://www.xflr5.com/xflr5.htm (2012), [Online; accessed 2014-11-04].

[36] Dassault Systèmes, *Dassault Systèmes Catia,* http://www.3ds.com/products-services/catia/welcome/ (2014), [Online; accessed 2014-11-05].

[37] *LaTeX - A document preparation system,* http://latex-project.org/ (2014), [Online; accessed 2014-11-05].

[38] MathWorks, *MATLAB. The Language of Technical Computing.* http://www.mathworks.nl/products/
matlab/ (2014), [Online; accessed 2014-11-05].

[39] Microsoft, *Excel,* http://office.microsoft.com/nl-nl/excel/ (2014), [Online; accessed 2014-11-05].

[40] J. W. Eaton, *GNU Octave,* https://www.gnu.org/software/octave/ (2013), [Online; accessed 2014-11-05].

[41] M. Drela and H. Youngren, *XROTOR Download Page,* http://web.mit.edu/drela/Public/web/xrotor/ (2011), [Online; accessed 2013-11-28].

[42] B. Shoelson, *XLSAPPEND,* http://www.mathworks.com/matlabcentral/fileexchange/28600-xlsappend (2010), [Online; accessed 2014-06-10].

# A

# APPENDIX A - STRUCTURAL ANALYSIS OF STATOR BLADE FOR APIAN-INF WIND TUNNEL TEST

**Description of stator**

The stator consists of 5 identical blades which are mounted behind the APIAN propeller in the APIAN-INF wind tunnel test setup. Each blade will be connected to the support tube by a flange and 4 screws. With the chord and thickness being almost constant along the blade and a lift coefficient decreasing towards the blade tip, the largest stresses are therefore expected to happen near the root of the blade. See Figure A.1 for a 3D view of 1 blade without root flange. The airfoil is NACA 0009 over the full blade span.

**Assumptions for the analysis**

The following assumptions are made:

- Neglect torsion on blade.
- Root moment and maximum bending stress are found using XROTOR, taking into account local chord, local velocity and local lift coefficient.
- XROTOR stator analysis has taken into account APIAN rotor slipstream velocities and angles.
- Tip deflection can be found by assuming a constant distributed load (based on total lift on the blade) and a rectangular plan form. Given the lift coefficient distribution, this will actually over-predict the deflection slightly.

When the rotor is working at low advance ratios with fixed free-stream velocity, the thrust, torque and velocity increase are the highest. It is expected that the highest velocity encountered will be $V_\infty = 70 m/s$, and the lowest advance ratio will be $J = 1.05$. Two cases are analyzed; one with the highest expected load where the system is at 0° angle of attack, and one where a stator blade sees a 6° angle of attack. The latter case corresponds to a situation where the APIAN-INF rotor-stator combination is mounted 6° angle of attack, which is the highest angle of attack considered for the APIAN-INF test campaign. Because of the

asymmetric flow situation in this case, only one stator blade will see the full additional load increase that is analyzed here.

**First load case: one blade, 0° system angle of attack**

The procedure to find the lift over the blade is straightforward. See Figure A.2 for a schematic overview of a blade section. The blade as modeled in XROTOR [1] consists of 30 sections along the radius. Each section $i$ of the stator blade has a certain area $dS(i) = dr(i) * chord(i)$, where the *chord* and *dr* can be calculated from data from XROTOR's stator '*.prop' file. The local velocity as seen by the section can be found by using the free-stream velocity and the slipstream velocities of the rotor's XROTOR '*.writ' file: $V(i) = \sqrt{(V_\infty + V_{axial}(i))^2 + V_{tangential}(i)^2}$. The lift on a section is then calculated with the standard equation for lift:

$$dL(i) = \frac{1}{2}\rho V(i)^2 dS(i) C_l(i) \tag{A.1}$$

Which gives a total lift by summing:

$$L_{blade} = \sum_{i=1}^{30} dL(i) = 58.7N \tag{A.2}$$

**Bending**

Since the blade angles of the stator are very near 90° as can be seen in Figures A.4 and A.7, the assumption is made that the torque on the blade can be approximated as being equal to the lift on the blade, as both point in virtually the same direction. The drag on the blade then works in the axial direction where the full blade chord is available to counteract bending. Since the drag is so much smaller than the lift force and the chord is so much larger than the blade thickness, it is clear that the torque on the blade will be the limiting load case with respect to bending moments at the root. The equations in this section can be found in many study books on mechanics, such as Hartsuijker and Welleman [2].

The contribution of each section $i$ to the moment at the blade root can be found by multiplying the local lift $L(i)$ with the distance to the blade root; $distance(i) = radius(i) - 0.090$, where the hub radius of the stator is assumed to be $90mm$. The root moment of the total blade is then found by summing all the section moments, which for this load case becomes:

$$M_{root} = \sum_{i=1}^{30} distance(i) * dL(i) = 3.7Nm \tag{A.3}$$

The NACA 0009 airfoil has an bending moment of inertia of $I_{xx} = 1.1136E{-}10mm^4$ (data calculated from XFOIL data). The maximum stress in the blade root can be found using $\sigma_{max} = \frac{M_{root} * y}{I_{xx}}$, where $y$ is half of the blade thickness, $y = \frac{1}{2} * 0.09 * 44.38 = 1.9971mm$.

$$\sigma_{max} = \frac{2.7 * 0.0019971}{1.1136E{-}10} = 66.5MPa \tag{A.4}$$

The blades will be milled from aluminum 7075 alloy [3], which has the following material properties: a yield stress of $450MPa$, a maximum tensile strength of $530MPa$, and an elastic modulus of $E = 72GPa$.

This gives a minimum safety factor (defined as the ratio of stress over maximum tensile strength) aft the blade root of:

$$n = \frac{530}{66.5} = 8.0 \tag{A.5}$$

DNW requires a safety factor of $n \geq 4$, so it is clear that the maximum stress found on the blade root is much lower than the maximum stress allowed by DNW. It is assumed that any small deviations in the force distribution or manufacturing tolerances fall well within this safety range.

**Tip deflection**

The tip deflection can be approximated by the equation for an Euler-Bernoulli beam with one clamped and one free end, and a constant distributed load. For this part of the analysis, the blade plan form is approximated by a rectangle. The length is the distance from tip to root which is $l = 221.95-90.0 = 131.95mm$, the width is the chord width which can be taken as $c = 44.38mm$. This gives a lifting surface area of $131.95 * 44.38 = 5856mm^2$. The constant distributed load is simply the lift divided by the blade length: $q_{avg} = \frac{58.7}{0.13195} = 444.87N/m$.

For aluminum, the tip deflection (in tangential direction) is:

$$w_{tip,al} = \frac{q_{avg} * l^4}{8 * E * I_{xx}} = \frac{444.87 * 0.13195^4}{8 * 72E9 * 1.1136E-10} = 2.1mm \tag{A.6}$$

**Second load case: one blade, 6° system angle of attack**

As in the first load case, the loads are found by looking at sections of the blade from XROTOR data. With an increase in angle of attack over the full blade of $\Delta\alpha = 6°$, the new $C_l$ and $C_d$ distributions are found. Figure A.5 shows the slipstream angle of the APIAN rotor and the stator blade angle. Figure A.6 shows the accompanying lift coefficient and drag coefficient distributions over the blade. Because most of the blade is stalled, the increase in $C_l$ is not as much as expected from thin airfoil theory. This means that the actual blade loading is only a bit higher than the loading found for the first case. It is the drag that is affected the most because of stall, but the drag force is still much smaller than the lift force and it is mainly pointing parallel to the chord direction and not perpendicular. Note that with the increased angle of attack, a better approximation of the out-of-plane forces on the blade can be found by vector adding the lift and drag per section. Figure A.3 shows the geometry of this approximation.

**Bending**

Via the same procedure as the first analysis, the blade lift distribution, drag distribution, root moment, and maximum root stress are found:

$$L_{blade} = \sum_{i=1}^{30} dL(i) = 64.4N \tag{A.7}$$

$$D_{blade} = \sum_{i=1}^{30} dD(i) = 1.5N \tag{A.8}$$

$$M_{root} = \sum_{i=1}^{30} distance(i) * \sqrt{dL(i)^2 + dD(i)^2} = 4.2Nm \tag{A.9}$$

$$\sigma_{max} = \frac{2.7 * 0.0019971}{1.1136E{-}10} = 76.0MPa \tag{A.10}$$

This gives a safety factor of:

$$n = \frac{530}{76.0} = 7.0 \tag{A.11}$$

Which is still above the minimum value of $n = 4$ as required by DNW.

**Tip deflection**

The new distributed load is again the resultant of the lift and drag, and amounts to $q_{avg} = \frac{\sqrt{64.4^2+1.5^2}}{0.13195} = 488.20N/m$. The new tip deflection then becomes:

$$w_{tip,al} = \frac{q_{avg} * l^4}{8 * E * I_{xx}} = \frac{488.20 * 0.13195^4}{8 * 72E9 * 1.1136E{-}10} = 2.3mm \tag{A.12}$$

**Shear loads, blade root flange**

Each blade is secured to the support tube with 4 screws through a flange connected the the blade root. Figures A.8 and A.9 show the torque and thrust of the total stator for the first analysis case, and it is clear that even at low advance ratios the forces are reasonably small. Because blade stall limits the maximum attainable lift coefficient, the increase in thrust and torque is very small for the second analysis case, in the order of 5%. It is expected that connecting the blades with the aforementioned method should pose no problems for the forces found in the two analyzed cases.

**Bibliography**

[1] Drela, M., and Youngren, H., *XROTOR Download Page*, http://web.mit.edu/drela/Public/web/xrotor/, [Online; accessed 2013-11-28], 2011.

[2] Hartsuijker, C., and Welleman, J. W., *Engineering Mechanics, Volume 2*, Springer, Dordrecht, The Netherlands, 2007.

[3] Salomon's Metalen, *Voorraadboek van Salomon's Metalen B.V., Aluminium*, http://www.salomons-metalen.nl/images/Web-pdfs/aluminium.pdf, [Online; accessed 2014-07-31], 2014.

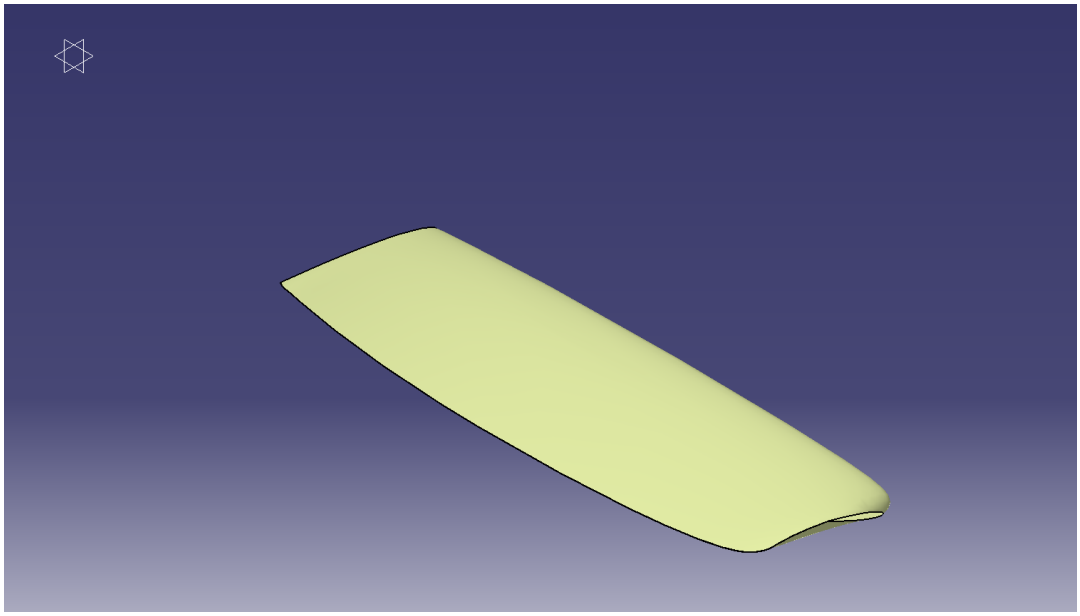

Figure A.1: 3D view of one stator blade in CATIA. The white mark in the top left corner is located on the rotation axis. Note that no root flange for connecting the blade to the supporting tube is present in this figure. Flow direction is from upper right corner to lower left corner.

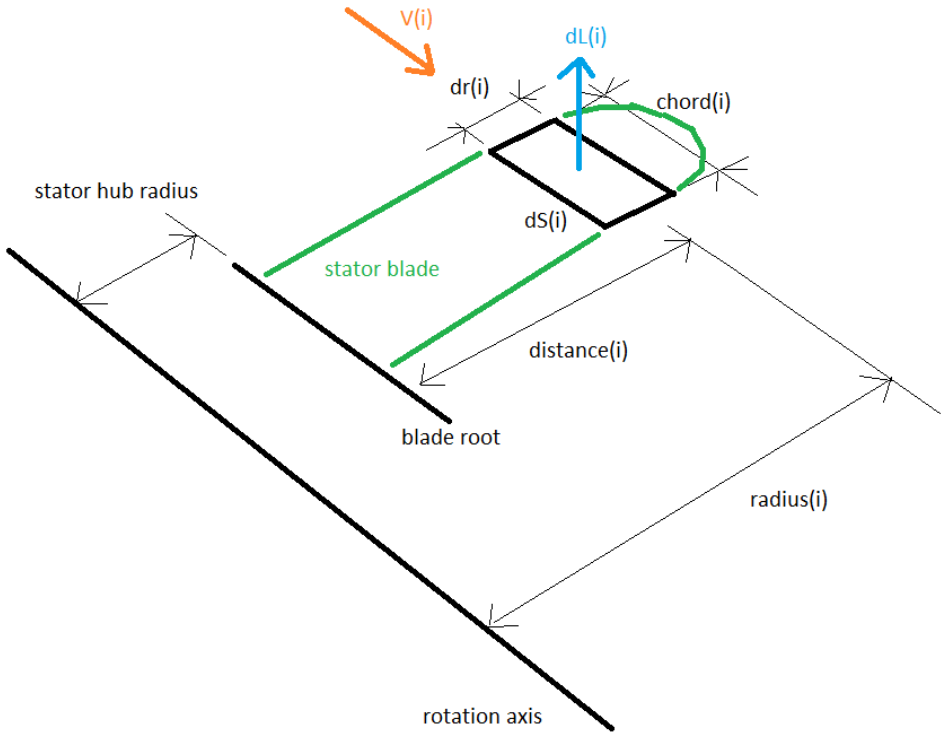


Figure A.2: Schematic view of one section of the stator blade for the 1lst analysis case with all associated dimensions, lift force and flow direction.

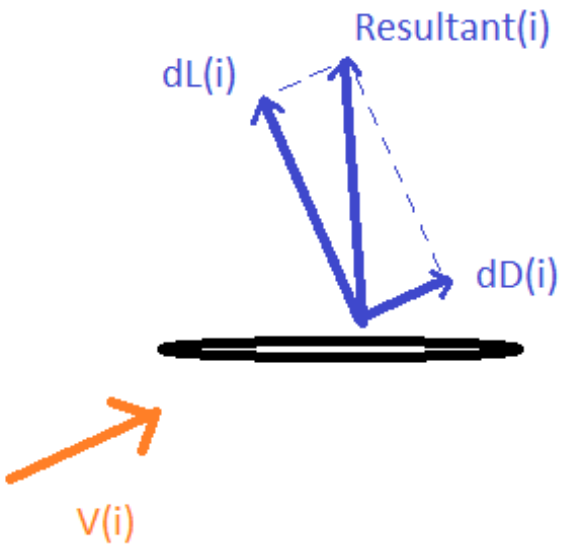


Figure A.3: Schematic view of one section of the stator blade for the 2nd analysis case with lift force, drag force, resultant, and flow direction. Note here that due to the angle of attack the drag force is included, such that the resultant force is a better approximation of the force perpendicular to the airfoil than the lift force only.

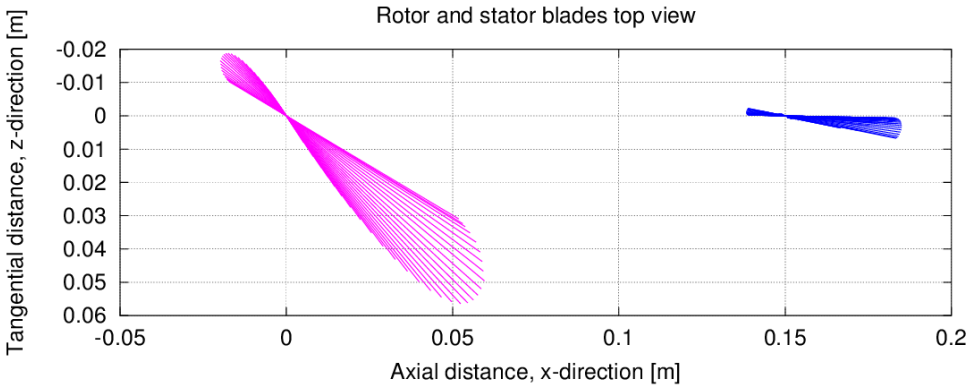


Figure A.4: Top view of APIAN rotor blade (magenta) and stator blade (blue) chord sections. Note that the stator section blade angles are nearly 90°, and that the chord length is rather constant.

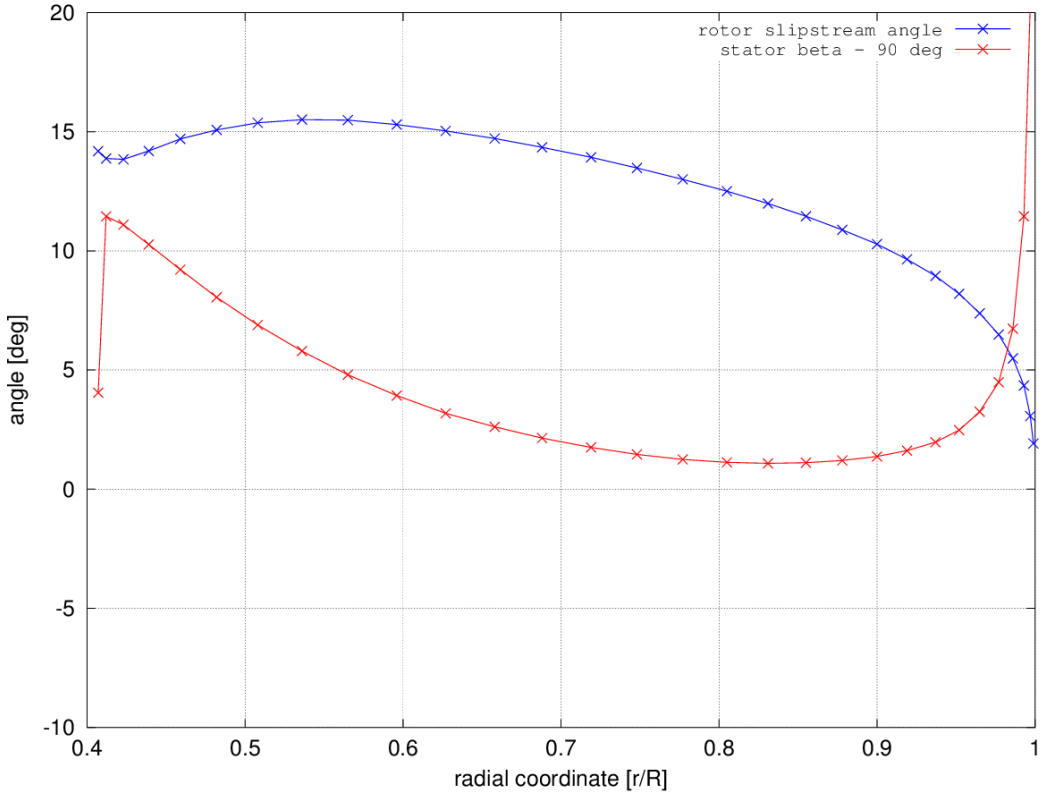


Figure A.5: Distribution of APIAN rotor slipstream angle, and stator blade angle (minus 90°). The excessive change in angles near the tip and root have been removed manually for manufacturing reasons.

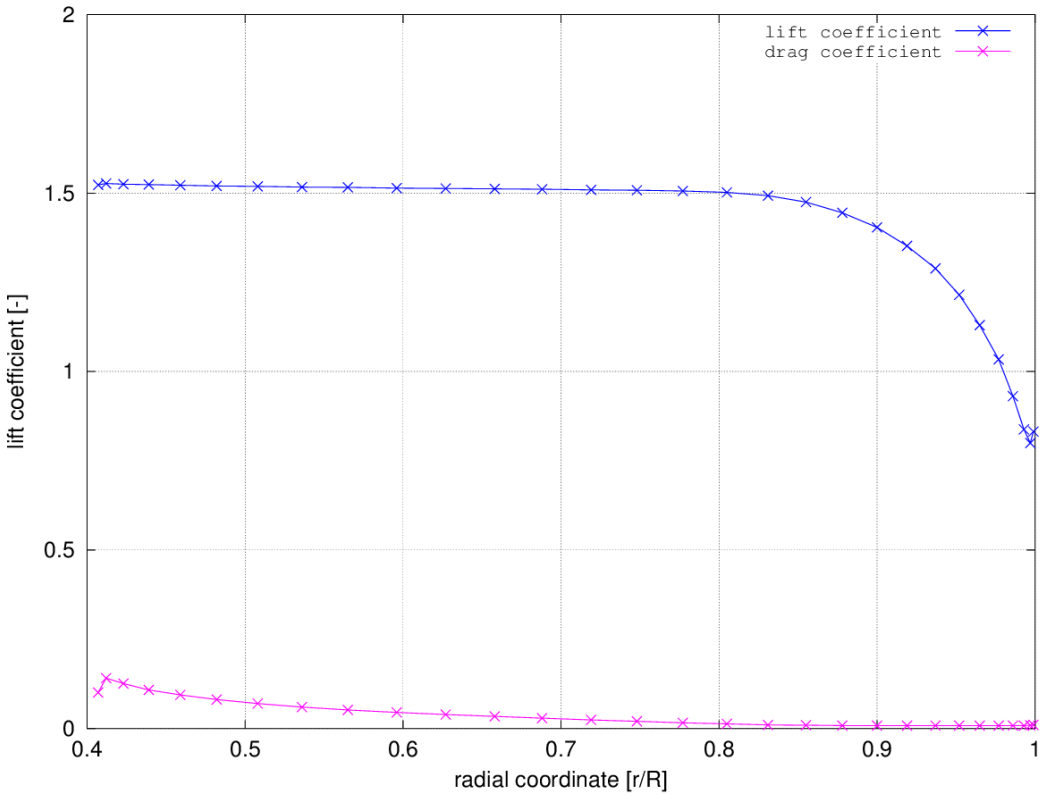


Figure A.6: The lift coefficient and drag coefficient distributions along the blade, for the 2nd analysis case. The capping effect of blade stall on the lift coefficient can clearly be seen in the range $r/R = 0.4$ to 0.8.

Figure A.7: Views of root (left) and tip (right) of stator blade in CATIA. Rotation axis is horizontal. Flow direction is left-to-right for both images.

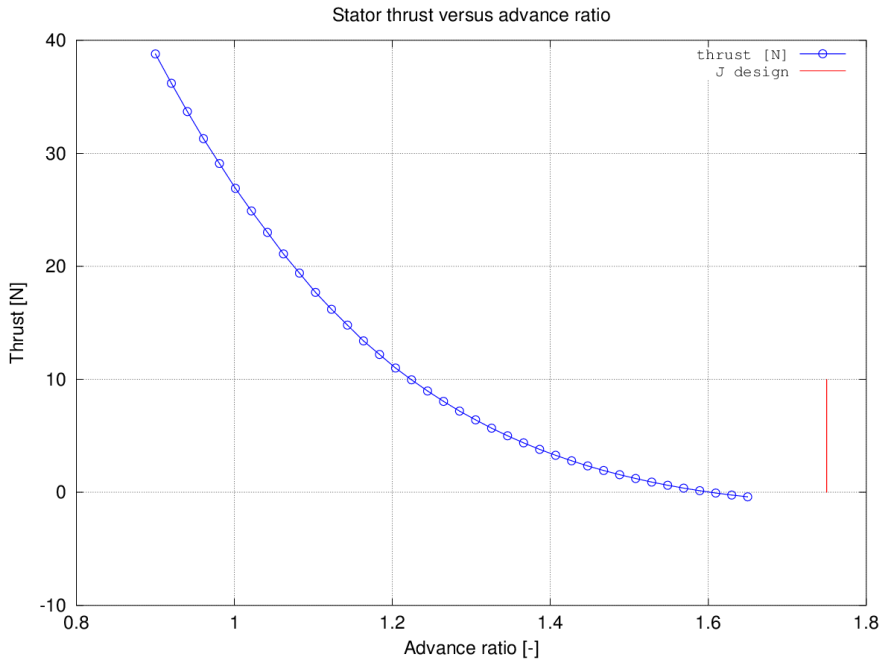


Figure A.8: Stator thrust (sum of 5 blades) versus rotor advance ratio, first analysis case. The red mark indicates the advance ratio of the rotor for which the stator was designed.

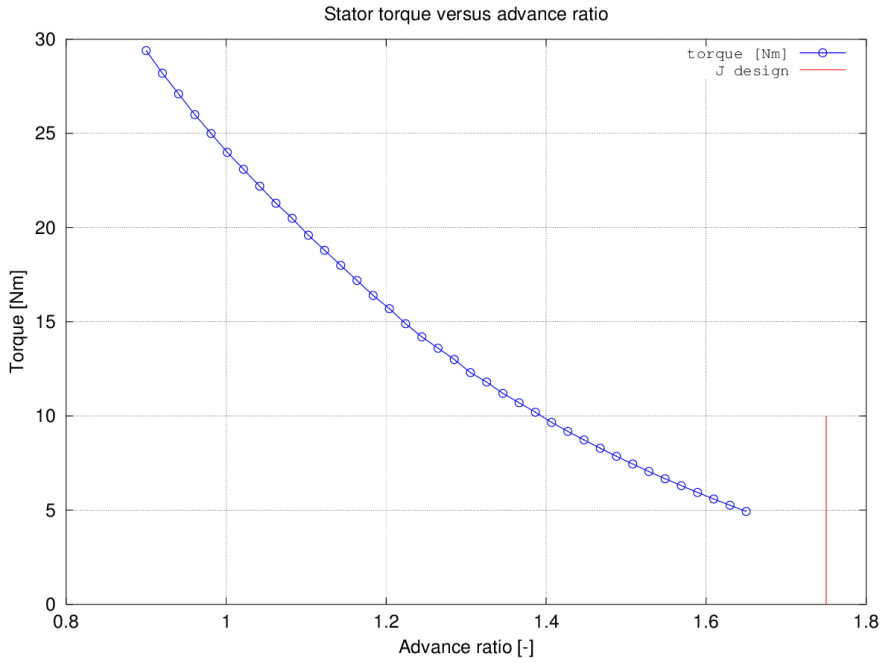


Figure A.9: Stator torque (sum of 5 blades) versus rotor advance ratio, first analysis case. The red mark indicates the advance ratio of the rotor for which the stator was designed.

# B

# APPENDIX B - SOFTWARE DESCRIPTIONS

The analyses and designing of rotors, stators, wings, and their interaction was done by various software programs. A short overview of the different programs is given below in alphabetical order. The author's code (Appendices E and F) make use of opensource codes XROTOR and XFOIL, and are written to be compatible with both MATLAB and it's unofficial opensource companion Octave. Other programs were mainly used for data processing, image generation or report writing.

**CATIA**

CATIA is a 3D CAD engineering and design program from Dassault Systèmes [36]. It is used to create 3D models of various stator blade designs.

**LaTeX**

This document was written using LaTeX [37], a great document preparation language which takes care of type-setting, picture placement, and referencing troughout the document with ease.

**MATLAB**

MATLAB [38] was needed to create '*.xls' files for generating a CATIA 3D model of the stator blades. Octave does not have an 'xlswrite' function.

**Microsoft Excel**

CATIA makes use of Microsoft Excel [39] spreadsheets which contain macros to automatically create point clouds, splines, or lofts (3D sections). Excel is part of the Microsoft Office suite.

**Octave**

The codes written by the author are written as MATLAB files for Octave [40], which is an open-source version of MATLAB and has virtually the same language. The main advantage of using Octave over MATLAB is simply that it is free to use while it can still run MATLAB files. OCTAVE might lack advanced toolboxes of MATLAB.

**XFLR5**

This is an analysis tool for wings and aircraft, using lifting line method, vortex lattic method or full panel method. It uses XFOIL to assess the 2D section aerodynamic parameters. XFLR5 was developed for designing model aircraft, and is released under the GNU General Public License. XFLR5 website: [35].

**XFOIL**

XFOIL is a 2D panel method for analysing and designing airfoils. It was created by Drela and Youngren [18] several decades ago and is still used widely today. In the author's program, XFOIL is run to analyse a given stator airfoil at a given Reynolds number. XFOIL creates an airfoil polar file as output, which is then used to curve-fit a linear lift curve and parabolic drag estimation for a certain range of $C_l$. The parameters from the curve-fit are then used as input for XROTOR's airfoil data. It is released under the GNU General Public License.

**XROTOR**

The main program used to assess rotor and stator performance is XROTOR by Drela and Youngren [41]. The program uses a command-line interface, and can analyze and design a rotor geometry using a blade element method. It has the capability of inputting a non-uniform, axi-symmetric slipstream into the rotor, and it can save the circumferentially averaged slipstream values behind the rotor. All calculations are performed by first nondimensionalizing the geometry, then analyze the rotor and then sale the geometry back. It uses 30 radial stations by default, and a maximum of 20 airfoils can be declared to simulate the rotor performance. Airfoil characteristics at radial stations are interpolated. The airfoil polar at a particular station is scaled depending the local Reynolds number, which gives polar curves such as the example seen in Figure B.1. In this thesis XROTOR is also used to design a stator. Mathematically, XROTOR cannot handle cases where $rpm = 0$ or $P = 0$. However, by desiging a very slowly rotating rotor with a low power input, placed in the slipstream of a propeller (located upstream), it is possible to 'trick' the program in designing a stator. Subsequent analysis with XROTOR uses also a very low $rpm$ setting. The code by the author defines these stator power and $rpm$ settings as ratios based on the respective rotor values:

$$powerratio = \frac{P_{rotor}}{P_{stator}} \tag{B.1}$$

$$rpmratio,analysis = \frac{rpm_{rotor}}{rpm_{stator}} \tag{B.2}$$

$$rpmratio,design = \frac{rpm_{rotor}}{rpm_{stator}} \tag{B.3}$$

Input for the stator airfoils is given by curve-fitting data from XFOIL. Like XFOIL, it is released under the GNU General Public License.

XROTOR can use three different methods to calculate the induced velocities and losses on a blade, see the list below. A blade is modeled as a lifting line in all three methods. It is assumed that the disk loading is relatively low, such that the wake contraction and wake deformation are small. The Graded Momenum Formulation is XROTOR's default setting.

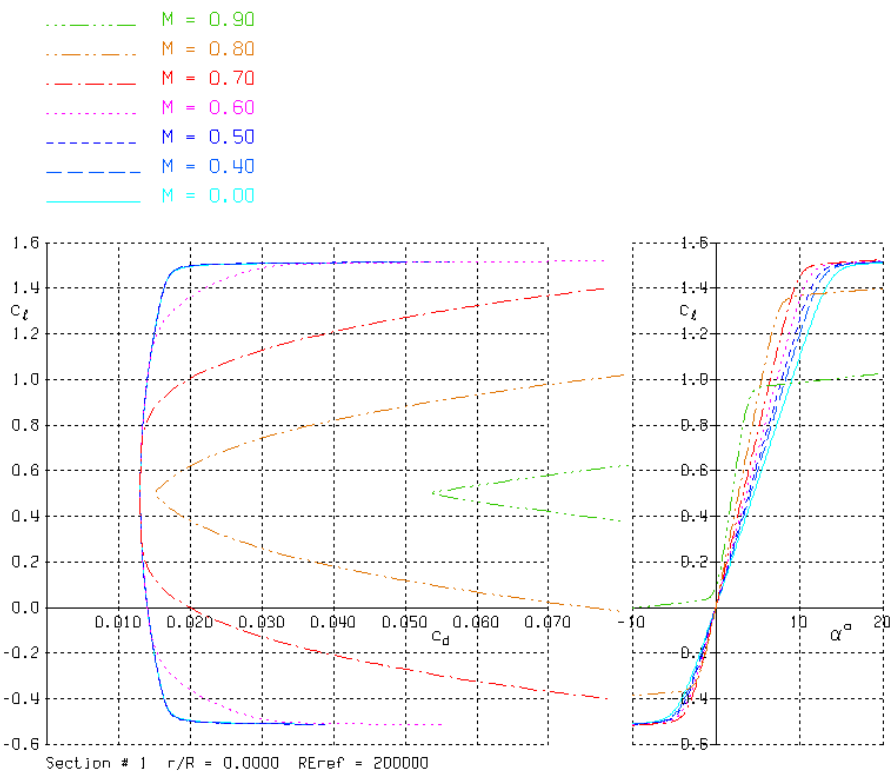


Figure B.1: Polars of the default XROTOR airfoil as found in the AERO menu. A scaling law scales a polar for a given *Re* (here denoted 'REref') to the correct *Re* and speed as seen by a blade section.

Each next method is slower in computation but gives more accurate results. The Vortex Formulation can also handle swept or raked rotors, but this is not implemented in the current version of XROTOR.

- Graded Momentum Formulation. A rather simple and very fast model, improved on by Larrabee [22]. It includes Betz-Prandtl tip loss factor, which in itself assumes a rotor with many blades and/or a low advance ratio. Therefore it is not suitable for high advance ratios.

- Potential Formulation. Assesses a potential flow about a rigid helicoidal wake. Therefore it can handle all advance ratios and blade numbers, based on Goldstein's 2- and 4-blade solutions [20]. It can treat finite hubs and nacelles, thus the Betz-Prandtl factor is not needed. It can accept a ducted configuration, which is not used in this report. It is more computationally expensive than the Graded Momentum Formulation.

- Vortex Formulation. A discrete vortex wake for induced velocity calculations. It can handle rotors with non-radial lifting lines, meaning raked or swept blades. The velocities on the lifting line are modeled using discrete trailing vortices on the helicoidal wake. Swept blade geometry is not used in XROTOR. The method is slower than the other two mentioned above. Note that the wake trails at a different advance ratio than the rotor advance ratio.

A note of caution; sometimes the advanced methods do not want to converge near limit conditions, whereas the Graded Momentum Formulation might still work. A limit condition could be negative lift or stall for example. Although non-convergence does not necessarily mean that the solution has 'blown up', it generally prevents the output of a `*.vput` slipstream file (especially true for stator designs). The rotor-stator analysis program needs these slipstream files for the full system to converge and sometimes needs a simpeler method in order to have convergence.

Also note that in general, XROTOR's advance ratio $J_{xrotor}$ is not equal to the advance ratio normally denoted by $J$. Here the advance ratio is different from $J$ by a factor of $\pi$:

$$J_{xrotor} = \frac{V}{\pi n D} \tag{B.4}$$

$$J = \frac{V}{nD} \tag{B.5}$$

In this document, $J_{xrotor}$ and $J$ are used interchangeably, and always denote $J$ as seen in Equation B.5. The conversion for XROTOR is taken care of in the rotor-stator design and analysis routine.

It is possible to analyze the performance of counter rotation and SRV rotors by manually iterating back and forth between the rotors. XROTOR has the capability of saving the circumferentially averaged slipstream velocity profile (axial and tangential) to a data file; `*.vput`. An example: a rotor is created, which sees a uniform undisturbed inflow by default: the axial velocity is constant and the tangential velocity is zero everywhere. This rotor then creates a slipstream, defined as an increase in axial component and a tangential componenent for each radial station. A second rotor (or stator) is placed behind the first rotor, and is given the first rotor's slipstream as input. The axial slipstream velocity distribution is added to the freestream velocity, and the tangential slipstream component is taken 'as-is', since the freestream has no swirl. This second rotor now is influenced by the upstream first rotor, and it will also create a slipstream itself. By assuming that the rotors are placed close together (about < 1 radius) such that the upstream rotor also feels the influence of the downstream rotor, the same procedure can also be applied to the upstream rotor. By iterating back-and-forth and updating the rotor performance of each rotor using the new slipstream velocities, the system will converge to a point where the rotor performances and their slipstream velocities can be assumed constant.

The slipstream velocities calculated by XROTOR are the far-wake, circumferentially averaged values. At the rotor disk itself these velocities are half of the far-wake values, as explained by the actuator disk theory in Section 2.1. XROTOR assumes that with a reasonably small rotor spacing, the axial velocity increase 'felt' by the other rotor has not changed yet: it is still half the far-wake value. In the same way the tangential velocity increase is either fully felt downstream (full downwash of forward rotor needs to be counteracted by downstream rotor) and not felt upstream (only upwash of downstream rotor felt by upstream rotor). Axial and tangential velocity weighting factors or 'velocity weights' are used to tell XROTOR to which extend each rotor is influencing the other rotor.

According to XROTOR's manual, appropriate velocity weights used for the effect of rotor on stator and vice versa are:

- Rotor on stator: axial velocity weight: 0.5

- Rotor on stator: tangential velocity weight: -1.0
- Stator on rotor: axial velocity weight: 0.5
- Stator on rotor: tangential velocity weight: 0

# C

# APPENDIX C - ROUTINES ROTOR-STATOR SYSTEM ANALYSIS PROGRAM

This chapter explains each routine of the rotor-stator analysis program. Two flowcharts of the two most important routines are shown at the end of the chapter. Figure C.4 shows the flowchart of `main.m`, and Figure C.5 shows the flowchart of the main analysis routine `advanceratioanalysis.m`. The files below are presented in alphabetical order. A short note on the slipstream scaling by the program is given at the end.

**`advanceratioanalysis.m`**

This is the core file of the program. It contains a loop which analyzes the rotor, stator, and system performance for each specified advance ratio. First the rotor slipstream scaling ratio is calculated by `slipstreamscaling.m`, this happens once, outside the main loop. Then the loop is started. The stand-alone rotor is analyzed with `rotoranalysisstandalone.m` to get reference data to later compare the system performance by. Inside the main loop a convergence loop is started, which will continuously assess the influence of rotor on stator and vice versa until the calculated change in system efficiency is below a user-specified threshold. This convergence loop runs `rotoranalysis.m`, `rotorvputscaling.m`, `statoranalysis.m`, `statorvputscalingback.m`, and `statorvputscaling.m` for all the analyses and appropriate slipstream scaling. See also near the end of this Appendix. After each analysis run the existence of a `*.vput` file is checked; if nonexistent, XROTOR is assumed to have analysis issues itself and this advance ratio is skipped. The system slipstream is created by calling `createsystemslipstream.m`, and the system performance is found using `systemperformancecalc.m`. When the convergence loop has finished, `convergenceplot.m` is called to plot the convergence history for that particular advance ratio. When the main loop has finished, the system performance values are written to a data file called `output.txt`. Various geometry and performance plots are created by calling subroutines `plotting.m` and `plottingvput.m`, and if the user has enabled the CATIA coordinate toggle, subroutine `pointclouds.m` is run.

**`copyfiles.m`**

This file makes sure all output files are copied to either the case or sweep analysis folder for storage.

**createstator.m**

This file sets up all parameters for the actual XFOIL MIL design routine. It reads in rotor geometry data such as the number of blades and radii. It calls subroutine `slipstreamscaling.m` to calculate the effective slipstream contraction ratio by taking into account the rotor hub radius, and the 'statorslipscaleratioequalhub' ratio. Stator radii are calculated from the rotor radii by scaling by appropriate values. The routine then calls `rotoronlyvputscaling.m`, which will scale the rotor slipstream data down to the new slipstream radius. The stator *rpm* and power are calculated using the appropriate scaling factors, and finally routine `createstatormilxfoil.m` is called to design the actual stator.

**createstatormilxfoil.m**

This routine reads in the XFOIL data file created by `xfoil_data.txt`, and writes an input file for XROTOR: `xrotor_statormil.txt`. It then runs XROTOR MIL routine which will create the stator; `<statorname>.prop`, which is stored in folder `/stator`. The XROTOR velocity weights for the influence of the rotor slipstream on the stator are 0.5 for axial slipstream components, and $-1.0$ for the tangential components as suggested by the program's manual.

**createstatorsimple.m**

This routine is similar to `createstatormil.m` with regard to the slipstream scaling. It will however model a stator by assuming a constant chord and a constant angle of attack, which are user input values. The rotor slipstream velocities are read in to calculate angle $\phi$ along the blade, and the local $\beta$ is found using the following relation: $\beta = \phi + \alpha$. With these two radial distributions; $c$ and $\beta$, XROTOR is called to design a stator: `createstatorsimplexfoil.m`.

**createstatorsimplexfoil.m**

This routine reads in the XFOIL data file created by `xfoil_data.txt`, and writes an input file for XROTOR: `xrotor_statormil.txt`. It then runs XROTOR INPU routine which will create the stator by specifying the geometry directly;
`<statorname>.prop`, which is stored in folder `/stator`. The XROTOR velocity weights for the influence of the rotor slipstream on the stator are 0.5 for axial slipstream components, and $-1.0$ for the tangential components as suggested by the program's manual.

**createsystemslipstream.m**

Rotor and stator slipstream files are read in and stitched together to create a slipstream velocity file
`system*.vput`. A figure is plotted which contains three subplots; for rotor, stator, and system the axial and tangential slipstream velocity distributions are plotted.

**loadgeneralparameters*.m**

There are four versions of this file. `loadgeneralparameters.m` contains generic input parameters for a rotor-stator system, and can be modified by the user to suit any rotor-stator combination. The three other files are pre-arranged versions of this file for the APIAN, the Fokker F50 cruise and the Fokker F50 take-off design cases. When a new stator will be designed, the user can change the stator name which will be used throughout the program,

most visibly by the `<statorname>.prop`, `<statorname>.vput`, and `<statorname>.writ` created and used by XROTOR. The other input parameters are:

- $J_{des}$: The rotor analysis advance ratio for which a stator will be designed
- $J_{lb}$: Lower bound of advance ratio range
- $J_{ub}$: Upper bound of advance ratio range
- $J_{step}$: Step size of advance ratio range
- *spacing*: Spacing between rotor and stator blade heart lines. Does not affect slipstream contraction as described elsewhere; for plotting purposes only.
- *error threshold*: Convergence limit; maximum difference between the propulsion efficiencies of two successive iterations.
- *toggle for CATIA files*: Toggle to allow the program to write out airfoil section coordinates for CATIA 3D modeling. Switching off decreases runtime.
- *statorslipscaleratioequalhub* : Ratio of rotor far wake slipstream radius over rotor tip radius.
- *statorhubscaleratio*: Ratio of stator hub radius over rotor hub radius.
- *statorhwkscaleratio*: Ratio of stator hub wake radius over rotor hub wake radius. For all practical purposes when no spinner model is applied, assume the hub wake radius equal to the hub radius.
- *statorpowerratio*: Ratio of stator power over rotor power for XROTOR analysis routine.
- *statorrpmratio*: Ratio of stator *rpm* over rotor *rpm* for XROTOR design routine.
- *statorrpmratioa*: Ratio of stator *rpm* over rotor *rpm* for XROTOR analysis routine.
- *altitude*: Altitude in [km] to set ambient conditions according to the International Standard Atmosphere model (ISA) in XROTOR.
- *xrotorform*: Toggle for XROTOR FORM menu, three options are available for calculating induced velocities and induced losses.
- *xrotorwake*: Toggle for rigid wake modeling in XROTOR.
- *convlimit*: Maximum number of iterations allowed per analysis point before moving to next analysis point. Prevents program from entering infinite loop if XROTOR does not converge.

**main.m**

This is the main program, which handles all the user input. It can analyze a rotor-stator system by using XROTOR, by reading in an existing rotor and using an existing stator or designing a new one. The first user input is the rotor name, which should correspond to a XROTOR `<rotorname>.prop` file in the `/rotor` sub-folder. The program also comes with existing rotor files of the APIAN rotor with a blade angle of 40.4° at $0.75r/R$, and two Fokker F50 Dowty-Rotol rotors, one in cruise conditions and one in take-off conditions. A second menu asks the user if an existing stator should be analyzed, if so, enter the stator name. The stator `<statorname>.prop` file should be located in the `/stator` sub-folder. If no existing stator is being used, the user can decide to let XROTOR design a stator according to the minimum induced loss principle, or use a simple BEM with a rectangular blade to design a crude stator. The third menu asks the user which file should be read in to import the ambient conditions at which the analysis should take place, and rotor-stator geometry parameters such as axial spacing and slipstream radius scaling ratios and stator design parameters. Finally, the fourth menu gives the user two options for analysis: a point analysis at a certain advance ratio $J$ or a sweep over a range of advance ratios. In the latter case, the user has to input the minimum and maximum $J$ and the step size for this range. With the input complete, a `README.txt` file is written which contains general information about the program.

The main analysis part is next. A folder to store data is created for either the point analysis or sweep analysis case: `/case.point` or `/case.sweep`. The stand-alone rotor analysis routine `rotoranalysisstandalone.m` is run to create a rotor slipstream `<rotorname>.vput` and parameter `<rotorname>.writ` files needed for the stator design routine. If a stator is to be designed, depending on the user input, either `createstator.m` is called for the MIL design routine, and `createstatorsimple.m` for the BEM design routine. With a rotor and stator present and all other operating parameters defined, the main advance ratio analysis routine is called: `advanceratioanalysis.m`. When this routine is finished, the general analysis parameters are written to a file by routine `writeparameters.m`. Finally all relevant analysis files are copied into the case folder mentioned above by routine `copyfiles.m`.

After finishing the analysis, the program displays the runtime and finishes. If the program crashes shortly after starting the analysis loop, it is almost certain that the analysis point or range of $J$ is poorly chosen and XROTOR cannot output a `*.vput` file due to convergence errors. The user is advised to first check if the input value(s) for $J$ is/are sensible, and also the rotor-to-stator power ratio, *rpm* design ratio, and *rpm* analysis ratio can be modified, as the sensitivity analysis of Chapterchap:xrotorissues mentions.

**slipstreamscaling.m**

In order to deal with a difference in rotor hub and stator hub radii, a scaling method is applied in this routine to calculate the new slipstream radius. It assumes that the cross-sectional area of the streamtube (the part seen by the rotor blades) stays constant, even when the hub radius changes. A larger hub radius will therefore 'push' the streamtube slightly outwards. See also Figure C.2.

**rotoranalysisstandalone.m**

This code outputs a text file with commands for XROTOR, `rotoranalonly.txt`, and then runs this file through XROTOR. The rotor is analyzed at the given advance ratio, as a stand-alone rotor. XROTOR creates slipstream and performance output files; `<rotorname>.vput` and `<rotorname>.writ`.

**rotoranalysis.m**

This code outputs a text file with commands for XROTOR, `rotoranal.txt`, and then runs this file through XROTOR. The rotor is analyzed at the given advance ratio, and takes into account the influence of the stator using the velocity weights of 0.5 for axial effects and 0 for tangential effects. XROTOR creates slipstream and performance output files; `<rotorname>.vput` and `<rotorname>.writ`.

**rotorvputscaling.m**

The rotor slipstream data outputted by XROTOR has to be scaled down to mimic the slipstream contraction at the stator plane. This routine takes care of that by scaling the radial stations between hub and tip.

**statoranalysis.m**

This code outputs a text file with commands for XROTOR, `statoranal.txt`, and then runs this file through XROTOR. The stator is analyzed at the given *rpm* and power, and takes into account the influence of the rotor using the velocity weights of 0.5 for axial effects and $-1.0$ for tangential effects. XROTOR creates slipstream and performance output files; `<statorname>.vput` and `<statorname>.writ`.

**statorvputscaling.m**

The stator slipstream data outputted by XROTOR has to be scaled down to mimic the slipstream contraction in the far wake. This routine takes care of that by scaling the radial stations between hub and tip.

**statorvputscalingback.m**

The stator slipstream data outputted by XROTOR has to be scaled up to mimic the slipstream expansion upstream at the rotor plane. This routine takes care of that by scaling the radial stations between hub and tip.

**systemperformancecalc.m**

One of the core files of the program, it calculates the system performance parameters from the rotor and stator `*.writ` files. Among the calculated parameters are the thrust, power, and torque values of the system, as well as their non-dimensional forms $C_T$, $C_P$, $C_Q$. The percentage increase in thrust, power, and torque of the system over the stand-alone rotor are calculated as well. The overall system efficiency is calculated and the difference with the previous iteration value is stored for it's parent file to check if the analysis for this data point has converged.

**convergenceplot.m**

A small routine which creates a plot errorcheck*.png for each data point showing the error value in system efficiency for each iteration. Generally only about 2 or 3 iterations are necessary for the error value to drop below the threshold value.

**enhance_plot.m**

An open-source function for MATLAB scripts, to enhance plots. The lines of the graph itself are made more visible by increasing the width. Axes, grids, and texts in x and y directions are given a different font and font size. The author of this thesis has added the same function for z-axes too.

**plotting.m**

The only function of this file is to create plots for all analyzed airfoil cases. It starts by reading in the rotor and stator *.prop files, in addition to the parameters passed on by its parent file. Figure 1 plots a top view of the system chords, thus with the rotor and stator properly spaced. Figure 2 plots a side view of the system, again properly spaced, showing the chord distribution. Note that the blade angles are set to 90 ° for this plot (i.e. the blades are 'flattened out' and not 'projected'). Figure 20 consists of two subplots which show respectively the side and the top view of a stator blade. Figure 21 shows the side view of a single stator blade, and Figure 22 shows the planform for the same stator blade ('flattened out'). Figure 3 plots the increase in propulsion efficiency in % versus advance ratios. Figure 4 shows the total system propulsion efficiency, rotor stand-alone propulsion efficiency, and the system $C_T$, $C_P$, and $C_Q$ distribution versus advance ratio. Note that Figure 3 shows the difference between the total system propulsion efficiency and the rotor stand-alone propulsion efficiency for the same advance ratio range as Figure 4, but then displayed in %. Figures 5, 6, and 7 show the increase of respectively system thrust, power, and torque over the stand-alone rotor versus advance ratio. Figures 8, 9, and 10 show the stator thrust, power, and torque versus advance ratio.

**plottingvput.m**

This subroutine reads in the rotor and stator slipstream files and creates two figures, one with the axial velocity distributions over the radii and one with the tangential velocity distributions.

**pointclouds.m**

A small subroutine which scales the airfoil data to the local chord size, rotates it to the local blade angle, moves it to x,z-coordinates and adds an y-coordinate column containing the local radial position. This x,y,z-coordinate point cloud is then written to an *.asc file, one each per airfoil. Such airfoil coordinate data can be used by 3D CAD software such as CATIA to generate 3D digital models of the stator for technical drawings or aerodynamic or structural analysis. This routine creates two figures, one top view and one 3D view of the stator blade.

**matlabtoxlsFINAL.m**

A small file which creates an MS Excel *.xls file to be used by CATIA. It starts by reading in the airfoil *.asc data files containing x,y,z-coordinates of a stator design. Then these

point clouds are written to file using `xlsappend.m`. The CATIA MS Excel file macro needs a specific input containing point clouds and descriptions, which is the reason to have the 3D point cloud file created in this manner. This routine can be run externally by the user, it is not run by the main program itself.

**`writeparameters.m`**
This routine writes all the used input parameters to a text file called `parameters.txt`.

**`xlsappend.m`**
This is file from The MathWorks, Inc. website [42], the developer of MATLAB. It uses the 'xlswrite' function of MATLAB to append data to existing `*.xls` files, which the original MATLAB function cannot do. This routine can be run externally by the user, it is not run by the main program itself.

**`xfoilanalysis.m`**
This subroutine runs a given airfoil through XFOIL to obtain data for XROTOR's airfoil modeling. By running XFOIL, a polar file is created for 0.5 <= $C_l$ <= 1.5 with a step size of 0.05. A linear fit to the $C_l$ versus $\alpha$ data is made to obtain the lift slope. A parabolic fit is made to the $C_d$ versus $\alpha$ curve, of which the polynomial fit parameters are needed for XROTOR's AERO menu airfoil input. Various other aerodynamic parameters needed for XROTOR's AERO menu are calculated, such as: $\alpha_0$, $C_{d,min}$, $C_l(C_{d,min})$. All these parameters are written to a data file named `xfoil_data.txt` and stored for use by other routines.

**Slipstream scaling for XROTOR**
As described in Appendix B, XROTOR can simulate the effect of an upstream rotor on a downstream rotor and vice versa, using the slipstream velocity profiles. XROTOR assumes that the rotor spacing is small enough that both rotors influence eachother. The downstream rotor sees the upstream rotor's velocity profile added to the freestream velocity profile, with appropriate weighing factors to influence to which extend the downstream rotor 'sees' the upstream slipstream. At the same time, the upstream rotor's incoming flow is also slightly altered by the downstream rotor's presence. A flow chart of how the XROTOR slipstream files are passed around by the rotor and stator analysis routines to influence eachother and to create a system slipstream can be seen in Figure C.1.

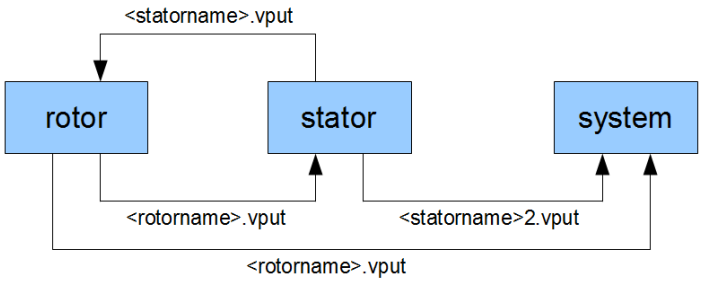


Figure C.1: Flow chart of the XOTOR `*.vput` slipstream files, as they are used within the rotor-stator analysis routine `advanceratioanalysis.m`.

The slipstream of the full system is composed of the rotor and stator slipstreams, as mentioned earlier in Section C. Figure C.2 shows in a schematic way what the streamtube scaling looks like and how the system slipstream is created from the two other slipstreams. Of particular interest is the 'jump' in rotor slipstream radius between the rotor and stator locations. Note that the hub radii are not equal for rotor and stator, a common occurence in counter-rotation propulsion systems due to aerodynamic spinner geometry. Especially when SRVs are installed as retro-fit, the hub radii are likely to be different.

Figure C.2 clearly shows how the large step in hub radius has a small but significant effect on the tip radius of the rotor slipstream. The stator therefore sees the same rotor slipstream as before the hub radius increase, but finds the slipstream velocities at different radial locations.

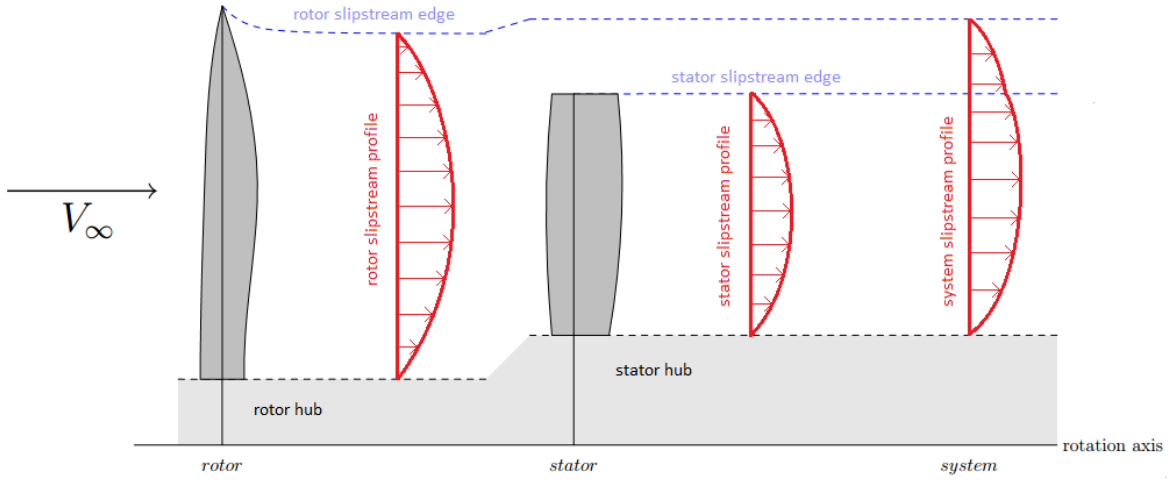


Figure C.2: Schematic view of how the rotor and stator slipstreams are joined together to form the system slipstream profile. Here only schematic axial slipstreams are shown (red), the procedure for tangential flow is similar except that the two slipstreams are then subtracted instead of added. Note how the change in hub radius 'pushes' the slipstream tube (blue) slightly outwards between rotor and stator.

The author has proposed a slipstream scaling model to allow for different hub radii. Because propellers work at subsonic speeds, mostly below $M < 0.7$, the assumption is made that the flow is incompressible (XROTOR itself uses a compressibility correction for the airfoil polars to incorporate compressibility effects). The streamtube downstream from the rotor has the shape of an extruded annulus. When it encounters an increase in hub radius, it's tip radius should increase such that the annulus cross-sectional area stays constant, as incompressible flow dictates this. Because of the constant annulus area, the axial velocities are equal too. No scaling of the slipstream velocity values is required, only the radial positions belonging to the velocity vectors need to be altered.

For now, assume that there is no slipstream contraction, as it is generally small as discussed in at the end of Section 2.1. The areas of both slipstream cross-sections or disks, Figure C.3, can be found using the following equations:

$$A_{rotordisk} = \pi \left( {r_{tip,rotor}}^2 - {r_{hub,rotor}}^2 \right)$$
$$A_{statordisk} = \pi \left( {r_{tip,stator}}^2 - {r_{hub,stator}}^2 \right) \tag{C.1}$$

An imcompressible fluid with the assumption of equal mass flow makes that both cross-sectional areas should be equal:

$$A_{rotordisk} = A_{statordisk} \tag{C.2}$$

With the stator hub radius known, the new stator tip radius (without slipstream contraction) becomes:

$$r_{tip,stator} = \sqrt{\frac{A_{statordisk}}{\pi} + {r_{hub,stator}}^2} \tag{C.3}$$

Any slipstream contraction is generally small. The value of 95% of the radius found in the low speed APIAN data (Section 4.3) is drawn as a red dashed circle in Figure C.3; $statorslipscaleratio = 0.95$ here. Cropping of the stator is defined as the percentage or ratio of this new slipstream radius, and is shown as a green dashed circle in the same figure, with an example cropping ratio of 0.9.

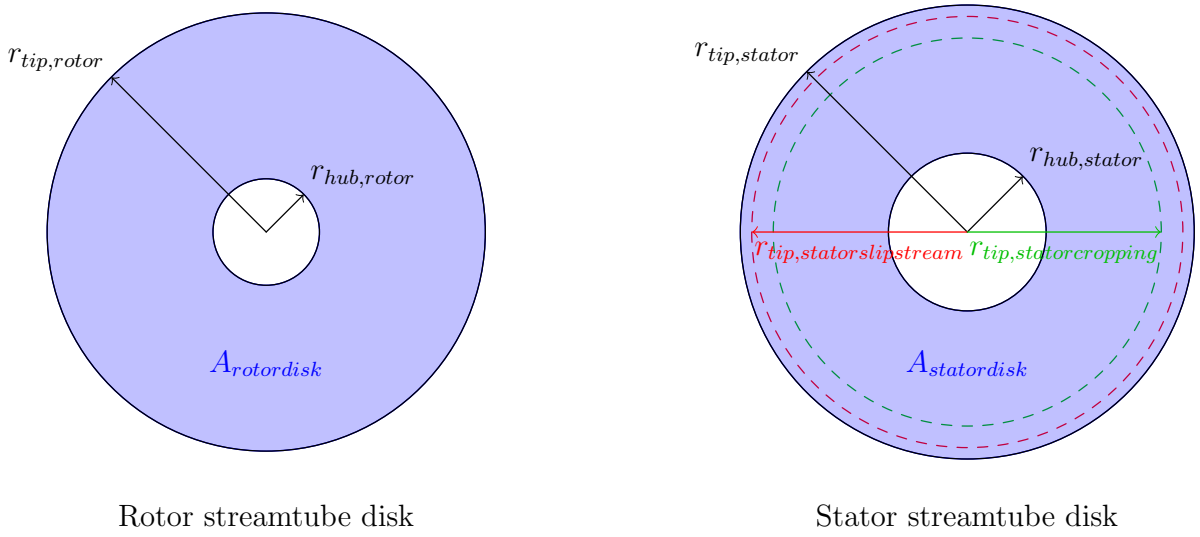


Figure C.3: Geometry of cross-section of streamtube at the rotor and stator disks. Both blue areas have the same size. The stator disk includes dashed circles indicating the slipstream contraction (red) and stator tip radius cropping (green).

With $r_{tip,stator}$ and $r_{hub,stator}$ now known, the scaling procedure for the radial location of the slipstream velocity vectors is explained. First a scaling ratio is defined, which relates the stator blade length to the rotor blade length:

$$statorscalingratio = \frac{statorsclipscaleratio * r_{tip,rotor} - r_{hub,stator}}{r_{tip,rotor} - r_{hub,rotor}} \tag{C.4}$$

A temporary radius is defined for each rotor radius, based on the above scaling ratio. It scales a rotor radius such that is has the correct relative radial distance from other radii, but absolute radial position of the scaled radius is not correct yet.

$$newradius = r_{rotor} * statorscalingratio \tag{C.5}$$

The next equation shifts the new radius to its proper radial location as rotor slipstream radius.

$$r_{rotor,slipstream} = newradius - statorscalingratio * r_{hub,rotor} + r_{hub,stator} \tag{C.6}$$

The files which scale the stator slipstream for the rotor slipstream use a rather similar but reverse procedure. The file which scales the stator slipstream before it is used to create the system slipstream uses the above procedure too.

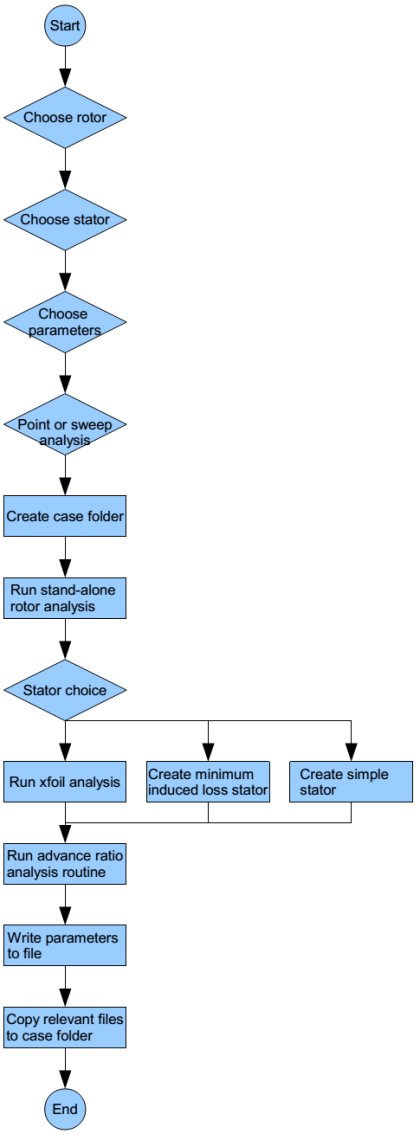


Figure C.4: Flow chart of routine `main.m`.

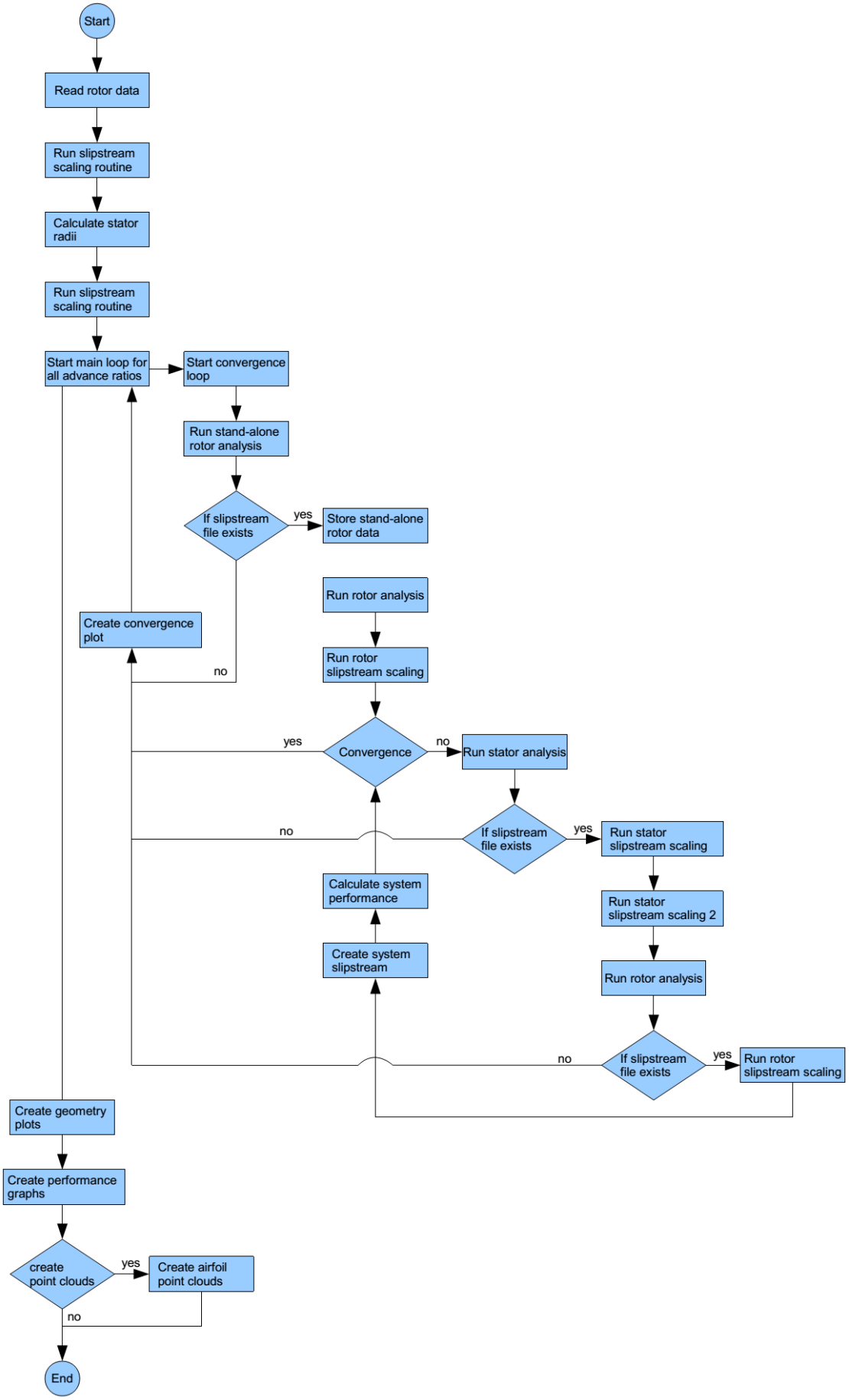


Figure C.5: Flow chart routine `advanceratioanalysis.m`.

# D

# APPENDIX D - ROUTINES LIFTING LINE PROGRAM

A short description is given for each routine of the lifting line method, in alphabetical order. Flowcharts of the full routine and the lifting line subroutine are presented.

`mainliftline.m`

The main file first asks the user for a wing design and ambient conditions. See the left part of Figure D.1. The user can choose from a F50 wing modeled after Veldhuis [34] in either cruise or take-off conditions, or choose to input an arbitrary unswept wing with 2 trapezoidal panels per half span at arbitrary conditions. Next the user is asked to input rotor or system slipstream parameters such as radius and distance between the wing centerline and slipstream centerline. Again the user can also opt to use an existing F50 rotor in cruise or take-off conditions. The third and last input from the user is the number of lifting line nodes. This number must not be too small to miss out on proper slipstream modeling, $N > 50$ is a good advice, and already $N = 200$ gives good results without too much runtime. The number of nodes must be even, otherwise one node will be placed at the centerline of the wing which causes this particular way of modeling the wing to crash. The chord distribution, angle of attack distribution, and zero-lift angle of attack distribution over all nodes are found and various other wing and slipstream related parameters are calculated.

With the input complete, the main loop over the three cases is called. The first case is the wing with installed rotor slipstreams, as this will be the reference case from which the other two cases will be judged. Case two is the wing with installed rotor-stator system slipstreams. Case 3, just for comparison, is the uninstalled clean wing. To be able to assess the efficiency increase or decrease the lift should be equal in all cases. Since the slipstream presence or absence changes the circulation distribution over the wing, an iterative procedure is incorporated in cases 2 and 3 to change the overall angle of attack (e.g. changing the pitch angle of the full wing) until the current lift over the previous case lift ratio is within a certain error threshold. For each case, all relevant parameters such as $C_L$, $C_{D0}$, $C_{Di}$, $C_D$, $L/D_{wing}$, roll moment $M$, total lift $L$, and number of iterations are calculated and stored, as well as the spanwise distributions of $\alpha_i$ and $\Gamma$, and the $\Delta\alpha$ due to the equal lift constraint.

Output of the code consists of on-screen output of all relevant parameters mentioned above, in a table-like output such that the differences between the cases can easily be compared. This output is also written to a `*.txt` file. Two subroutines create plots, one creates a number of 2D plots of various spanwise distributions, the other creates six 3D plots of the wing with for each case the $C_l$ and $\Gamma$ distribution (not to scale, for illustrative purposes only). The installed cases also show the slipstream streamtubes over the wing.

**`prandtlwing*.m`**
This file asks the user to input the flow conditions such as $V$, $\rho$, and $\mu$. It then asks the user to input all required wing geometry and airfoil names. Preset versions of this file exist for the Fokker F50 cruise and take-off case.

**`prandtlrotor*.m`**
This file asks the user to input rotor parameters such as the slipstream name, spanwise distance of the rotation axis, and if the rotor rotates 'inboard up' or 'inboard down'. Preset versions of this file exist for the Fokker F50 cruise and take-off case.

**`llcase#.m`**
This file is nearly the same for each of the three cases. A generic flow chart of a case is shown in the right part of Figure D.1. The routine immediately enters an iteration loop to have equal lift compared to the previous case. Case 1 obviously only has one iteration since there is no previous lift value to compare with. Next, the rotor or system slipstream *.vput file is read in. A polynomial of order 5 is used to create a good polynomial fit to the tangential and axial slipstream velocity distributions. If there is no slipstream present whatsoever, as in case of the clean wing, these values are set to 0.

The code will now calculate for each node the local axial ($V_x$) and vertical ($V_z$) velocity components. Since the slipstream centerline is assumed to be in the same plane as the lifting line, the slipstream tangential velocities therefore directly translate into vertical velocity components on the lifting line. These are read from the polynomial created earlier. Outside the slipstream tubes, $V_z = 0$, and $V_x = V_\infty$. The local total velocity and the increase of local $\alpha$ due to slipstream effects are calculated. The angle of attack distribution is thus altered where needed.

Lifting line core calculations are made next, as presented in the book by Anderson [32], or see Chapter 5.2 for an explanation of the lifting line core method with slipstream effects. After setting up the matrices and solving the system, the wing performance parameters $C_L$, $C_{D0}$, $C_{Di}$, $C_D$, $L/D_{wing}$, roll moment $M$, total lift $L$, the spanwise distributions of $\alpha_i$ and $\Gamma$, and the $\Delta\alpha$ are calculated. regarding the aircraft control system, the roll moment introduced by the stators should be added up to the wing roll moment for that case. Since this analysis is concerned with the aerodynamic effects, only the roll moment due to the slipstream is calculated.

**`writewingparameters.m`**
This routine outputs the data as seen on the screen to a `*.txt` file.

`liftlineplots3.m`

All five 2D graphs are made by this routine. One graph is a top view of the wing, the other four show respectively the spanwise distributions of various angles, $C_l$, nondimensional $\Gamma$, and a side view of the wing airfoils.

`enhance_plot.m`

An open-source function for MATLAB scripts, to enhance plots. The lines of the graph itself are made more visible by increasing the width. Axes, grids, and texts in x and y directions are given a different font and font size. The author of this thesis has added the same function for z-axes too.

`wing3dplot.m`

The six 3D views of the wing with either a $C_l$ or $\Gamma$ distribution are made by this routine. Plotting can take quite some time.

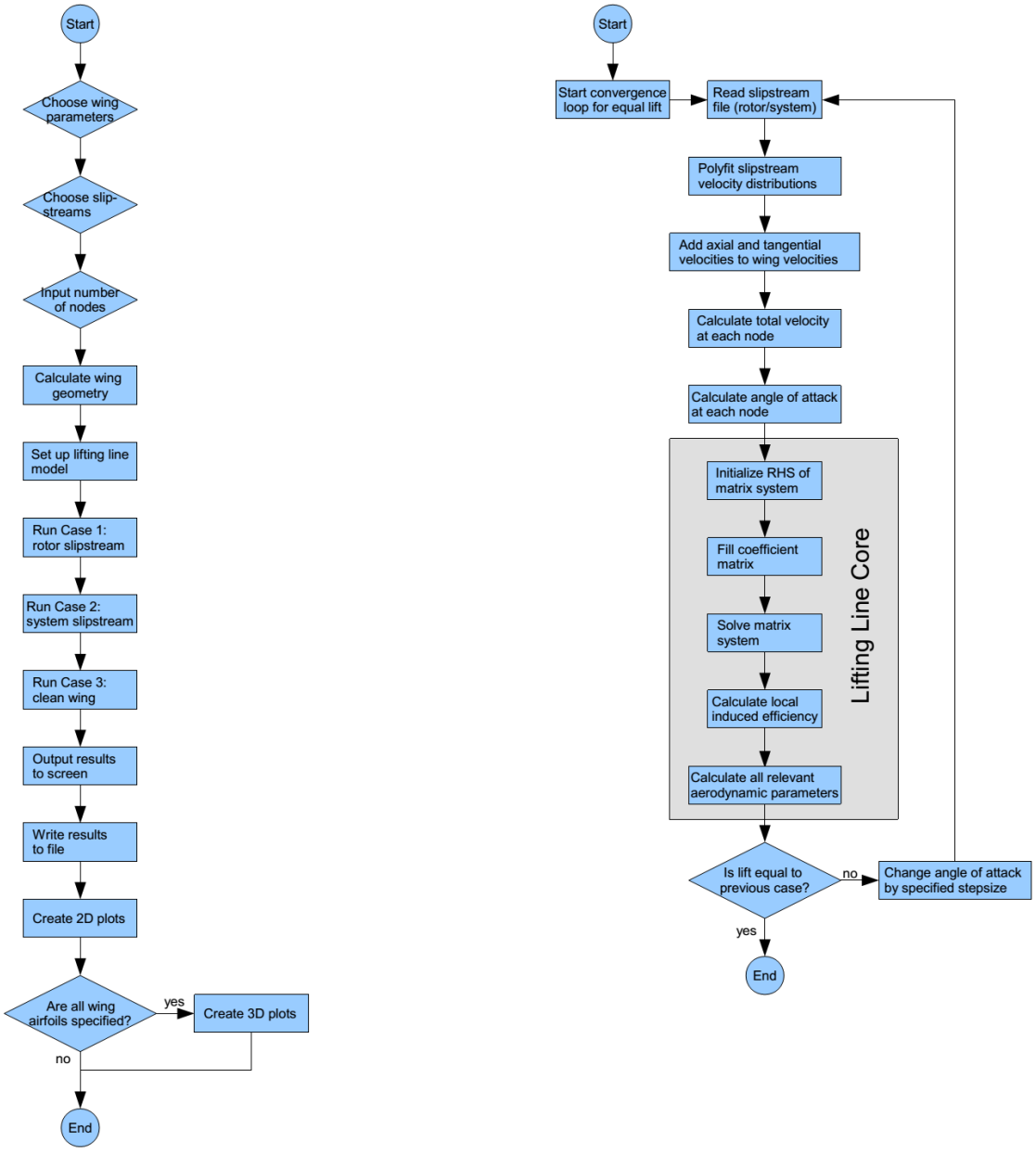


Figure D.1: Flow charts of the main file (left) and a generic case file (right) of the lifting line with slipstream interaction code.

# E

# APPENDIX E - CODE: ROTOR-STATOR PERFORMANCE ANALYSIS

Computer codes belonging to the rotor stator performance analysis program can be found on the accompanying CD-ROM. Code listings are not shown to preserve paper.

# F

# APPENDIX F - CODE: LIFTING LINE METHOD WITH SLIPSTREAM INTERACTION

Computer codes belonging to the lift line method with rotor-stator slipstream interaction can be found on the accompanying CD-ROM. Code listings are not shown to preserve paper.